

Politecnico di Torino

Master's Degree in Aerospace Engineering



Master's Thesis

Satellite Formation Flying Initial Configuration Maintenance Using Impulsive Maneuvers

Academic tutors

Prof. Giorgio GUGLIERI

Prof. Franco BERNELLI ZAZZERA

Company tutor

Ph.D. Reza R. KARIMI

Candidate

Edoardo BRUNO

Academic Year 2019/2020

*“A mamma, papà e Sofia,
la formazione più forte della mia vita”*

Edoardo

Abstract

On-orbit Servicing missions are increasingly gaining interest among the aerospace community driven by a growing commercial space sector that has developed a market for servicing Earth-orbiting satellites. Such missions may require a formation of satellites to maintain a precise shape with mission-appropriate tolerances, depending on the tasks to carry out. Indeed, over the past two decades, space agencies have questioned the need to use single platforms with a high level of complexity, which is not always associated with a high degree of reliability, a key driver in any space mission. Several studies have shown that spacecraft formations can perform tasks previously accomplished with single space platforms, often large and complex, but employing smaller satellites and therefore significantly lower costs. Spacecraft formation flying consequently represents an emerging technology with high potential for future commercial and scientific space missions. The purpose of this work is the analysis of a formation of satellites (deputies) in different configuration, orbiting around a main spacecraft (chief). The formation is deployed in a Low Earth Orbit (LEO) and also in some asteroid low orbits. In order to perform some scientific or commercial tasks, the formation is required to maintain its original shape as unaltered as possible. It is therefore necessary to apply maneuvers for each deputy individually to counteract the natural dynamics of the spacecraft. In this regard, an algorithm has been developed to determine the best set of initial conditions, able to guarantee the lowest amount of deconfiguration. Orbital perturbations such as J_2 and atmospheric drag were also taken into account to perform more accurate simulations. In the last part of the work, an analysis was conducted in order to observe the effects of variation in altitude or formation size. This thesis work is the result of an internship conducted in collaboration with NASA's Jet Propulsion Laboratory.

Acknowledgements

Before presenting this dissertation, I would like to dedicate a few lines to all those who have contributed to the realization of this work and to my human and professional growth during these years of university. Looking back in the past, Politecnico di Torino allowed me to live five intense but also inspiring years. My experiences with the Alta Scuola Politecnica and the period spent in Toulouse, France, were stimulating challenges that introduced me to people from whom I learned a lot in view of the future.

First and foremost, I feel compelled to thank my tutor, Ph.D. Reza Karimi, for his support and willingness throughout these months. His encouragement has been truly invaluable to me. Without him this work probably could not have even started. Unfortunately the health crisis we had to face didn't allow me to live this experience as I would have liked. Writing a thesis while working completely remotely is not an easy task, but despite this we managed to build a not only professional but also human relationship. I am extremely grateful to him for this.

I am proud to have worked with such a prestigious institution as NASA's Jet Propulsion Laboratory, albeit in a very particular time and manner. I would like to express my gratitude to Ph.D. Jon Sims, who had faith in my abilities by giving me this unique opportunity.

I would like to thank my academic advisors, Professor Guglieri and Professor Bernelli Zazzera, for their helpfulness and promptness in responding to my every request, which is truly an uncommon quality. Even though I did not collaborate directly with them, they were always willing to give me the right advice in every phase of the realization of this thesis.

Special thanks go to my family, to whom this thesis is dedicated. A few lines will never be enough to express my eternal gratitude to them. Without them I would not be the person I am. Thank you for all the sacrifices made in these years, thank you for having always supported my life choices. I would like this achievement of mine to be a reward for them as well.

Finally, I think it's only fair to express a thought towards all of my friends with whom I have shared part of this journey, both inside and outside of the university. To mention them all would be impossible, but those who read this will know that they are involved. An ancient African proverb says "*If you want to go fast, go alone. If you want to go far, go together*". I prefer to go far. Thank you for being by my side.

Edoardo

Table of Contents

List of Figures	XI
List of Tables	XIII
Acronyms	XV
List of Symbols	XVII
1 Introduction	1
1.1 A brief history of orbital dynamics	1
1.2 The concept of spacecraft formation flying	5
1.3 Coordination approaches	8
1.3.1 Orbit Tracking	8
1.3.2 Leader/Follower (Chief/Deputy)	8
1.3.3 Virtual Structure	9
1.3.4 Swarming	9
1.4 Formation flying missions	10
1.5 Scope of this work and thesis outline	15
2 Theoretical Background	17
2.1 Coordinate systems	18
2.1.1 ECI reference frame	18
2.1.2 Euler-Hill Frame	19
2.1.3 Polar Frame	20
2.1.4 Transformation between ECI and Hill-frame	21
2.2 The Keplerian two-body problem	23

2.3	Spacecraft relative dynamics	26
2.4	Linearization of relative motion equations	29
2.5	The energy matching condition	32
2.6	Case study description	34
3	Formation Simulations	39
3.1	Unperturbed case	39
3.2	Independent motion	43
3.3	Clohessy-Wiltshire linearization	46
3.4	Perturbed case	50
3.5	Formation control	55
3.5.1	The objective function	56
3.5.2	Triangular formation	58
3.5.3	Tetrahedral formation	60
4	Sensitivity Analysis	63
4.1	Change in the formation size	63
4.2	Effects of formation's altitude	65
4.3	Application on Vesta	67
5	Conclusions	71
A	Complementaries on Keplerian problem and relative motion	75
A.1	Change of coordinates from \mathcal{I} to \mathcal{R}	75
A.2	Conservation of energy	75
A.3	Spacecraft relative motion	76
B	Matlab scripts	79
	Bibliography	107

List of Figures

1.1	Aristarchus of Samos.	3
1.2	Rendering of the GRACE mission.	12
1.3	Illustration of the four MMS spacecraft in orbit in Earth's magnetic field.	14
2.1	ECI Reference Frame.	19
2.2	Local-Vertical, Local-Horizontal rotating coordinate system.	20
2.3	Polar coordinate system centered at the primary.	21
2.4	\mathcal{I} -frame and \mathcal{L} -frame. ECI is depicted in green, LVLH in blue.	27
2.5	Rendering of a potential 3U-Cubesat employed in the formation.	35
3.1	Initial positions of the deputies around the chief, forming the ideal tetrahedron.	40
3.2	Relative orbits for the unperturbed case. The chief is located at the origin of the axes (LVLH-frame).	41
3.3	Distance between deputies and chief (unperturbed case).	42
3.4	Distance between deputies (unperturbed case).	42
3.5	Absolute orbits of chief and deputies in ECI frame.	44
3.6	Distance between deputies and chief (independent trajectories).	45
3.7	Distance between deputies (independent trajectories).	45
3.8	Distance between deputies and chief using HCW equations.	48
3.9	Distance between deputies and chief using HCW equations, with the no-drift condition.	48
3.10	Distance between deputies using HCW equations.	49

3.11	Distance between deputies using HCW equations, with the no-drift condition.	49
3.12	Earth geoid.	51
3.13	Relative orbits for the perturbed scenario.	53
3.14	Distance between deputies and chief for the perturbed scenario.	54
3.15	Distance between deputies for the perturbed scenario.	54
3.16	Triangular formation maintenance - Deputy-Chief distance.	59
3.17	Triangular formation maintenance - Distance between deputies.	59
3.18	Secular motion of the triangular formation. One burn per orbit is applied.	60
3.19	Tetrahedral formation maintenance - Deputy-Chief distance.	61
3.20	Tetrahedral formation maintenance - Distance between deputies.	62
3.21	Effect of the adjustment of the cost function. Deputy-Chief distance has been given a 10-times more importance than the inter-deputy distance.	62
4.1	Representation of asteroid Vesta.	68

List of Tables

2.1	Chief's orbit parameters (baseline scenario)	36
2.2	Chief's orbit hybrid parameters (baseline scenario)	38
4.1	Sensitivity analysis for formation size at the same altitude (350 km) (with atmospheric drag) - ΔV for 100 orbits	65
4.2	Sensitivity analysis for formation altitude with the same size (100 m) (without atmospheric drag) - ΔV for 100 orbits	66
4.3	Sensitivity analysis for formation altitude with the same size (100 m) (with atmospheric drag) - ΔV for 100 orbits	66
4.4	Asteroid Vesta's main characteristics. Source: [21].	67
4.5	Asteroid Vesta's orbital characteristics. Source: [22].	68
4.6	Sensitivity analysis for Vesta (effect of J_2 parameter) - ΔV for 100 orbits	70

Acronyms

ARE Algebraic Riccati Equation

AU Astronomic Unit

CLF Control Lyapunov Function

CM Center of Mass

CW Clohessy-Wiltshire

DLQR Discrete-Time Linear Quadratic Regulator

DOF Degrees of Freedom

ECI Earth-Centred Inertial coordinate system

EOM Equations Of Motion

FF Formation Flying

FFC Formation Flying Control

HCW Hill-Clohessy-Wiltshire

IC Initial Condition

JPL Jet Propulsion Laboratory

KF Kalman Filter

LEO Low Earth Orbit

LQR Linear Quadratic Regulator

LVLH Local-Vertical Local-Horizontal coordinate system

NASA National Aeronautics and Space Administration

ODE Ordinary Differential Equation

OOS On-Orbit Servicing

PCO Projected Circular Orbit

RAAN Right Ascension of the Ascending Node

STM State-Transition Matrix

UTC Universal Time Coordinated

List of Symbols

$(\cdot)_0$ Subscript for chief satellite's coordinates

$(\cdot)_1$ Subscript for deputy satellite's coordinates

A Spacecraft sectional area

a Semi-major axis

\mathbf{a} Acceleration vector

\mathcal{E} Total energy per unit mass

e Eccentricity

f True Anomaly

\mathbf{h} Angular momentum vector

\mathcal{H} Hill reference frame (same as \mathcal{L})

i Inclination

\mathcal{I} ECI reference frame

J_2 Earth oblateness factor ($1.08262668355315 \times 10^{-3}$)

\mathcal{L} LVLH reference frame

M Mean anomaly

R_E Earth equatorial radius (6378.1363 km)

\mathcal{R} Polar rotating reference frame

p Semilatus rectum

ρ Atmospheric density

\mathbf{r} Position vector

t Time

\mathbf{v} Velocity vector

\mathbf{x} State vector $[x \ y \ z \ v_x \ v_y \ v_z]$

θ Argument of latitude ($\theta = \omega + f$)

Ω Right Ascension of the Ascending Node (RAAN)

ω Argument of periapsis

ω_Z Mean angular rate

Chapter 1

Introduction

The objective of this chapter is to provide the reader with a general overview of spacecraft formation flying and its growing importance in the scientific and technical domain. The purposes of this research work are also presented.

1.1 A brief history of orbital dynamics

In *War and Peace* (1869) Lev Tolstoy (1828-1910) does not limit himself to narrating the exploits of the French Emperor Bonaparte and the Russian Tsar Alexander, because he believes that focusing on the great characters is a good way to make mistakes about history. This is the task of historians, but in doing so they make, as Tolstoy himself says, the mistake of "recognizing expressed in the activity of a single historical figure the will of every man". The truth is that History, even that of orbital dynamics, is the product of a great collective action, in which each actor provides his small contribution. And Tolstoy offers an interesting mathematical metaphor in this regard: according to him, this is exactly what happens in the infinitesimal calculus, in which the individual contribution of infinitesimal quantities, called differentials, is added by calculating an infinite sum, called integral. To the educated reader who is about to read this work, the operation will sound familiar. In mathematical terms, then, history would be the integral of the infinitesimal behaviors of individuals. Unfortunately, as Tolstoy himself

admits, it is not possible to tell the story of all the individual contributors. Similarly, orbital mechanics, or celestial mechanics, is a discipline that has seen, and still sees, the contribution of many astronomers, scientists, men, whose names are often and will remain unknown. The reader will forgive me if here we will report only some of the great names of the *science of stars*, without which even I could not have been able to treat this subject.

The appeal of space is one of the attributes that has accompanied humankind since the earliest times. Everything that goes beyond the boundaries, beyond imagination, has interested and fascinated all civilizations for its mysteries and its apparent unexplorability since the ancient Greeks. At that time, the main object of study was the motion of celestial bodies, which were seen as gods, able to influence the events of man on Earth. However, if we leave out the aspect purely related to religion, it is to them that we must give credit for having examined with scientific rigor the dynamics of celestial bodies easily observable. The mechanics of celestial bodies is in fact a discipline that has its origins in ancient Greece and, not surprisingly, intertwines its roots with those of mathematics. It is in fact undeniable that the greatest contribution to mathematics comes from this civilization.

The way to deal with the astronomical problem that characterized for many centuries the Greeks and those who were inspired by their ideas, is indicated in a statement of **Plato** (428-347 B.C.), dating from the fourth century B.C. He posed the astronomical problem to his students in these terms: "*The stars, representing eternal, divine and immutable objects, move with uniform speed around the earth, as we can see, and describe the most regular and perfect of all trajectories, that of the endless circumference. But some celestial objects, that is the Sun, the Moon, the planets, wander through the sky and follow complex paths, including retrograde motions. However, being celestial bodies, they too must move in a manner consistent with their high rank: their motions must therefore derive from some combination of perfect circles, since they do not exactly describe perfect circles. What are the combinations of circular motions with uniform velocity that can explain such peculiar variations in a coherent set of regular motions in the sky?*" [1].

It emerges from this writing the importance of a question that assumes

a double meaning, that is philosophical but also mathematical. We will have to wait until **Euclid** (330-370 B.C.) to have the first evidence of the mathematical formulation of the conics, although it was **Apollonius** (262-190 B.C.) to have treated in a complete way the subject and consequently to have coined the terms parabola, ellipse and hyperbola. Astronomer and physicist, **Aristarchus** (310-230 B.C.) is known to be the one who first introduced an astronomical theory in which the Sun and the fixed stars are immobile while the Earth rotates around the Sun covering a circumference (Fig. 1.1). The heliocentric theory had been forcefully rejected a century earlier by Plato and his student Aristotle (384-322 B.C.), and was rejected four centuries after Aristarchus, even by Claudius Ptolemy, whose conceptions dominated unchallenged late antiquity and the Middle Ages. It is reasonable to assume, however, that the theory of Aristarchus was accepted for the first centuries, since Pliny the Elder and Seneca refer to the retrograde motion of the planets as an optical phenomenon and not real, a conception more in line with heliocentrism than geocentrism.



Figure 1.1: Aristarchus of Samos, the first to introduce an heliocentric theory.

The theories of Aristarchus were unfortunately not taken up by **Hipparchus** (310-230 B.C.), who succeeded however in developing accurate models to explain the motion of the Sun and the Moon, using the observations and the knowledge accumulated over the centuries by the Babylonian Chaldeans, and estimated with precision the distance between the Earth and the Moon. Thanks to his theories on the motions of the Sun and Moon and his knowledge of trigonometry, of which he is considered the founder, he was probably the first to develop a reliable method for the prediction of solar and lunar eclipses. He was also the first to catalog a thousand stars based on their brightness.

Finally, we must consider the contribution of **Claudius Ptolemy** (100-175 B.C.), author of numerous works of astronomical nature, of which the most important was *Almagest*. The original Greek title of this work was *Μαθηματικὴ σύνταξις* (Mathematikè sýntaxis, “Mathematical Collection”). The name *Almagest* (“The Greatest”) is the Arabic version of the Greek name by which the work was known and is due to the fact that, as with much of classical Greek science and philosophy, its initial diffusion in Europe was mainly through Arabic manuscripts, which were translated into Latin in the twelfth century. He took up some of the results obtained by Hipparchus but was not aware of the works of earlier astronomers, who had already predicted the spherical geometry of the Earth and placed it in rotation around the Sun. This model of the solar system, that from him will take the name of *Ptolemaic System*, remained as reference for all the western world (but also Arabic) until it was replaced in modern times by the heliocentric solar system model of the Polish astronomer **Nicolaus Copernicus** (1473-1543). Copernicus is universally recognized as the first to formulate the heliocentric model of the solar system in modern times. Although he was not the first to formulate this theory, he was the scientist who most rigorously demonstrated it using mathematical procedures. His theories were the foundation of the work developed a few years later by **Galileo Galilei** (1564-1642), the pillar of modern physics. Galileo’s name is mainly associated with that of the scientific revolution and the introduction of the scientific method, elements in open opposition to the religious doctrine imposed by the Church, which

formally cancelled in 1992 all the accusations made against him. For his work of astronomical nature, Galileo made use of the telescope, but he was not the inventor of it. He perfected a monocular developed by a Dutch optician and was the first to use the instrument to observe the sky [2].

The history of celestial mechanics continues with **Johannes Kepler** (1571-1630), a contemporary of Galilei. Professor of science at several universities in Germany and Austria and protégé of Emperor Rudolf II, he was charged with compiling the annual almanacs for the emperor. Although this task was not his greatest aspiration, it still represented a source of income and allowed him to follow his scientific interests. Kepler exploited the data of the Danish astronomer **Tycho Brahe** (1546-1601) and thanks to these he was the first astronomer who demonstrated the validity of the Copernican system based on physical causes and not on geometric models. After years of intense work, in fact, Kepler came to the famous three laws that bring his name. The first two were published for the first time in 1609 his treatise *Astronomia Nova* ("New Astronomy"), the third appears in *Harmonices mundi libri quinque* ("Harmony of the World, Fifth Book") of 1619. The importance of Kepler's laws lies in the accurate description of the kinematics of the planets, however it does not completely solve the planetary motion, because it does not involve the knowledge of the orbital dynamics. This lack will be filled by one of the greatest scientists of all time, **Isaac Newton** (1642-1727). Fascinated by Kepler's laws, Newton wondered what mysterious force forced such large bodies to be bound together. In 1687, in *Philosophiae Naturalis Principia Mathematica* ("Mathematical Principles of Natural Philosophy"), his famous three laws, foundation of classical mechanics, were published, together with the law of universal gravitation. This result enabled to achieve the analytical solution of Kepler's laws and represents the fundamental equation that governs the orbital mechanics.

1.2 The concept of spacecraft formation flying

Since the time when Newton came to the analytical treatment of the law of universal gravitation, spaceflight mechanics has reached many milestones.

The milestones of the Space Race undertaken simultaneously by the Soviets and the Americans since the 1950s are now well known. The first artificial satellite launched into space was *Sputnik 1* ("Fellow traveler"), sent into orbit by the Soviet Union on October 4, 1957. Soviet cosmonaut Yuri Gagarin (1934-1968) became the first human being to reach space when he entered Earth orbit on the Vostok 1 spacecraft on April 12, 1961, a day still considered a holiday in Russia. On the next U.S. mission *Freedom 7*, Alan Shepard (1923-1998) entered sub-orbital space on May 5, 1961, and John Glenn (1921-2016) with the *Friendship 7* mission later became the first American to successfully orbit the Earth, completing three orbits on February 20, 1962. However, these were pioneers in the Space Race, which was based on the political and economic competition of the major international powers at that time. For a long time, in fact, space has been a goal, or perhaps a starting point depending on the perspective, reachable only by nations able to have a large amount of resources, mainly economic and technical-scientific. Today the number of countries able to access the Earth orbit with an artificial satellite has drastically increased, but at the same time the technological level of space missions and objectives has definitely increased. This is the reason why it is unreasonable to think that, except for rare cases, a single state can employ enough resources to reach a milestone in the space race. All major projects (e.g. International Space Station) now involve collaboration between multiple national governments and their space agencies, so that each state can make its own contribution and subsequently benefit from the advantages generated by this investment.

From a technical point of view, since the early days of the Space Race many of the achievements made in the aerospace field have been based on single space platform designs, most of them large and complex. This approach has involved both unmanned missions and manned missions, which are notoriously more complex and expensive. In the last two decades approximately, however, space agencies have questioned the necessity of using platforms with this high level of complexity, which does not always go in parallel with a high degree of reliability, a fundamental driver of space missions. As a result, several analyses have been conducted to verify the validity of this

approach. What has been realized is that many of the goals set in the past could be achieved by exploiting a network of smaller satellites, able to work together as a whole. Hence, using a terminology typically more related to aeronautics, the concept of spacecraft formation flying was born. But what exactly is formation spaceflight? Its definition is not very precise or universally recognized. Most of the space community, however, would agree with the definition proposed by NASA's Goddard Space Flight Center (GSFC): "*The tracking or maintenance of a desired relative separation, orientation or position between or among spacecraft*" [3]. Spacecraft in formation can then be considered as belonging to a broader category called distributed space systems, defined by the GSFC as follows: "*An end-to-end system including two or more space vehicles and a cooperative infrastructure for science measurement, data acquisition, processing, analysis and distribution.*" According to the GSFC, there are, however, some distinctions between the various concepts of space flight in formation. A constellation is a set of spacecraft that constitutes the spatial element of a distributed space system; virtual aperture is the actual aperture generated by physically independent spacecraft; virtual platform is a spatially distributed network of individual vehicles that collaborate as a single functional unit and exhibit a common system-wide capability to achieve a shared goal [3].

Thus, the prospects offered by formation-based spaceflight piqued the interest of the space community, which began to conduct more specific analyses at the turn of the 1970s and 1980s. In fact, in 1977, Sholomitsky, Prilutsky and Rodin conceptually studied a proposed multiple spacecraft interferometer for infrared synthetic aperture imaging [4]. Today, formation flying is a critical technology for planned and future missions of NASA, the Department of Defense, ESA, and other national space agencies. In the late 1980s and early 1990s, research focused on developing aerodynamic drag compensation strategies, and fuel-efficient relative trajectories for Earth orbiting formations. These fuel-efficient trajectories are referred to as passive relative orbits. Significant interest in formation flying started to develop in the late 1990s. The first formal study of spacecraft Formation Flying Control (FFC) was by Wang and Hadeeth in 1996, who analyzed the Leader/Follower

(Chief/Deputy) architecture [5]. However, the mission architecture analyzed by Wang and Hadeeth is not the only one that can be considered. In fact, there are several approaches to considering a satellite formation, which will be briefly described in the next section.

1.3 Coordination approaches

As mentioned in the previous paragraph, spacecraft formation flying can be conceived following different approaches, each of which interprets in its own way the relationship between the various satellites that constitute the formation. It is evident that the physics of the problem remains the same in each case, but this may influence elements such as the mission architecture or the spacecraft control. The main methods for coordination reported in the literature are briefly described in the following paragraphs.

1.3.1 Orbit Tracking

The design of single-satellite space missions typically involves a platform occupying a precise orbit, or a specific position within an orbit. Due to the ever-present orbital perturbations, however, station-keeping maneuvers are regularly performed. It is therefore possible to extend the same approach to a formation of satellites, where each is controlled by reference to its specific orbit. This is a primitive conception, since each satellite is fundamentally treated individually and there is no real coordination between satellites.

1.3.2 Leader/Follower (Chief/Deputy)

The approach followed here features a leader satellite positioned on a reference orbit and another follower satellite whose position is determined relatively to the leader. In this design, the leader satellite travels the designated orbit around the primary body, possibly subject to perturbations, and correction maneuvers are applied to it. Physics dictates that the follower satellite also travels its orbit around the primary body, but its position

and velocity are always seen in reference to the leader satellite, which is by definition in its correct state. The advantage of leader following is that group behavior is directed by specifying the behavior of a single quantity: the leader. The disadvantage is that there is no explicit feedback to the formation. Another disadvantage is that the leader is a single point of failure for the formation [6]. The Chief/Deputy definition is similar to the one described, with the difference that typically the former is used in case of a single follower, while the latter is more appropriate when the number of deputies is greater than one. It is interesting to note that this approach is typically used for classical orbital rendezvous between artificial satellites, where generally the leading satellite maintains its orbit, while the follower corrects its relative orbit in order to engage it.

1.3.3 Virtual Structure

In the virtual structure approach the entire formation is treated as a single structure [6]. Virtual structure and virtual center approaches fit a set of desired states to a formation in a way that minimizes the overall state error of the formation [3]. The virtual structure can evolve as a rigid body in a given direction with some given orientation and maintain a rigid geometric relationship among multiple vehicles. The advantage of the virtual structure approach is that it is fairly easy to prescribe a coordinated behavior of the group. Furthermore, compared to the leader/follower approach, the state error will pertain to all the spacecraft in the formation. The disadvantage of this approach is that requiring the formation to act as a virtual structure limits the class of potential applications of this approach. Lastly, the implementation of a virtual structure approach requires of course coordinated inter-spacecraft communication.

1.3.4 Swarming

In a swarm, the number of satellites is not defined a priori but typically we refer to a formation with a large number of spacecraft, with none of them playing a leading role. Over the years, several researchers have proposed

control laws to handle an arbitrarily large number of vehicles in a formation. These methods have the advantage of easily scaling to a large number of vehicles without incurring large communication or computational burdens. It is no coincidence that space formations with a decidedly large amount of satellites are now a reality (e.g. Space X's *Starlink* constellation). However, these approaches are typically not optimized for fuel consumption and rarely include specific systems to ensure collision avoidance.

1.4 Formation flying missions

During the last two decades or so, the prospects offered by formation spaceflight have aroused the interest of several space agencies, which have begun to evaluate the possibility of missions related to the subject. Several missions have been planned, some of which have remained in the concept or study phase, while others have reached the development or operational phase. The main objectives of these missions are scientific or programmatic, ranging from the acquisition of images with sparse aperture telescopes for the observation of extra-solar planets, to the analysis of gravimetry in lunar orbit. However, it must be recognized that today we cannot exclude the commercial component related to these services, thanks to the affirmation of tested technologies and the general lowering of costs.

One of the first missions of a certain relevance conceived was *TechSat-21* (Technology Satellite of the 21st Century), developed by the U.S. Air Force Research Laboratory's Space Vehicles Directorate to test the formation flying technology, exploiting small similar satellites (*clusters*), able to change formation according to mission requirements. It was noted that one of the advantages was the reliability of the system, since the possible loss of one of the satellites could be "absorbed" by the remaining ones, so that the overall impact of the damage did not cause the end of the mission. Unfortunately, the project was cancelled in 2003 due to excessive cost increases.

The increased scientific return and the potential adaptability of formation flying satellites to changing mission goals have created new opportunities for the scientific endeavor. However, the current control, measurement and

modeling challenges of spacecraft FF have rendered some of the proposed missions too costly. Thus, recent years have seen many proposed FF missions cancelled or transformed into technology-demonstration missions. Although there are not many operational missions with a large number of satellites in formation, several current missions require close interaction between two or more satellites and can therefore be considered formation flying missions. Two such missions are *CLUSTER*, developed by the European Space Agency (ESA), and *GRACE*, the result of a collaboration between NASA and ESA.

CLUSTER was first proposed in November 1982 and was ready for launch in 1996. Unfortunately, the first four satellites were lost during the Ariane Flight 501 ascent from Kourou, French Guiana, on June 4, 1996. The second Cluster mission was launched in two sets of two satellites each on July 16 and August 9, 2000 [7]. The Cluster mission comprises four satellites (their names are *Rumba*, *Salsa*, *Samba* and *Tango*) launched into large, highly elliptical polar orbits around the Earth, with perigee and apogee altitudes of 19,000 km and 119,000 km, respectively. These spacecraft fly in a tetrahedral formation and collect detailed data on small-scale changes in near-Earth space, and on the interaction between the charged particles of the solar wind and Earth's magnetosphere. This has enabled scientists to build a 3D model of Earth's magnetosphere and to better understand the processes taking place inside it. The four satellites carry identical sets of 11 instruments to investigate charged particles and electrical and magnetic fields. In 2015, the mission celebrated 15 years in orbit and is one of ESA's missions that have generated the highest amount of scientific publications [7]. The mission has been extended to 2022 [8]. The GRACE (Gravity Recovery And Climate Experiment) mission [9] is one of the classic missions in which the formation is called a *trailing formation*. Trailing formations are formed by several satellites orbiting on the same path, in which each of them follows the previous one and is separated from it thanks to a specific time interval. The purposes are very varied, for example the observation of the same target at different times or with different angles of view. The GRACE mission features two identical satellites in a leader/follower formation (GRACE A and GRACE B, Fig. 1.2) orbiting the Earth on the same orbital plane. The

purpose of this mission has been to generate high-fidelity modeling of Earth's gravitational field, leading to an improvement of several orders of magnitude in gravity measurements. The two GRACE satellites were launched from the Pleseck cosmodrome in Russia on March 17, 2002. Initially designed to last five years, the mission was extended to eight years in 2005 and then further rescheduled until 2015, two years before being finally decommissioned in 2017. Grace is considered one of the successful missions not only among FF missions but among scientific analysis missions in general. The experience gained with it led to a second mission of the same type, called *GRACE-FO* (Grace Follow-On), launched on May 22, 2018 aboard a Falcon 9 rocket from the U.S. Vandenberg Air Force Base. The chosen orbit and design are very similar to those of its predecessor. Over its planned 5-year life, GRACE-FO will continue to monitor Earth's gravity field and climate, including adding GPS antennas needed to build profiles of atmospheric temperature and water vapor.

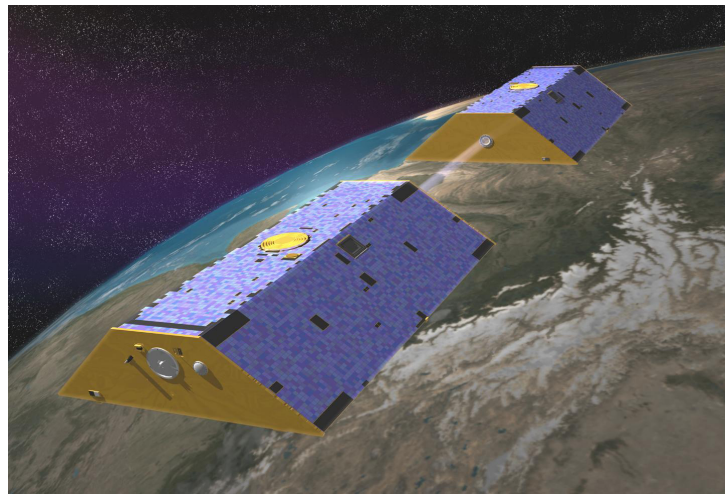


Figure 1.2: Rendering of the GRACE mission.

The first real mission designed to study formation flight was PRISMA, funded by a collaboration between Sweden and CNES. It comprises two satellites (*Mango* and *Tango*, 145 kg and 50 kg) flying together, equipped with an autonomous collision avoidance system. The mission officially began on June 15, 2010 with a Dnepr rocket launch from the Dombarovsky Cosmodrome,

Russia.

Another ESA mission that features an interaction between two spacecraft is *PROBA-3*, part of the *In orbit Technology Demonstration Programme*. The purpose of the program is to test new technologies able to exploit the benefits of on-board autonomy, i.e. the ability to perform many operations in complete autonomy drastically reducing operations from the ground. PROBA-3 is actually the fourth mission of the PROBA program and will see a pair of satellites of about 300 kg each, flying at 150 m from each other in a very elliptical orbit (eccentricity equal to 0.811, apogee at 60530 km). Their task will be to analyze the solar corona, placing the largest satellite equipped with a telescope behind the second and taking advantage of the artificial eclipse produced by the latter. The planned duration of the mission is two years, with launch scheduled for the beginning of 2023 [10].

A more ambitious project was the *DARWIN* mission [11], which envisioned the creation of four to five 1.5 m diameter telescopes arranged in formation to search for extra-solar Earth-like planets. Due to high costs and technological complexity, the development of the mission ended in 2007, before its conclusion. The same fate befell the *XEUS* (X-ray Evolving Universe Spectroscopy) mission project, which included two satellites, but the engineering effort merged into the larger *ATHENA* (Advanced Telescope for High Energy Astrophysics) project.

Of course, also NASA has proposed in recent years several missions that are based on the technology of spacecraft formation flying. An important collaboration between NASA and ESA is the basis of the mission *LISA* (Laser Interferometer Space Antenna). LISA consists of 3 artificial satellites placed at the vertices of an equilateral triangle, separated from each other by a distance of 5 million kilometers. The purpose of the project is to detect gravitational waves generated by systems of binary stars within the Milky Way, supermassive black holes in other galaxies and their fusion. Using a laser interferometer, the mutual distance will be accurately measured, and any very small changes can be attributed to passing gravitational waves. The launch date is scheduled for 2034 with an operational life of five years. ESA will design the probes while NASA will provide the launcher to put them

into orbit. ESA's *LISA Pathfinder* satellite was launched on December 3, 2015 and will help test technologies that will later be used in the three LISA satellites.

Another important mission developed by NASA is the *Magnetospheric Multiscale Mission* (MMS). It aims to study the Earth's magnetosphere, exploiting four satellites in tetrahedral formation with variable size (Fig. 1.3). It was successfully launched on March 13, 2015, and as of today (2021) is still operational. The formation is maintained through the use of a high-altitude GPS receiver, *Navigator*, to provide orbit knowledge, and regular formation maintenance maneuvers.

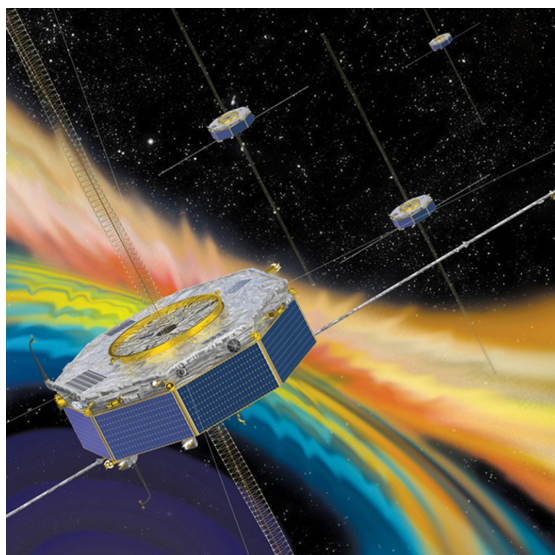


Figure 1.3: Illustration of the four MMS spacecraft in orbit in Earth's magnetic field.

A NASA project that has some similarities with PROBA is *New World Mission* (NWM) dedicated to the search for exoplanets, in particular the New World Observer mission. The basic idea is to exploit a spacecraft to occult the light from nearby stars to observe the planets orbiting them. The mission, which could take advantage of the modern JWST (James Webb Space Telescope), is currently under development and has already requested a larger investment of funds.

The missions outlined are just a few of the most important that have

been conceived by government space agencies. They testify to the affirmation of a technology that is now tested but still shows wide margins of development. The main limits that have led to the closure of some programs are due to economic restrictions, sometimes born from prejudices: its implementation appears in fact too expensive or too complicated [12]. A mitigation of this phenomenon is provided by the affirmation of small satellites (micro/nano/pico-satellites), which are very well suited for formation spaceflight. Small Satellites are more accessible to companies of all types and sizes, have more affordable prices, shorter development times, more up-to-date technology, smaller size and weight, provide risk distribution and more flexible services, and greater independence and control over the project. Thus, small satellites are enabling multi-satellite missions that were not otherwise possible because of their small size and modular nature. Missions with multiple small satellites can deliver a comparable or greater mission capability than a monolithic satellite, but with significantly enhanced flexibility and robustness [13] [14]. For all these reasons, it is very likely that spacecraft formation flying will increasingly involve the use of smaller, more adaptable and less expensive platforms. In fact, this work is based on these premises, which are further described in the following section.

1.5 Scope of this work and thesis outline

This dissertation work is part of the study of spacecraft formation flying presented in the previous paragraphs. The main task was the analysis of the behavior of a specific formation of satellites currently being studied at NASA’s Jet Propulsion Laboratory. The specific case study includes four small satellites (*deputies*) in tetrahedral formation, which describe an orbit around the main spacecraft (*chief*). The set objective is to maintain the original shape of the formation, which must remain as unaltered as possible throughout the mission. The reasons for this requirement can be attributed to scientific tasks or on-orbit servicing. In the baseline scenario the primary satellite is positioned in Low Earth Orbit, but one of the secondary objectives of the work is the understanding of the system response, under controlled

and uncontrolled conditions, in orbit around primary bodies other than the planet Earth. In particular, analyses have been performed taking into account one of the largest asteroids in the asteroid belt, Vesta. A preliminary analysis by means of simulations was then performed to verify the natural dynamics of the system. It is subject to perturbations peculiar to the space environment such as the effect of J_2 , which is more or less intense depending on the primary body, and atmospheric drag, whose presence greatly affects lower Earth orbits. This type of analysis is the subject of Chapter 3 of this research.

Chapter 2 provides the main theoretical tools needed to understand the phenomenon, as well as the equations that govern the dynamics of systems such as spacecraft formations. Formation maintenance, on the other hand, is also studied in more detail in Chapter 3. In order to obtain an unaltered arrangement of spacecraft and counteract the natural evolution of the system, it is necessary to apply low-thrust maneuvers independently for each of the deputies. The optimization of such maneuvers by *ad-hoc* algorithms is necessary since the propellant on board such satellites is limited. Attitude control, not studied here, is relegated to more in-depth analysis, where the exact knowledge of the systems installed on the spacecraft is fundamental.

The last chapter will discuss in more detail the effects of any changes in formation geometry and aerodynamic drag depending on the altitude considered. The behavior of the formation under analysis in the case of orbits around bodies other than the Earth is then shown and how changing certain parameters affects the final results.

The Matlab scripts used for the simulations and analysis are listed in the Appendix.

Chapter 2

Theoretical Background

In this chapter we review some notions of orbital mechanics, assuming that the reader already has prior knowledge of astrodynamics. We will then introduce the basics of relative spacecraft motion, starting with coordinate systems. The fundamental equations of orbital dynamics will be introduced. Finally, we will arrive at the exact and linearized equations of spacecraft formation flying. The last part of the chapter is dedicated to the general description of the case study that has been developed in this dissertation, while the simulations conducted will be the focus of the next chapter.

In this work vectors will be denoted by bold lower case letters (\mathbf{x}) and matrices by bold upper case letters (\mathbf{A}). The time derivative of a vector will be denoted by $(\dot{\cdot})$ and the second time derivative by $(\ddot{\cdot})$. The state vector of a certain satellite will be denoted as a column vector consisting of the position vector \mathbf{r} and the velocity vector \mathbf{v} concatenated together.

$$\mathbf{x} = \begin{pmatrix} \mathbf{r} \\ \mathbf{v} \end{pmatrix} = (\mathbf{r} \ \mathbf{v})^T \quad (2.1)$$

In this discussion we will often mention the satellite *chief* and one or more *deputies* satellites. In general, the equations will specify which specific satellite is being referred to. If this is not possible, the notation used for the chief and the deputies will be $(\cdot)_0$ for the first case and $(\cdot)_1$ for the second.

2.1 Coordinate systems

Problems that involve kinematics of physical quantities require a definition of reference frames, giving rise to coordinate systems, which the rates can be referred to. The study of problems in orbital mechanics usually requires the definition of a few coordinate systems. Many reference systems can be defined, each of which suits best in a given scenario. The reference systems useful to our discussion are presented below.

2.1.1 ECI reference frame

The state vector in the inertial system, which is fixed to the primary body, describes the absolute motion of a satellite with respect to that. The local frame is fixed to the formation and thus able to describe the relative distances and velocities between the satellites. The inertial frame used throughout this work is \mathcal{I} , a Cartesian, rectangular, dextral (CRD) inertial coordinate system, centered at the gravitational body (primary). In our case, since the primary body will be the Earth, unless otherwise specified, we can refer to it as a *geocentric* system. A geocentric system is centered at the Earth, the fundamental plane is the equator, the unit vector $\hat{\mathbf{x}}$ is directed from the Earth's center along the vernal equinox, $\hat{\mathbf{z}}$ is normal to the fundamental plane, positive in the direction of the geographic north pole, and $\hat{\mathbf{y}}$ completes the setup (see Fig. 2.1). This reference frame is usually referred to as Earth-Centered Inertial (ECI). An inertial system is used to define the satellite's position and velocity vectors, as well as the right ascension, α_r , and the declination, δ_d . The angle α_r is measured from the vernal equinox to the projection of \mathbf{r} onto the equatorial plane, whereas δ_d is measured from the same projection to \mathbf{r} .

The state vector \mathbf{x} of a satellite in this frame is defined by Equation (2.1).

$$\mathbf{x} = [x \ y \ z \ \dot{x} \ \dot{y} \ \dot{z}]^T = [x \ y \ z \ v_x \ v_y \ v_z]^T \quad (2.2)$$

The distance from the centre of the Earth is $r = \|\mathbf{r}\| = \sqrt{x^2 + y^2 + z^2}$. The

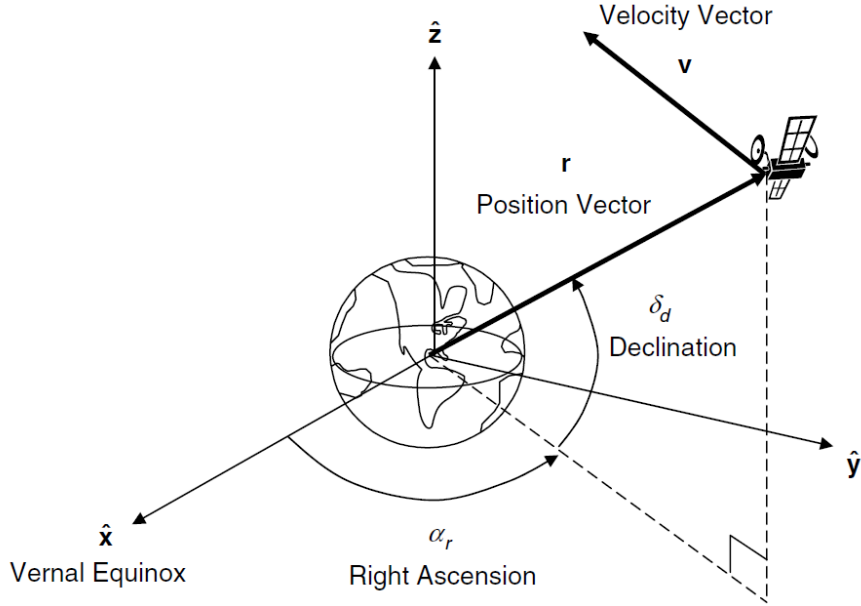


Figure 2.1: ECI Reference Frame. The origin is placed on the primary body and the system does not rotate [image taken from [3]].

angular momentum of the satellite, vector \mathbf{h} , which is normal to the position and the velocity vector, is given by

$$\mathbf{h} = \mathbf{r} \times \dot{\mathbf{r}} \quad (2.3)$$

2.1.2 Euler-Hill Frame

In order to deal more easily with the topic of relative motion between satellites, it is useful to define another reference system, local and centered on the spacecraft. We define then \mathcal{L} , a CRD *local-vertical, local-horizontal* (LVLH) rotating coordinate system, which has its origin in the satellite's centre of mass. The fundamental plane is the orbital plane. The unit vector $\hat{\mathbf{x}}$ is directed from the spacecraft radially outward, $\hat{\mathbf{z}}$ is normal to the fundamental plane, positive in the direction of the (instantaneous) angular momentum vector, and $\hat{\mathbf{y}}$ completes the setup (see Fig. 2.2). When a deputy satellite is viewed in the chief's \mathcal{L} -frame, the frame is called Euler-Hill-frame \mathcal{H} (or Hill-frame for brevity). Although there are those who suggest that

there are some differences between \mathcal{L} and \mathcal{H} , throughout this discussion we will refer to these two reference frames indistinctly.

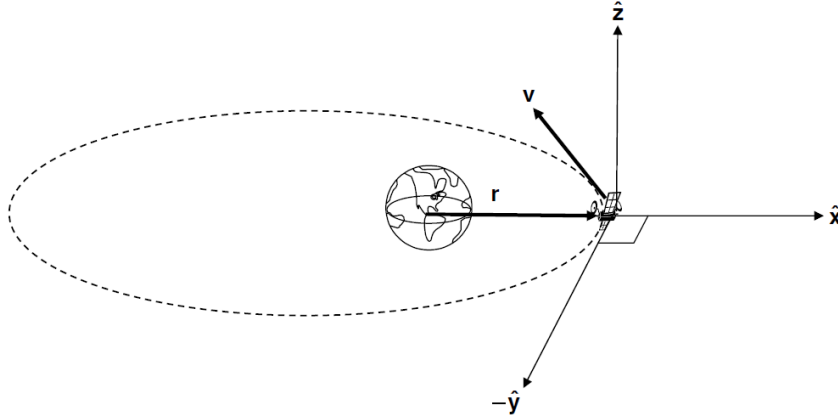


Figure 2.2: Local-Vertical, Local-Horizontal rotating coordinate system, centered at the spacecraft [image taken from [3]].

2.1.3 Polar Frame

In orbital mechanics it is useful to define another non-Cartesian reference system, as it greatly simplifies the analytical treatment of the equations involved. We can then define \mathcal{R} , a polar rotating coordinate system, centered at the primary. The fundamental plane is again the orbital plane. The unit vector $\hat{\mathbf{r}}$ is directed from the primary radially outward, and the angle θ is measured in the counterclockwise direction from some reference line, PQ , to \mathbf{r} (see Fig. 2.3). Taking advantage of this system, it is easy to observe the angle f , defined as the *true anomaly*, and the angle ω , the *argument of the periapsis*. The amplitude of the former is measured precisely from the position of ω . To overcome this dependence, we define the angle θ , the *argument of latitude*, defined as $\theta = \omega + f$. Through the angle θ it is more immediate to define the angular position of a satellite along its orbit.

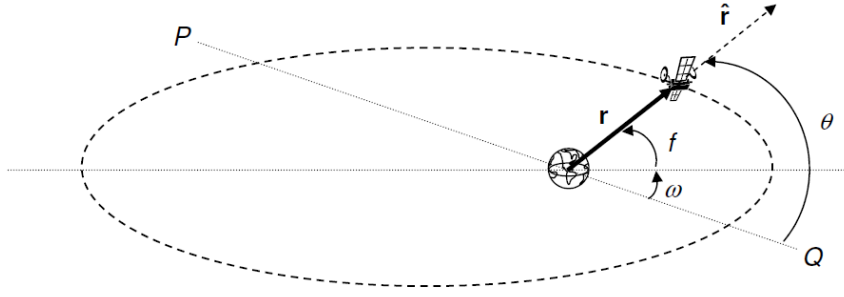


Figure 2.3: Polar coordinate system centered at the primary. Also shown are the angles f , ω and the argument of latitude θ [image taken from [3]].

2.1.4 Transformation between ECI and Hill-frame

Many applications involving formation control may require that a vector be transformed from \mathcal{L} to \mathcal{S} or vice versa. Given the \mathcal{S} frame representation of the position and velocity vectors of the chief, the transformation from \mathcal{L} to \mathcal{S} is given by this matrix

$$\mathbf{T}_{\mathcal{L}}^{\mathcal{S}} = [\hat{\mathbf{r}}_0 \quad (\hat{\mathbf{h}}_0 \times \hat{\mathbf{r}}_0) \quad \hat{\mathbf{h}}_0] \quad (2.4)$$

where $(\hat{\cdot})$ represents a unit vector. The inverse transformation can easily be obtained by using the matrix transpose operation; this leads to the following expression (the c and s stand for $\cos(\cdot)$ and $\sin(\cdot)$ functions).

$$\mathbf{T}_{\mathcal{S}}^{\mathcal{L}}(\Omega, i, \theta) = \begin{bmatrix} c_{\Omega}c_{\theta} - s_{\Omega}s_{\theta}c_i & s_{\Omega}c_{\theta} + c_{\Omega}s_{\theta}c_i & s_{\theta}s_i \\ -c_{\Omega}s_{\theta} - s_{\Omega}c_{\theta}c_i & -s_{\Omega}s_{\theta} + c_{\Omega}c_{\theta}c_i & c_{\theta}s_i \\ s_{\Omega}s_i & -c_{\Omega}s_i & c_i \end{bmatrix} \quad (2.5)$$

This matrix can be used to translate ECI coordinates to any satellite's LVLH-frame by using its corresponding position vector.

Throughout the discussion we will often refer to the deputy's state vector, defined by Eq. (2.2). Since we are dealing with the deputy, this is generally written according to the coordinates of the LVLH-frame, whose origin is located in the center of mass of the satellite chief. However, we may be interested in knowing the absolute orbit described by the deputy, which is completely defined by the state vector expressed in ECI coordinates. The

transformation involves the relative position of the deputy in the chief's frame, \mathbf{r}_d (expressed in \mathcal{L} -frame, see Fig. 2.4). First, we can write the absolute position of the deputy, expressed in the rotating frame coordinates.

$$\mathcal{L} \mathbf{r}_1 = \mathcal{L} \mathbf{r}_0 + \mathcal{L} \mathbf{r}_d = [(x + r_0), y, z]^T \quad (2.6)$$

Since we are interested in the deputy's absolute position in ECI coordinates, we express the vector in (2.6) in the \mathcal{I} -frame, using the transformation matrix described above.

$$\mathcal{I} \mathbf{r}_1 = \mathbf{T}_{\mathcal{L}}^{\mathcal{I}} \mathcal{L} \mathbf{r}_1 \quad (2.7)$$

We can proceed in the same way for the velocity vector, but in this case the absolute velocity of the deputy is not simply given by the vectorial sum of the velocity of the chief and that of the deputy. In fact, we must take into account the fact that the LVLH-frame is rotating around the primary body, causing additional velocity components to be present. The velocity vector, expressed in LVLH-coordinates, is then

$$\mathcal{L} \mathbf{v}_1 = \frac{d}{dt} \mathcal{L} (\mathbf{r}_d) + \frac{d}{dt} \mathcal{L} (\mathbf{r}_0) + \mathcal{I} \boldsymbol{\omega}^{\mathcal{L}} \times \mathbf{r}_0 + \mathcal{I} \boldsymbol{\omega}^{\mathcal{L}} \times \mathbf{r}_d \quad (2.8)$$

Substituting Eqs. (A.9), (A.10), (A.11) in Appendix into Eq. (2.8) yields

$$\mathcal{L} \mathbf{v}_1 = [v_x \ v_y \ v_z]^T = \begin{bmatrix} \dot{x} - \dot{\theta}_0 y + \dot{r}_0 \\ \dot{y} + \dot{\theta}_0(x + r_0) \\ \dot{z} \end{bmatrix} \quad (2.9)$$

Again, we want to express this vector using in ECI coordinates, using the same matrix as above.

$$\mathcal{I} \mathbf{v}_1 = \mathbf{T}_{\mathcal{L}}^{\mathcal{I}} \mathcal{L} \mathbf{v}_1 \quad (2.10)$$

Finally, we can write the deputy's state vector, expressed in ECI coordinates, which is (superscript \mathcal{I} has been omitted)

$$\mathbf{x}_1 = [\mathbf{r}_1 \ \mathbf{v}_1]^T \quad (2.11)$$

2.2 The Keplerian two-body problem

The two-body problem aims to find the solution of the equations of motion describing the dynamics of two bodies attracting each other in space. The analytical solution is based on some necessary assumptions: the only force acting on the bodies is that of gravity (for a Keplerian orbit there are no perturbative forces); the bodies are considered point-mass or spherical at the limit; the primary's mass is much larger than the orbiting body's mass; the gravitation force is Newtonian. Under these conditions, starting from Newton's second law ($\sum \mathbf{F} = m\mathbf{a}$), we can write the equation of Keplerian motion:

$$\ddot{\mathbf{r}} + \frac{\mu\mathbf{r}}{r^3} = \mathbf{0} \quad (2.12)$$

where \mathbf{r} is the position vector in ECI frame and $r = \|\mathbf{r}\|$.

In order to solve the equation (2.12), it is useful to perform a coordinate change and switch to the \mathcal{R} system. The change of coordinates for \mathbf{r} and its derivatives is omitted here, but can be found in the Appendix A.1. Following the change of coordinates, we obtain these two scalar equations.

$$\ddot{r} = r\dot{\theta}^2 - \frac{\mu}{r^2} \quad (2.13)$$

$$\ddot{\theta} = -\frac{2\dot{r}\dot{\theta}}{r} \quad (2.14)$$

From Eq. (2.14), knowing that $\mathbf{h} = \mathbf{r} \times \dot{\mathbf{r}} = r^2\dot{\theta}\hat{\mathbf{z}} = h\hat{\mathbf{z}}$, we observe that

$$\frac{d}{dt}(r^2\dot{\theta}) = r(r\ddot{\theta} + 2\dot{r}\dot{\theta}) = 0 \quad (2.15)$$

Equation (2.15) actively demonstrates that for Keplerian orbits the angular momentum vector remains constant ($\dot{\mathbf{h}} = \mathbf{0}$, *conservation of angular momentum*), both in its magnitude and in its components in the inertial space.

Let us recall at this point the energy equation, which can be derived starting from Eq. (2.13), without showing the mathematical steps. They are however available in the Appendix A.2.

$$\mathcal{E} = \frac{\dot{r}^2}{2} + \frac{h^2}{2r^2} - \frac{\mu}{r} = \frac{\dot{r}^2}{2} + \frac{(r\dot{\theta})^2}{2} - \frac{\mu}{r} = \frac{v^2}{2} - \frac{\mu}{r} \quad (2.16)$$

Using both constants of motion, we are now able to write the equations of motion in polar coordinates

$$\dot{r} = \sqrt{2\left(\mathcal{E} + \frac{\mu}{r}\right) - \frac{h^2}{r^2}} \quad (2.17)$$

$$\dot{\theta} = \frac{h}{r^2} \quad (2.18)$$

Although the equations (2.17) and (2.18) describe orbital motion with time as the independent variable, we are interested in having a more explicit relation of the trajectory followed by the orbiting body, in the form $r = r(\theta)$. Again, we choose to omit the steps that lead to writing the solution in the desired form. Dividing Eq. (2.17) by Eq. (2.18), we obtain a separable variable differential equation, the solution of which is given below (Eq. (2.19)). The initial condition necessary to solve the equation is provided by the parameter ω , which is the *argument of the periapsis*.

$$r = \frac{h^2/\mu}{1 + \sqrt{1 + 2\mathcal{E}h^2/\mu^2} \cos(\theta - \omega)} \quad (2.19)$$

We then achieved an important result, the famous *conic equation* in polar coordinates, which describes the trajectory of a body subject to the force of gravity in space, or Keplerian orbit. The Eq. (2.19) is often written in a more simplified form.

$$r = \frac{p}{1 + e \cos f} \quad (2.20)$$

where

$$p = h^2/\mu \quad e = \sqrt{1 + 2\mathcal{E}h^2/\mu^2} \quad f = \theta - \omega \quad (2.21)$$

are called respectively *semilatus rectum*, *eccentricity* and *true anomaly*. We can also define the parameter a

$$a = \frac{p}{1 - e^2} \quad (2.22)$$

which distinguishes between three different categories of orbits:

- *Ellipse*, a closed-orbit with $a > 0$ and $0 < e < 1$. In this case a is called *semi-major axis*. When $a = 0$ the ellipse becomes a *circle*;
- *Parabola*, an open-orbit with $a = \infty$ and $e = 1$;
- *Hyperbola*, an open-orbit with $a < 0$ and $e > 1$.

The Keplerian orbits can be similarly categorized in terms of the *total orbital energy*, \mathcal{E} . If we substitute the parameters in Eq. (2.21) into Eq. (2.16), we obtain

$$\mathcal{E} = -\frac{\mu}{2a} \quad (2.23)$$

The equation (2.23), in its relative simplicity and elegance, is of fundamental importance for orbital mechanics, since it tells us that the total energy held by a body describing a Keplerian orbit is a function only of the attractive body and the semi-major axis of the orbit. Using this parameter, we can obtain the same classification described above. Thus, for an ellipse ($0 < a < \infty$) $\mathcal{E} < 0$, for a parabola ($a = \infty$) $\mathcal{E} = 0$ and for a hyperbola ($-\infty < a < 0$) $\mathcal{E} > 0$.

We conclude this section with some important mathematical expressions. By differentiating the true anomaly with respect to time we obtain the angular velocity along a Keplerian orbit. For a Keplerian orbit, indeed, $\omega = \text{const.}$, and therefore $\dot{f} = \dot{\theta}$. We then obtain

$$\dot{f} = \sqrt{\frac{\mu}{a^3(1 - e^2)^3}}(1 + e \cos f)^2 \quad (2.24)$$

Eq. (2.24) is nothing more than the mathematical interpretation of Kepler's second law. As a matter of fact, it is observed that the angular

velocity of an orbiting body increases as it approaches the primary body and reaches a maximum at the point of periapsis ($f = 0$). Vice versa, the minimum of the angular rate is obtained at the apoapsis ($f = \pi$). The average angular rate (sometimes denoted by ω_Z or n), which is also instantaneous in the case of circular orbits, is obtained by placing $e = 0$ in Eq. (2.24).

Finally, we recall the expression for the orbital period, obviously valid only for closed orbits (elliptical and circular).

$$T = 2\pi\sqrt{\frac{a^3}{\mu}} \quad (2.25)$$

2.3 Spacecraft relative dynamics

In this section we want to introduce the equations governing the dynamics of relative motion between satellites in absence of perturbations. They represent a fundamental element for conducting the analyses and simulations presented in the next chapter. In order to treat this subject we will refer to a spacecraft called *chief* and to another spacecraft called *deputy*, as stated at the beginning of the chapter. We recall that the subscript $(\cdot)_0$ is used for the chief and $(\cdot)_1$ is used for the deputy. We will start with the description of the relative motion in \mathcal{S} and then transform the equations into \mathcal{L} , the LVLH rotating frame.

Neglecting any perturbing forces and assuming a spherical Earth, the motion of the chief satellite in \mathcal{S} -frame is fully described with the restricted two-body problem (Keplerian equation of motion, Eq. (2.12)):

$$\ddot{\mathbf{r}}_0 = -\frac{\mu}{r_0^3}\mathbf{r}_0 \quad (2.26)$$

where

$$r_0 = \|\mathbf{r}_0\| = \frac{p_0}{1 + e_0 \cos f_0} = \frac{a_0(1 - e_0^2)}{1 + e_0 \cos f_0} \quad (2.27)$$

In the same way we can write the Keplerian equation for the deputy

satellite

$$\ddot{\mathbf{r}}_1 = -\frac{\mu}{r_1^3}\mathbf{r}_1 \quad (2.28)$$

where

$$r_1 = \|\mathbf{r}_1\| = \frac{p_1}{1 + e_1 \cos f_1} = \frac{a_1(1 - e_1^2)}{1 + e_1 \cos f_1} \quad (2.29)$$

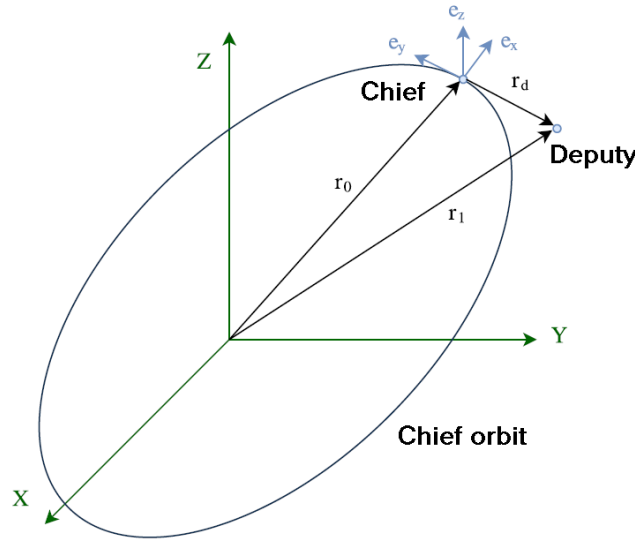


Figure 2.4: \mathcal{I} -frame and \mathcal{L} -frame. ECI is depicted in green, LVLH in blue.

We can denote the position of the deputy relative to the chief (Fig. 2.4) as

$$\mathbf{r}_d = \mathbf{r}_1 - \mathbf{r}_0 \quad (2.30)$$

Subtracting Eq. (2.26) from Eq. (2.28), the relative equation of motion becomes

$$\ddot{\mathbf{r}}_d = -\frac{\mu(\mathbf{r}_0 + \mathbf{r}_d)}{\|\mathbf{r}_0 + \mathbf{r}_d\|^3} + \frac{\mu}{r_0^3}\mathbf{r}_0 \quad (2.31)$$

Using the equations that express the relative acceleration in frame \mathcal{L} , Alfriend et al. [3] state Eq. (2.31) in terms of components in Euler-Hill-frame. We omit the intermediate steps, which we report in the Appendix A.3.

$$\ddot{x} - 2\dot{\theta}_0\dot{y} - \ddot{\theta}_0y - \dot{\theta}_0^2x = -\frac{\mu(r_0 + x)}{[(r_0 + x)^2 + y^2 + z^2]^{\frac{3}{2}}} + \frac{\mu}{r_0^2} \quad (2.32a)$$

$$\ddot{y} + 2\dot{\theta}_0\dot{x} + \ddot{\theta}_0x - \dot{\theta}_0^2y = -\frac{\mu y}{[(r_0 + x)^2 + y^2 + z^2]^{\frac{3}{2}}} \quad (2.32b)$$

$$\ddot{z} = -\frac{\mu z}{[(r_0 + x)^2 + y^2 + z^2]^{\frac{3}{2}}} \quad (2.32c)$$

Equations (2.32), together with Eqs. (2.33) (same as Eqs. (2.13) and (2.14)),

$$\ddot{r}_0 = r_0\dot{\theta}_0^2 - \frac{\mu}{r_0^2} \quad (2.33a)$$

$$\ddot{\theta}_0 = -\frac{2\dot{r}_0\dot{\theta}_0}{r_0} \quad (2.33b)$$

constitute a 10-dimensional system of nonlinear differential equations. This system has a single equilibrium at $x = y = z = 0$ and infinitely many equilibria for circular chief orbits. This means that, for a given elliptical orbit, the deputy spacecraft will appear stationary in the chief frame if and only if their positions coincide (situation with no practical value). On the other hand, for $e_0 = 0$ every position on the chief's orbit is a stable point and the two spacecraft are in a co-orbital motion. Although simplifications introducing changes in the independent variable have been proposed, this system is not solvable analytically. Its numerical resolution, however, is of great interest since these equations represent the exact dynamics of spacecraft relative motion, in the ideal case without perturbations. Furthermore, this system is the basis for the linearized models of the equations, presented in the next section.

2.4 Linearization of relative motion equations

In this section we aim to present a linearized model of the equations introduced in the previous section under the two-body assumption. The linearized model of the relative motion equations has found wide use in the analysis, design and control of spacecraft formations. Their peculiarity consists in the fact that, under appropriate assumptions related to the chief orbit, it is possible to find an analytical solution of the problem. These equations have been also used as inputs for linearized relative motion models to find state transition matrices (STMs) for relative motion. With these STMs, the evolution of the relative state may be predicted. The relative orbit propagation model we're about to present is a rather simple solution, where orbit eccentricity and perturbations are neglected.

In the previous section we derived the general nonlinear equations of relative motion for arbitrary chief orbits. A simpler, autonomous, form of the relative motion equations can be derived, however, if we assume that the chief follows a circular orbit. In many practical cases this is a realistic assumption. Thus, we recall the Eqs. (2.32) but we assume a circular orbit, so $r_0 = a_0 = \text{const.}$, $\dot{\theta}_0 = n_0 = \text{const.}$, $\ddot{\theta}_0 = 0$. This lead to

$$\ddot{x} - 2n_0\dot{y} - n_0^2x = -\frac{\mu(a_0 + x)}{[(a_0 + x)^2 + y^2 + z^2]^{\frac{3}{2}}} + \frac{\mu}{a_0^2} \quad (2.34a)$$

$$\ddot{y} + 2n_0\dot{x} - n_0^2y = -\frac{\mu y}{[(a_0 + x)^2 + y^2 + z^2]^{\frac{3}{2}}} \quad (2.34b)$$

$$\ddot{z} = -\frac{\mu z}{[(a_0 + x)^2 + y^2 + z^2]^{\frac{3}{2}}} \quad (2.34c)$$

As previously anticipated, these equations admit an *equilibria continuum* for $\dot{x} = \dot{y} = \dot{z} = \ddot{x} = \ddot{y} = \ddot{z} = 0$ given by

$$z = 0, \quad (x + a_0)^2 + y^2 = a_0^2 \quad (2.35)$$

Equation (2.35) defines a circle that coincides with the chief's orbit, centered at $x = -a_0$, $y = 0$ which are the coordinates of the primary in frame \mathcal{L} . This result reflects the trivial physical observation that the deputy

spacecraft will appear stationary in a chief-fixed frame if the deputy is co-located on the circular orbit of the chief. This type of in-line relative motion is referred to as *coorbital motion*.

The previous equations of relative motion have been developed assuming that the chief's orbit is circular. If the deputy's orbit in the inertial space is only slightly elliptic and slightly inclined with respect to the chief's orbit, the motion of the deputy will appear very close to the chief in a chief-fixed frame, provided that the initial positions are first-order small. In this case, Eqs. (2.34) may be linearized about the origin of the chief-fixed frame \mathcal{L} , and the resulting motion may be solved in closed-form. The linearized equations of motion are called the *Hill–Clohessy–Wiltshire equations* (HCW) or *Clohessy–Wiltshire equations* (CW). These equations were developed by Clohessy and Wiltshire in the early 1960s to analyze spacecraft rendezvous [15]. There are a number of ways to develop and solve the CW equations. The method we present involves the development of the right-hand side of Eqs. (2.34) into a Taylor series expansion around the chief, as stated by Alfriend et al. [3]. We take only the first-order terms and we denote $n_0 = \sqrt{\mu/a_0^3}$, so we get

$$-\frac{\mu(a_0 + x)}{[(a_0 + x)^2 + y^2 + z^2]^{\frac{3}{2}}} \approx 2n_0^2x - n_0^2a_0 \quad (2.36a)$$

$$-\frac{\mu y}{[(a_0 + x)^2 + y^2 + z^2]^{\frac{3}{2}}} \approx -n_0^2y \quad (2.36b)$$

$$-\frac{\mu z}{[(a_0 + x)^2 + y^2 + z^2]^{\frac{3}{2}}} \approx -n_0^2z \quad (2.36c)$$

Substituting Eqs. (2.36) into Eqs. (2.34) and omitting the subscript 0 (angular rate and semi-major axis are those of the chief), we obtain the *HCW equations*, for the unperturbed case and without control accelerations.

$$\ddot{x} - 2n\dot{y} - 3n^2x = 0 \quad (2.37a)$$

$$\ddot{y} + 2n\dot{x} = 0 \quad (2.37b)$$

$$\ddot{z} + n^2z = 0 \quad (2.37c)$$

The previous equations can be written in matrix form using the state vector \mathbf{x} (see Eq. (2.2)).

$$\dot{\mathbf{x}}(t) = \mathbf{A}\mathbf{x}(t) \quad (2.38)$$

where \mathbf{A} is the system matrix, given by

$$\mathbf{A} = \begin{bmatrix} 0 & 0 & 0 & 1 & 0 & 0 \\ 0 & 0 & 0 & 0 & 1 & 0 \\ 0 & 0 & 0 & 0 & 0 & 1 \\ 3n^2 & 0 & 0 & 0 & 2n & 0 \\ 0 & 0 & 0 & -2n & 0 & 0 \\ 0 & 0 & -n^2 & 0 & 0 & 0 \end{bmatrix} \quad (2.39)$$

The solution to the problem may be formulated in terms of the state transition matrix (STM). The STM is the solution of the HCW equations and can be expressed in the form $e^{\mathbf{A}(t-t_0)}$. This lead to the analytic solution of HCW equations, given by the following relations:

$$x(t) = \left[4x(0) + \frac{2\dot{y}(0)}{n} \right] + \frac{\dot{x}(0)}{n} \sin(nt) - \left[3x(0) + \frac{2\dot{y}(0)}{n} \right] \cos(nt) \quad (2.40a)$$

$$y(t) = -[6nx(0) + 3\dot{y}(0)]t + \left[y(0) - \frac{2\dot{x}(0)}{n} \right] + \left[6x(0) + \frac{4\dot{y}(0)}{n} \right] \sin(nt) + \frac{2\dot{x}(0)}{n} \cos(nt) \quad (2.40b)$$

$$z(t) = \frac{\dot{z}(0)}{n} \sin nt + z(0) \cos(nt) \quad (2.40c)$$

$$\dot{x}(t) = \dot{x}(0) \cos(nt) + [3x(0)n + 2\dot{y}(0)] \sin(nt) \quad (2.40d)$$

$$\dot{y}(t) = -[6nx(0) + 3\dot{y}(0)] + [6x(0)n + 4\dot{y}(0)] \cos(nt) - 2\dot{x}(0) \sin(nt) \quad (2.40e)$$

$$\dot{z}(t) = \dot{z}(0) \cos(nt) - z(0)n \sin(nt) \quad (2.40f)$$

Looking at the equations reported here, a number of considerations can be made. First, we can see that linearization has decoupled the in-plane motion

from the out-of-plane motion (*cross-track* motion). This simple harmonic motion can be cancelled by setting as initial condition $z(0) = \dot{z}(0) = 0$.

The second consideration concerns the *along-track* component. The first term of the solution has a linear dependence on time t and this results in a drift that grows linearly with time, making the motion in the plane unstable. However, we observe how the term dependent on t can be canceled if we nullify its coefficient. This happens by imposing a particular value on the initial conditions, which satisfies the following relation.

$$\dot{y}(0) = -2nx(0) \tag{2.41}$$

Eq. (2.41) provides a sufficient condition for stable in-plane motion. However, we must emphasize that this stability follows from the linearization in the HCW equations and is therefore *local*. In fact there are other conditions that violate Eq. (2.41) but also guarantee a bonded motion between the satellites. This happens because they satisfy the constraint of the *energy matching condition*, which will be discussed in more detail in the next paragraph. The energy matching condition is in fact a global stability criterion. The HCW equations, by performing a linearization and therefore an approximation of the solution, actually limit the physics of the problem and introduce an inherent error. It follows that the HCW equations should be handled with care, aware that their applicability is limited in the chief's neighbourhood and not to every circular orbit. The main case study described in this work is suitable for the use of these equations, at least for a first analysis. The results obtained and other considerations will be the subject of the next chapter.

2.5 The energy matching condition

In section 2.3, the nonlinear equations describing the exact dynamics of the unperturbed relative motion between chief and deputy were derived (Eqs. (2.32)). The first question that is natural to raise is whether conditions exist that guarantee constrained motion between the satellites. The physics

of the orbits tells us that if the two vehicles orbit the same primary body, the distance between them cannot grow indefinitely. However, the necessary condition to have a periodicity of the relative motion is that the periods of the orbits of the spacecraft are commensurate, otherwise the relative motion would appear locally unbounded. Since we know that the periods of the orbits depend only on their energies, we can exploit a constraint called the energy matching condition to find periodic relative orbits. In spacecraft formation flying, the only interesting case is one that provides 1:1 commensurability. Our goal is then to find a set of initial conditions such that $\mathcal{E}_0 = \mathcal{E}_1$, i.e. the total specific energies of chief's and deputy's orbits are the same.

To implement the energy matching condition we need to recall the expression of the velocity of the deputy, expressed in the coordinates of the rotating frame (Eq. (2.9)). In the most general case the orbit of the chief is not circular, which is why in the following expressions we keep the term \dot{r}_0 .

$$\mathbf{v}_1 = [v_x \quad v_y \quad v_z]^T = \begin{bmatrix} \dot{x} - \dot{\theta}_0 y + \dot{r}_0 \\ \dot{y} + \dot{\theta}_0(x + r_0) \\ \dot{z} \end{bmatrix} \quad (2.9)$$

The total specific energy of the deputy spacecraft is the sum of the kinetic energy and the potential energy

$$\begin{aligned} \mathcal{E}_1 &= \frac{1}{2}v_1^2 - \frac{\mu}{r_1} = \frac{1}{2}(v_x^2 + v_y^2 + v_z^2) - \frac{\mu}{r_1} \\ &= -\frac{1}{2}\{(\dot{x} - \dot{\theta}_0 y + \dot{r}_0)^2 + [\dot{y} + \dot{\theta}_0(x + r_0)]^2 + \dot{z}^2\} - \frac{\mu}{\sqrt{(r_0 + x)^2 + y^2 + z^2}} \end{aligned} \quad (2.42)$$

The total specific energy of the chief can be simply written by referring to the semi-major axis of its orbit.

$$\mathcal{E}_0 = -\frac{\mu}{2a_0} \quad (2.43)$$

The energy matching condition ($\mathcal{E}_1 = \mathcal{E}_0$) is therefore

$$-\frac{1}{2}\{(\dot{x} - \dot{\theta}_0 y + \dot{r}_0)^2 + [\dot{y} + \dot{\theta}_0(x + r_0)]^2 + \dot{z}^2\} - \frac{\mu}{\sqrt{(r_0 + x)^2 + y^2 + z^2}} = -\frac{\mu}{2a_0} \quad (2.44)$$

This results in a constraint in the initial conditions of the deputy for a bounded relative motion, which is

$$-\frac{1}{2}\{[\dot{x}(0) - \dot{\theta}_0(0)y(0) + \dot{r}_0(0)]^2 + \{\dot{y}(0) + \dot{\theta}_0(0)[x(0) + r_0(0)]\}^2 + \dot{z}(0)^2\} - \frac{\mu}{\sqrt{[r_0(0) + x(0)]^2 + y^2(0) + z^2(0)}} = -\frac{\mu}{2a_0} \quad (2.45)$$

2.6 Case study description

After having outlined the fundamental concepts that govern the relative motion between satellites in formation, we can move more specifically into the case study analyzed in this thesis. As mentioned in the introduction, small satellites are no longer a primitive technology but a well-established reality and still with a great possibility of development. The applications of small satellites are numerous, but among them the on-orbit servicing technology has undergone a great advancement in recent years, driven by the growth of the commercial space sector [16]. To date, major on-orbit services include inspection, repair, refueling or upgrading of a target satellite already in orbit, typically of larger size [13].

For our study, we chose to consider a formation of small satellites capable of performing these tasks during their operational lifetime. Since the objective of the study is to analyze the behavior of the formation in the uncontrolled and controlled scenario, the exact characteristics of the space platform have not been defined, although these are certainly needed at a more advanced stage of mission development. A certain level of detail is however required in order to perform realistic simulations, which constitute the core of this work. The satellites that constitute the formation are small spacecrafts 3U

(see Fig. 2.5). Their wet mass is therefore 3 kg. Larger satellites offer more possibilities but with much higher cost, not only in terms of production but also in terms of maintenance in orbit due to the higher fuel demand. These dimensions are instead in the average of small satellites and are getting more and more common. Since for some simulations the effect of atmospheric drag has been taken into account, it becomes important to know also the cross sectional area of the spacecraft. The value that has been chosen is 0.03 m^2 , compatible with a 3U spacecraft.



Figure 2.5: Rendering of a potential 3U-Cubesat employed in the formation.

The formation under study in the baseline scenario consists of four deputies satellites located at the vertices of a regular tetrahedron and a chief satellite positioned at the center of this ideal tetrahedron. The ideal distance between chief and deputies is exactly 100 m. For geometric reasons, this implies that the ideal distance between deputies is 163.3 m. Such a formation is suitable for the tasks described above, e.g. the inspection of a cargo satellite before re-entry to Earth. By performing relative orbits around the chief spacecraft, the deputies satellites are able to take measurements or images of it quite easily. To accomplish their task it is required that the distances between the deputies and the chief are as constant as possible. The

objective is therefore to maintain the initial formation withing a tolerance with minimum amount of fuel consumption under J_2 and atmospheric drag perturbations.

For this study, the behavior of a similar formation, but consisting of three satellites, was also analyzed. In this case, the formation is planar and the deputies are arranged at the vertices of an equilateral triangle. The chief spacecraft is still positioned at the center of this triangle, at a distance of 100 m from each deputy. This implies that the separation between the deputies is 173.2 m. As will be seen in the next chapter, the dynamics of the two formations are different in some aspects and lead us to some interesting observations.

Regarding the absolute positioning of the formation in space, the mission objectives clearly define a Low-Earth Orbit (LEO). For these simulations, the chief satellite is therefore positioned in such an orbit. The specific orbital parameters of the reference orbit are given in Table 2.1. Since we are dealing with a circular orbit, the argument of perigee is not defined.

Orbital parameter	Value
a	6728.1363 km ($R_E + 350$ km)
e	0
i	0.9 rad
Ω	0 rad
ω	Not defined
θ	$\pi/4$ rad

Table 2.1: Chief’s orbit parameters (baseline scenario)

A separate discussion deserves the treatment of the nonlinear equations used for the simulations. In the previous sections, the nonlinear equations describing relative motion in the unperturbed case have been treated. However, one of the goals of this work is to observe the influence of the atmospheric drag and the Earth’s oblateness factor. These two types of perturbations are the main causes of spacecraft orbit drift in LEO. Of course, these are not the only perturbations of the space environment (by way of example, we recall the presence of the gravity of other bodies like the Moon, the solar radiation

pressure or the effects due to the presence of the Earth’s magnetic field), but considering that the orders of magnitude of the first two are vastly superior to the remaining ones, the minor perturbations can be neglected, without affecting the accuracy of the results.

Thus, there is a need for the use of a mathematical model that accounts for these effects. The first to introduce the influence of the parameter J_2 in the equations of the spacecraft formation flying were Xu and Wang at the end of the last decade [17]. A few years later, Morgan et al. started from Xu and Wang’s equations and proposed a model in which the drag caused by the atmosphere is also taken into account [18]. It consists of a system of 12 differential equations (6 for the dynamics of the chief and 6 for the dynamics of each deputy). It serves as the basis for the simulations performed and has been implemented in Matlab for its resolution. Of course, these equations are not solvable analytically, but they can be easily integrated numerically in order to observe the dynamics of the spacecraft involved. For the sake of brevity, the equations are not fully reported here but can be found in Appendices A and B of the reference [18]. It goes without saying that the cancellation of the atmospheric resistance and J_2 parameters leads back to the nonlinear equations already stated throughout this chapter. The only difference lies in the fact that the orbital parameters used in the chief’s dynamics equations are not the classical orbital parameters. They exploit some classical orbital parameters and other parameters typical of Cartesian coordinates (state vector). Such representation is usually referred to as *hybrid mode*. The conversion between the classical orbital parameters and the hybrid mode is not so complex and employs the position vector, the velocity vector and the angular momentum vector. For the sake of completeness, Table 2.2 shows the hybrid coordinates that uniquely describe the orbit of the chief in the baseline scenario.

Orbital parameter	Value
r_0	6728.1363 km ($R_E + 350$ km)
v_x	0
h_0	51786.46598 km ² s ⁻¹
Ω	0 rad
i	0.9 rad
θ	$\pi/4$ rad

Table 2.2: Chief's orbit hybrid parameters (baseline scenario)

Chapter 3

Formation Simulations

This chapter represents the core of the work presented. The objective is to present the simulations that have been conducted, as well as the results that have been achieved. The analysis have been carried out using mainly the software Matlab ©, exploiting scripts written specifically for the purpose.

3.1 Unperturbed case

The first phase of the work is to observe the dynamics of the formation in the absence of perturbations. As described in the previous chapter, the main perturbations are represented by the effect of the parameter J_2 (Earth's oblateness) and the presence of the atmosphere at low altitudes. In order to observe the natural dynamics, we therefore chose to omit these types of effects initially. The underlying idea is the numerical integration of the equations of motion (2.33) and (2.32). These equations are the exact ones that describe the dynamics of relative motion and do not take into account external perturbative factors. Since this is a system of differential equations (ODE), it is necessary to use a numerical solver. The function provided for this purpose is `ode45`, already integrated in Matlab. This type of solver, designed in particular to solve non-stiff equations, guarantees a good accuracy of the results together with a general stability of the method used.

In order to observe the behavior of the spacecraft in the short period, the

plots that are shown have been made considering simulations that include five orbits of the chief. The duration of the orbital period is easily derived from Eq. (2.25).

$$T = 2\pi\sqrt{\frac{a^3}{\mu}} = 5.492 \cdot 10^3 s \approx 91' 30s$$

One aspect that should not be underestimated is the initial condition of the deputies. In effect, they will take on a particular importance in the algorithm developed to keep the formation fixed. The calculation of the initial conditions of the deputies is performed by a script written specifically for this purpose (listing B.1). The initial positions are defined by considering the vertices of a regular tetrahedron (Figure 3.1), while the initial velocities are not arbitrarily chosen but they derive from the physics of the specific problem. The three position coordinates and three velocity components obtained thus constitute the initial state vector with which to initialize the simulations.

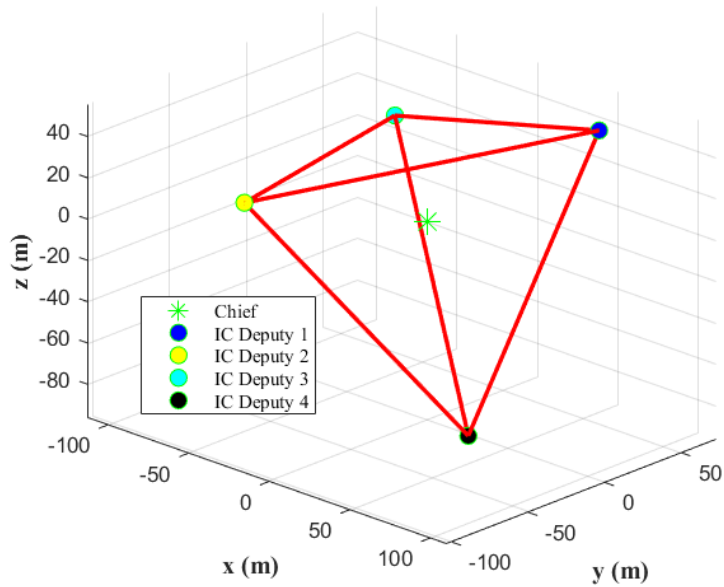


Figure 3.1: Initial positions of the deputies around the chief, forming the ideal tetrahedron.

The graphs describing the motion of the deputies with respect to the chief are shown in Figures 3.2, 3.3 and 3.4. The coordinates shown in the graphs are those of the \mathcal{L} -frame, in which the chief is placed at the origin of the axes and the positions of the deputies are given by referring to it. Using this coordinate system, the separation between the chief and the deputies is easily obtained from the following expression.

$$d_{1c} = \sqrt{x^2 + y^2 + z^2}$$

while the distance between two individual deputies (1 and 2, for example) is given by

$$d_{12} = \sqrt{(x_2 - x_1)^2 + (y_2 - y_1)^2 + (z_2 - z_1)^2}$$

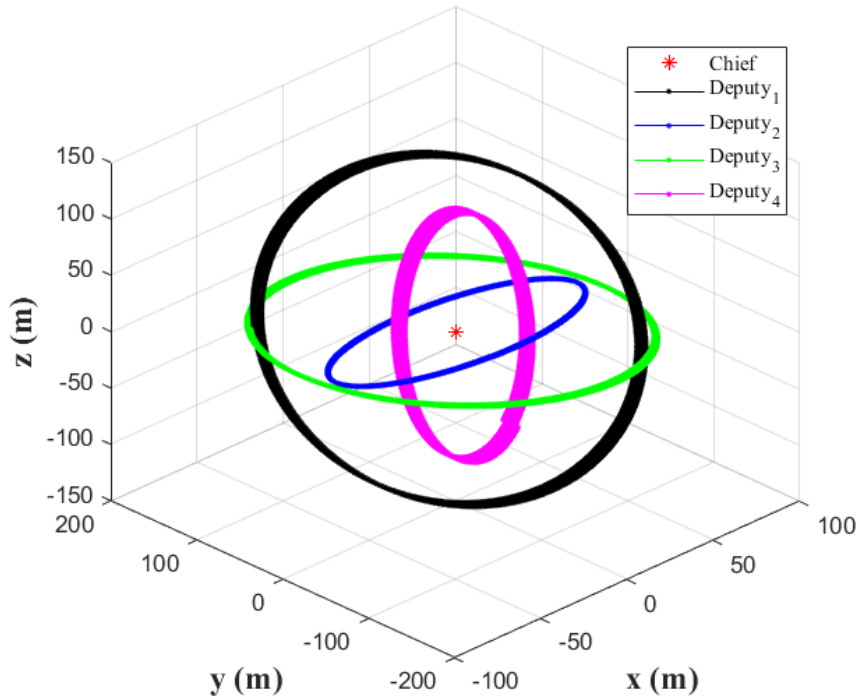


Figure 3.2: Relative orbits for the unperturbed case. The chief is located at the origin of the axes (LVLH-frame).

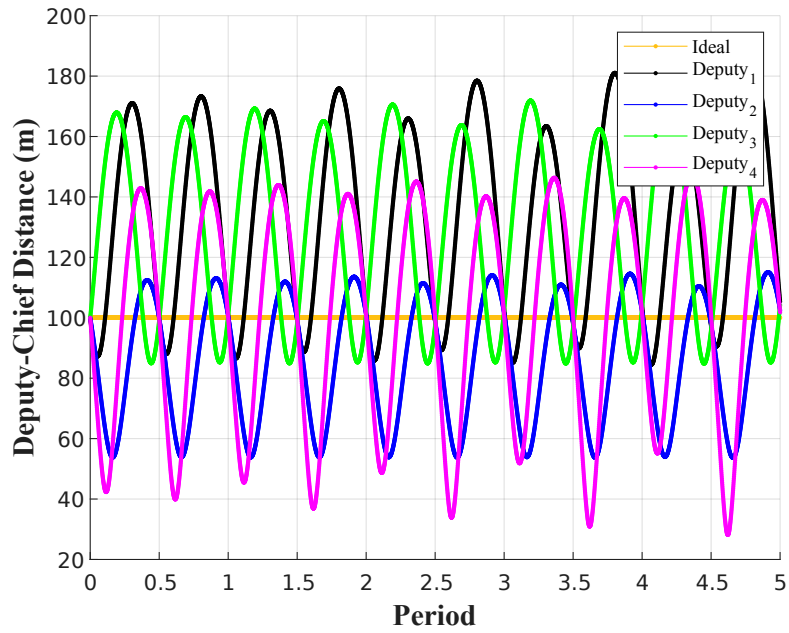


Figure 3.3: Distance between deputies and chief (unperturbed case).

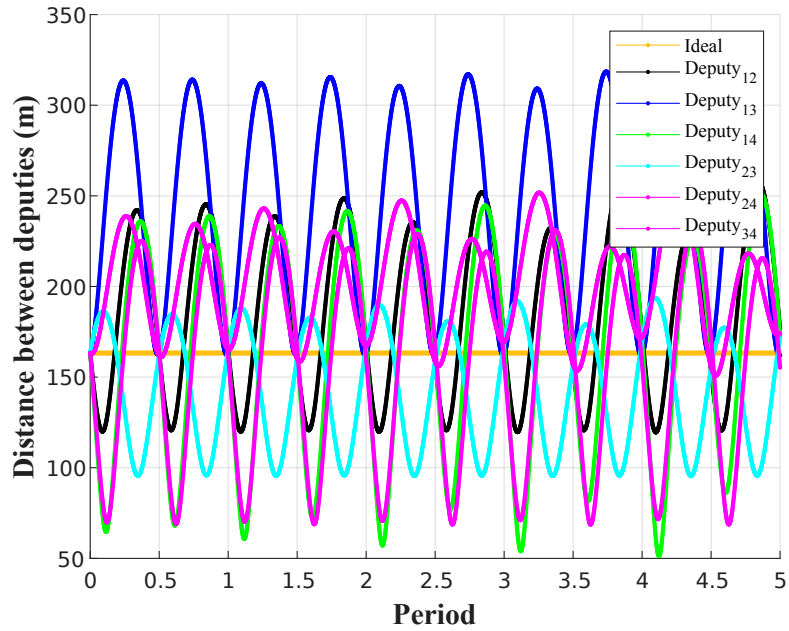


Figure 3.4: Distance between deputies (unperturbed case).

Even from a first observation, we can see that the natural dynamics of the deputies does not allow them to maintain a fixed position with respect to the chief. Indeed, their distance tends to oscillate repeatedly, with oscillations of the order of ten meters. Similarly, the distance between the deputies is not constant. The initial conditions of each deputy place them exactly at the vertices of the ideal tetrahedron that we seek to maintain and they ensure that there are no collisions between them or between them and the chief. However, the initial positions and velocities defining their orbit are also responsible for the behavior assumed during subsequent orbits.

3.2 Independent motion

In the previous section we made use of the nonlinear equations describing the dynamics of the relative motion between the deputies and the chief, referring to their coordinates in a non-inertial reference system, the LVLH-frame. In this system one can easily observe the relative orbit of each deputy around the chief, but can also lose sight of the physics of absolute motion. In fact, it is important to note that the relative orbits described by the deputies around the chief are the result of the interaction of the absolute motions of both satellites. The primary body is the Earth also for deputies, which describe an orbit that is only slightly different from that described by the chief.

Following this reasoning, it may be interesting to observe the problem from another point of view, that is the absolute motion of the deputies in space. Considering their initial conditions, it is indeed possible to integrate the equations of motion (Newton's law) and calculate the absolute trajectory of the deputies around the primary body. Of course, for consistency with the results previously obtained, also in this case we neglect the effects of any orbital perturbations. Unlike the previous case, however, the reference system used is no longer the \mathcal{L} -frame but the inertial reference system ECI (\mathcal{I} -frame). The transition from one reference system to the other one, involving the initial state vector of the deputies and chief, is the subject of the 2.1.4 section. The graphs resulting from this calculation are presented in

Figures 3.5, 3.6, and 3.7.

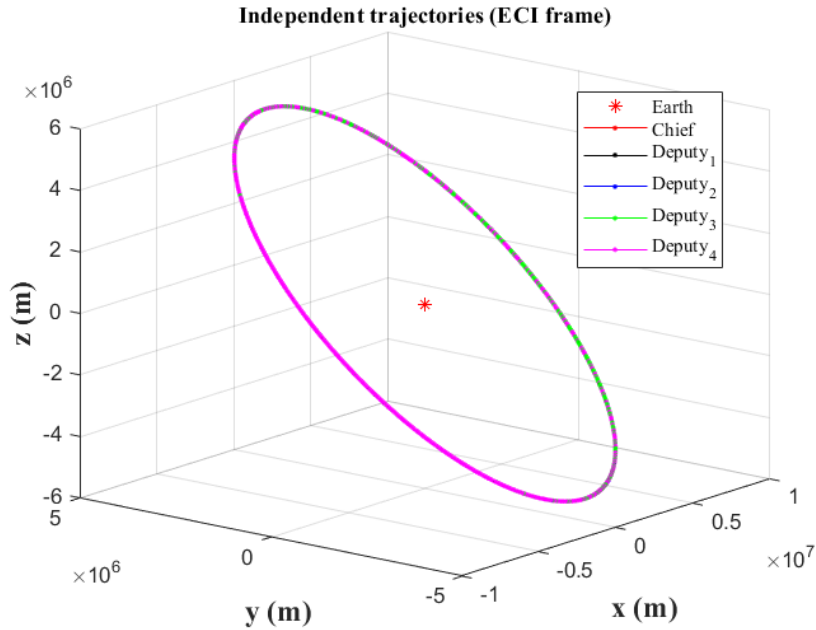


Figure 3.5: Absolute orbits of chief and deputies in ECI frame. Orbits of the deputies are slightly visible considering the global scale of the plot.

The charts shown refer to a period equal to 5 orbits of the chief, so as to keep the same number as in the previous case. As can be easily observed, the integration of Newton's law for each deputy individually leads to a result fully comparable to that obtained exploiting the equations of relative motion. Once again we note that the natural dynamics of spacecraft is characterized by frequent oscillations in the distance between deputies or between them and the chief, visible in Fig. 3.6 and Fig. 3.7. These distances are in effect independent of the choice of reference system, which is instead important in order to define the absolute orbit of the spacecraft. In Figure 3.5 it is well observed how the orbits of the five satellites are actually very close to each other, apparently indistinguishable when observed in the scale of the semi-major axis of the orbit.

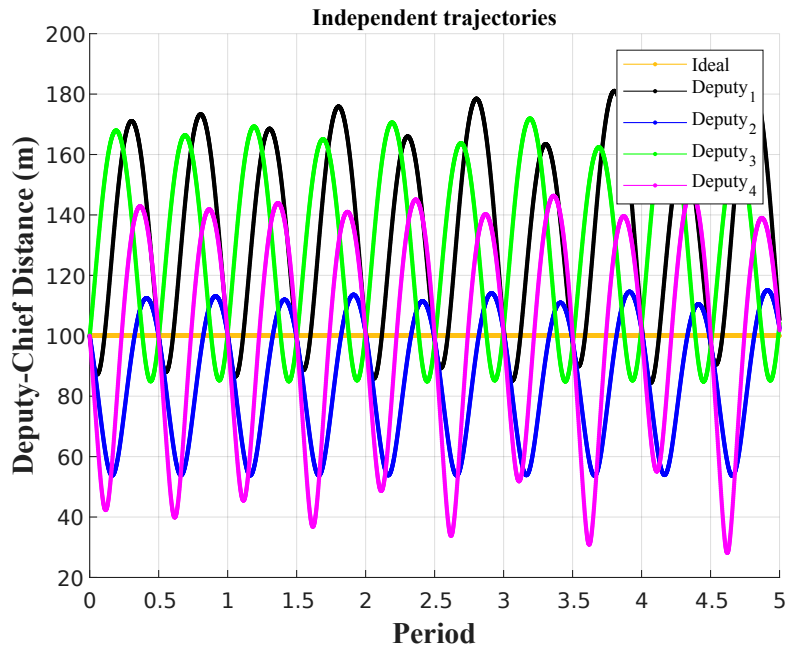


Figure 3.6: Distance between deputies and chief (independent trajectories).

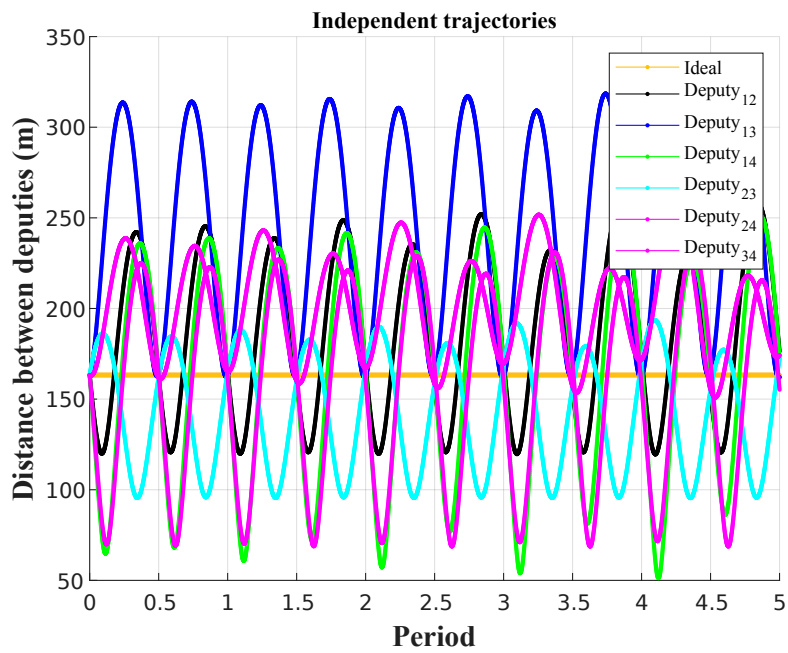


Figure 3.7: Distance between deputies (independent trajectories).

3.3 Clohessy-Wiltshire linearization

In section 2.4 we showed how, under appropriate assumptions, it is possible to linearize the equations of relative motion and thus find an analytical expression of their solution (Equations (2.40)). The case study presented here meets the criteria under which the Clohessy-Wiltshire equations can be applied, since the orbit of the chief is circular and the size of the formation is much smaller than the scale of the chief's orbit. Their accuracy is clearly restricted to a limited surround of the chief satellite, but the advantages offered are numerous. One of them is certainly the time required to perform the desired simulations. The integration of the equations of relative motion assumes the resolution of an ordinary differential equation. If it is true that Matlab or other commercial software propose algorithms tailored to the type of equation to be solved (in this case the function `ode45`), the resources used in this type of algorithms are always greater than those required for the simple representation of a function already known a priori. For this reason, the HCW equations prove to be a particularly convenient tool when it is necessary to observe the dynamics of spacecraft formation over a longer time horizon, which would normally require a lot of time to be simulated accurately. This strength, due to the linearization of the problem, is the reason why we chose to analyze spacecraft dynamics using the HCW equations.

Unlike previous cases, however, simulations are performed for a larger number of orbits, equal to 200. The goal is to maintain the same initial conditions for the deputies and observe the orbital dynamics for a higher time interval. The number of orbits is not chosen casually: 200 orbits correspond to approximately two weeks of time (12.71 days) and this duration seems suitable for the intended mission purposes. In general, if an OOS (On-Orbit Servicing) type mission is envisaged, two weeks are sufficient to guarantee the inspection of the payload before the re-entry into the Earth's atmosphere or a possible refueling of a customer satellite. The resulting graphs are shown in Fig. 3.8 and Fig. 3.10. Although the full simulation covers 200 orbits, the graphs shown refer only to the last 20 or 30 orbits for a better graphical visualization.

The first remark that can be noticed considering a longer period of time is the drift motion to which deputies are subjected. In addition to the continuous periodic variation in the distance between satellites, still present in this situation, it is observed that with the progress of the orbits also the average distance tends to increase significantly, reaching values close to 800 m between chief and deputies.

We remind the reader that the spacecraft are subjected to simple natural dynamics and no maneuver has been imposed on them so far, other than the initial one that determines the starting conditions. Unlike what will be presented later, this behavior cannot be due to the effects of any perturbations that tend to modify the orbit (the HCW equations do not consider at all any nonlinear phenomena such as J_2 or aerodynamic drag). However, this result is not unexpected. The theory lying behind the HCW equations predicts that the relative motion between satellites inevitably tends to diverge if the initial conditions are not precisely chosen (see section 2.4). Indeed, the simple application of the HCW equations does not assume the energy matching condition, which is a global stability condition. The same starting conditions chosen for the previous simulations produce a drifting motion and thus an instability inherent in the linearization of the problem. In any case, this instability can be cancelled if we impose the so-called *no-drift condition*, Eq. (2.41). By overwriting the previously chosen value for $\dot{y}(0)$ with the one imposed by Eq. (2.41), the output becomes trivial (Figures 3.9 and 3.11). The drift motion has disappeared and the oscillations in the distances are maintained at the same amplitude for each orbit (the oscillations are not visible due to the graphical scale chosen for the plots). It cannot be otherwise since the HCW equations thus become a simple combination of trigonometric functions. This result is nevertheless quite relevant because it gives us a possible way to overcome this issue (even if theoretical, because unfortunately in reality it is not possible to impose an initial condition without any experimental error).

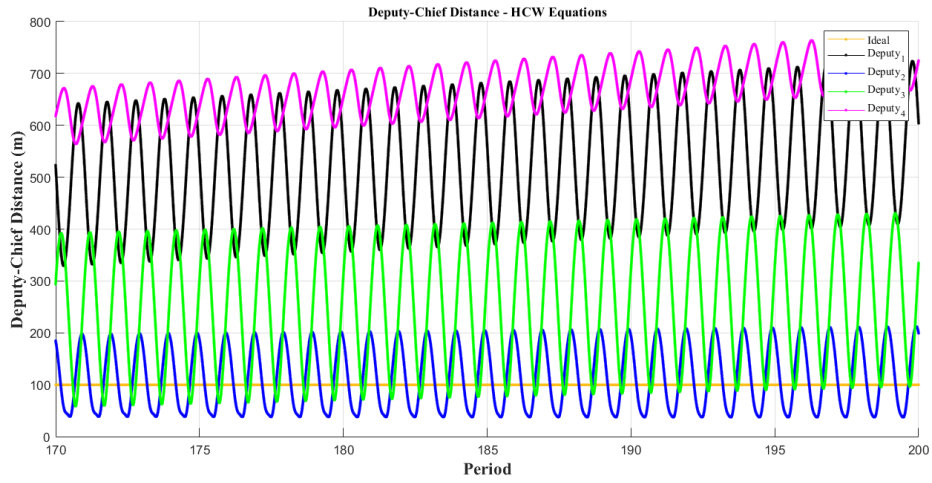


Figure 3.8: Distance between deputies and chief using HCW equations.

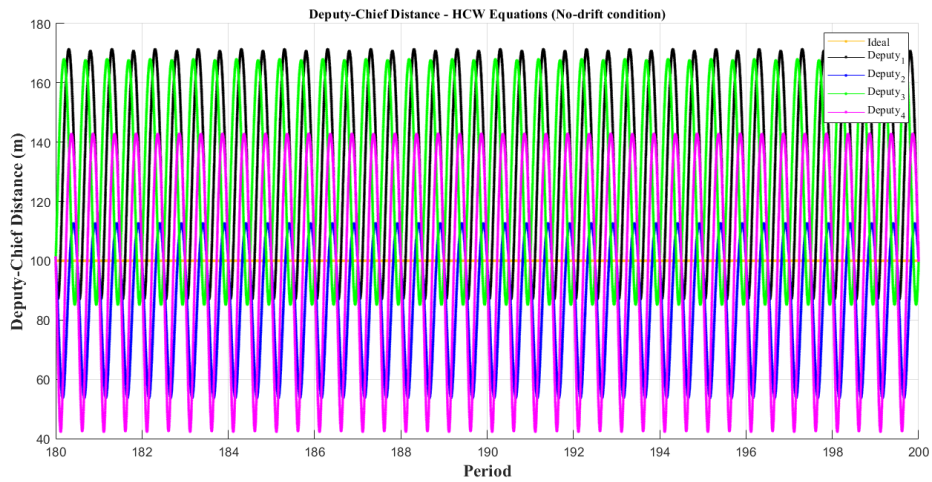


Figure 3.9: Distance between deputies and chief using HCW equations, with the no-drift condition. The output is a simple combination of trigonometric functions.

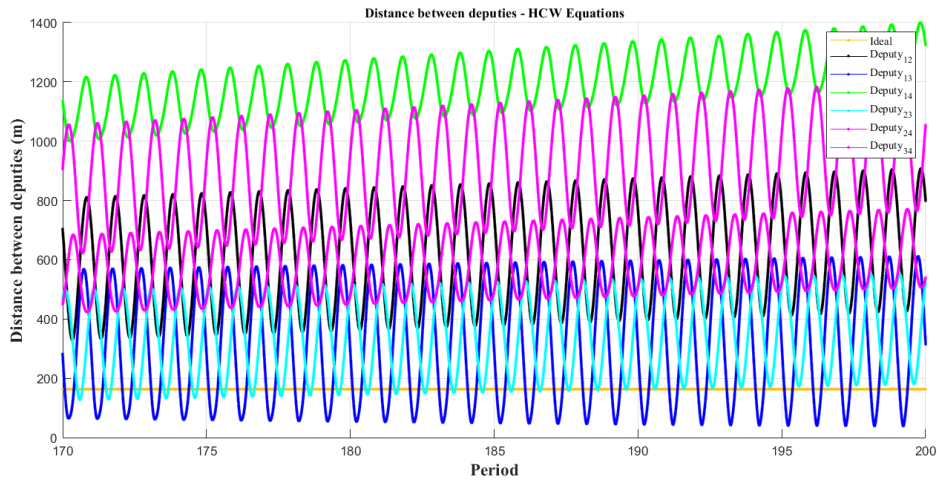


Figure 3.10: Distance between deputies using HCW equations.

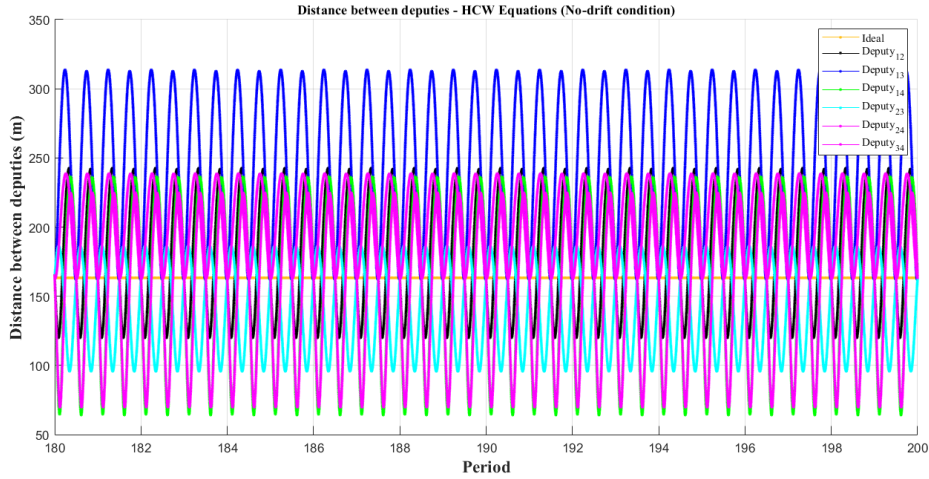


Figure 3.11: Distance between deputies using HCW equations, with the no-drift condition. The output is a simple combination of trigonometric functions.

3.4 Perturbed case

The next phase of our study involved a more detailed analysis of the kinematics of the tetrahedral formation. Up to this point, in fact, the non-linear equations of relative motion or the corresponding linearized equations have been contemplated, but both refer to an ideal scenario, where the force of gravity is the only one acting on the spacecraft. In this section we want to add the effect of the orbital perturbations described in the previous paragraphs, namely J_2 and aerodynamic drag, in the study of the baseline scenario.

As already stated, the Keplerian two-body problem predicts a perfectly spherical model of the attractor body, in this case the Earth, with a homogeneous density distribution. Actually, the planet Earth is neither spherical nor has a homogeneous mass distribution; rather, it has the following characteristics, found through satellite observations.

- Oblateness = $1/298.257$
- Eccentricity at the equator = $1.14 \cdot 10^{-5}$

Oblateness is defined as the difference between the equatorial radius and the polar radius, compared to the equatorial radius. The eccentricity of the equator is defined as the ratio between the half focal distance and the semi-major axis.

This obvious discrepancy, visible in Fig. 3.12, between the gravitational model of the Keplerian problem and the actual characteristics of the planet Earth is at the origin of the perturbative action linked to the asymmetries of the Earth's gravitational field. It appears, therefore, evident the necessity to define a more realistic model of Earth's gravitational field. In order to take into account the actual conditions of the Earth's gravitational field, a semi-analytical model of the Earth's potential is defined, taking into account the sphericity of the Earth, the ellipticity at the equator and other differences between the real gravitational field and the spherical gravitational field model. This potential is obtained from the gravitational field potential of a

perfectly spherical body to which is added a series of spherical harmonics satisfying Laplace's equation in empty space. The complete treatment of the Earth's gravitational potential and its mathematical expression is beyond the scope of this work. Thus, the model used takes into account only the effect of the harmonic J_2 , whose value is equal to $1.0826 \cdot 10^{-3}$. The next harmonic J_3 , which in itself would increase the model's accuracy, actually has a much more negligible contribution, being three orders of magnitude smaller ($J_3 = 2.5327 \cdot 10^{-6}$).

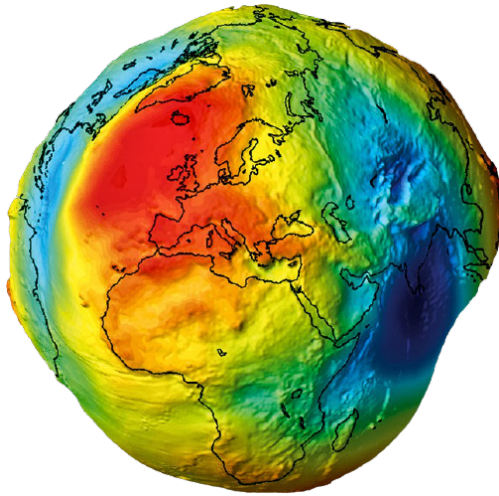


Figure 3.12: Earth geoid. Anomalies induced by the inhomogeneous mass distribution are clearly visible.

Atmospheric drag is a particularly significant perturbation for low orbits. The force acting on the satellite due to atmospheric drag is opposed to the relative velocity of the satellite, and changes the shape of the orbit. Since air density decreases rapidly with height, a satellite having a highly eccentric orbit will only suffer the effects of air resistance around perigee where, to a first approximation, it will lose velocity. This means that the satellite will not reach the same altitude as it did in the previous orbit at apogee. The apogee distance is reduced while the distance at perigee remains essentially constant. In other words, both the semi-major axis and eccentricity tend to decrease, resulting in a circularization of the orbit and a loss of operational altitude for the satellite.

A simple formulation of the perturbative acceleration due to atmospheric drag is as follows

$$\mathbf{a}_{\text{drag}} = \frac{1}{2}\rho\|\mathbf{V}_a\|\mathbf{V}_a\frac{A}{m}C_D \quad (3.1)$$

where, \mathbf{V}_a is the relative velocity vector of the satellite with respect to the atmosphere. The drag coefficient C_D depends on the shape and orientation of the satellite with respect to the satellite-atmosphere relative velocity direction. As mentioned in the previous chapter, the exact shape of the spacecraft involved has not been defined at this stage of the study, but given the use of small 3U-6U satellites, a value of $C_D = 0.5$ was chosen, which seems to be appropriate for this scenario. As it is evident from the expression (3.1), the acceleration due to atmospheric drag depends explicitly on the density; consequently, the choice of the atmospheric model to be used is particularly important to obtain a good estimate of the effects of the atmosphere on satellite motion.

The mathematical model used for the following simulations considers an air density at an altitude of 350 km equal to $\rho = 1.8796 \cdot 10^{-11} \cdot 10^9 \text{ kg/km}^3$. The effect of altitude and relative atmospheric density will be discussed in more detail in the next chapter. Another aspect to consider, related to this type of perturbation, is certainly the duration of the mission. For the previous simulations an OOS type mission objective was assumed, with an estimated operational lifetime of about 2 weeks. It is evident that a shorter time span is much less affected by the effects of these perturbations, if compared to longer duration missions. If this aspect does not cause particular problems on the absolute orbit of the chief (which is also already circular at the beginning), it is still crucial to take it into account when a high precision in maintaining the shape of the formation and the distance between spacecraft is required.

Figures 3.13, 3.14 and 3.15 show the graphs resulting from the simulations performed considering the orbital perturbations described. The simulation period was kept equal to 5 orbits of the chief. We can easily see that for such a small number of orbits there are no particular differences compared to the ideal scenario (see Figures 3.3 and 3.4 for comparison) or to the results obtained using the HCW equations. The previously described effects become

noticeable in longer duration simulations, where it becomes necessary to act on the formation with appropriate maneuvers. Such low-pulse maneuvers will then need to be periodically applied to avoid this non-uniform trend in inter-satellite distances, and at the same time counteract the secular motion typical of these spacecraft. In the next section a possible method designed to address this need is presented in detail.

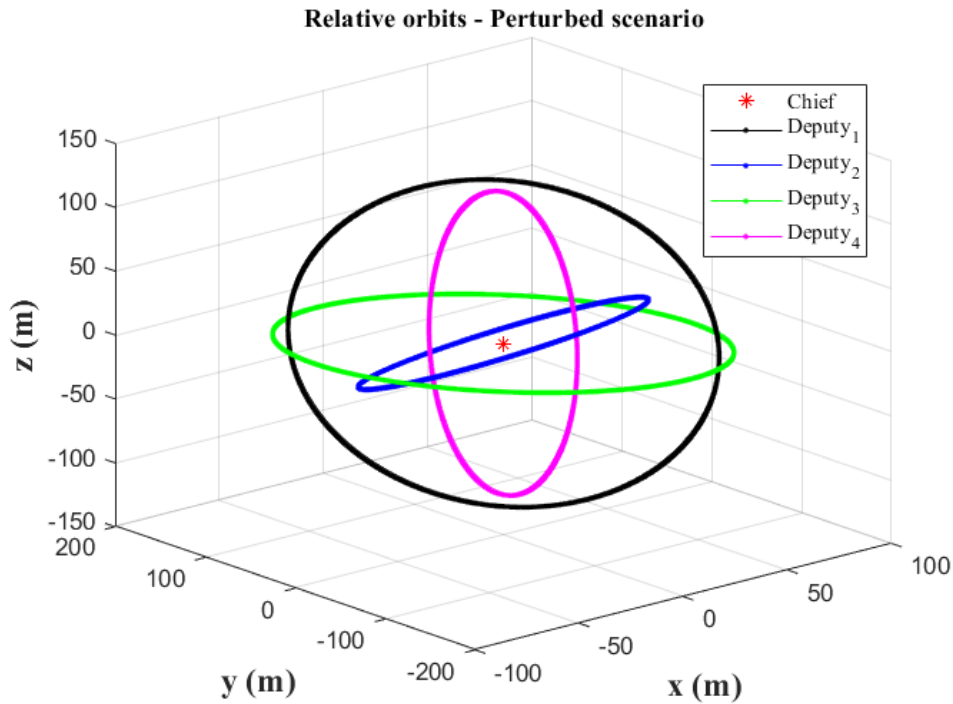


Figure 3.13: Relative orbits for the perturbed scenario.

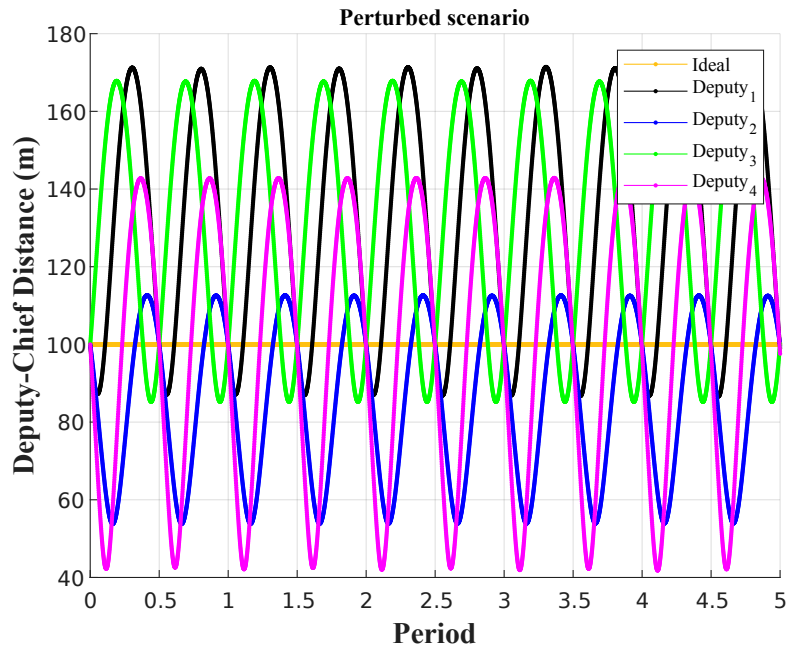


Figure 3.14: Distance between deputies and chief for the perturbed scenario.

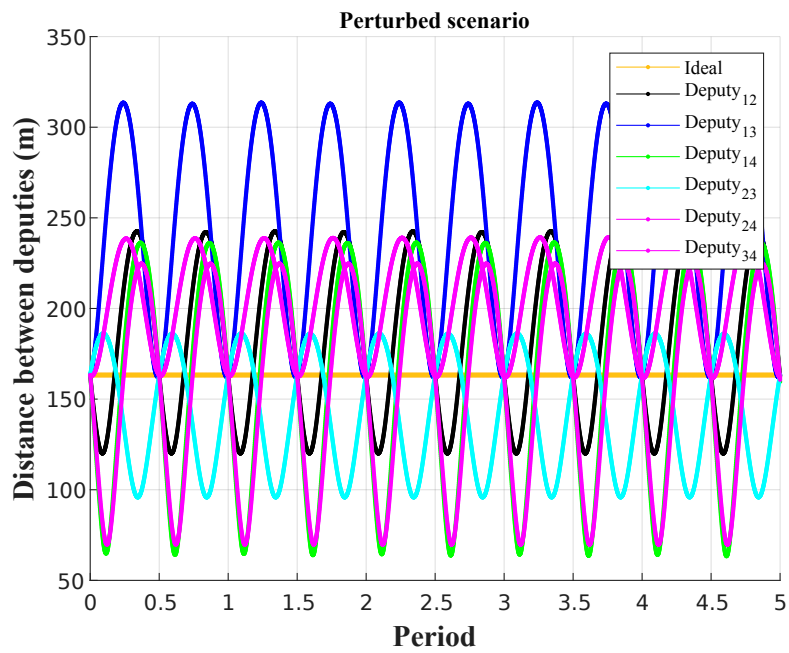


Figure 3.15: Distance between deputies for the perturbed scenario.

3.5 Formation control

The simulations presented in the previous paragraphs showed how the natural dynamics of the spacecraft does not allow the maintenance of the deputies in the desired positions, i.e. at the vertices of the ideal tetrahedron. As observed, this behavior is not due to the presence of the perturbations typical of the space environment, but it is inherent in the orbital dynamics of the spacecraft that constitute the formation. It therefore becomes necessary to perform corrective maneuvers to keep the satellites in the targeted positions.

Given the small size of the spacecraft involved, a possible solution is represented by impulsive burns performed with a propulsion system based on cold gas. This technique is widely tested on small satellites and guarantees good reliability and low costs [19] [20]. However, it is important to define a precise technique to perform such maneuvers effectively, considering one of the fundamental drivers for a mission with these requirements, which is propellant consumption (i.e. the total mass required). In this regard, an algorithm has been conceived whose objective is to find, for each application, the initial conditions of each deputy that guarantee the smallest deviation between the real and the desired distances. Thus, in order to be able to maintain this formation, we need to define an objective function to be minimized for an optimal choice of deputy initial conditions (relative position and velocity of deputies with respect to the chief) subject to some constraints. It is important to say that this methodology, applied to the tetrahedron formation, actually holds for any formation. The general procedure is shown schematically in Algorithm 1. Its implementation in Matlab for the tetrahedral formation consists of a script that can be found in the Appendix B.6.

The objective function L_1 and L_2 are the algebraic sum of the square of residuals of the distance between deputies and chief (d_{ic} , $i = 1, 2, 3, 4$) and distance between deputies (d_{ij} , $i = 1, 2, 3, 4$ and $j = 1, 2, 3, 4$). The constraint is Energy Matching Condition that guarantee 1:1 boundedness between chief and deputies (e.g., it will enforce deputies to have the same period as chief spacecraft so the formation remains bounded and does not

drift). To start the process, we need to have some initial conditions (relative position and velocity of deputies with respect to chief spacecraft). The frame used in this analysis is the \mathcal{L} -frame attached to rotating chief spacecraft. The guessed relative position coordinates of deputies are simply obtained from the geometry of the formation (triangle or tetrahedron) and the guessed relative velocity components can be set to zero with a small value of perturbation to start the integration process of the equations of motions.

3.5.1 The objective function

As can be seen from the review of the algorithm, the focus of this method is on minimizing the proposed cost function. The choice of this function is dictated by a tradeoff between the various distances involved. In order to ensure the tightness of the formation, it is necessary that both the deputy-chief distance and the distance between deputies are aligned as closely as possible with the ideal ones. This ensures that the deputies are arranged to form a regular tetrahedron. However, one must keep in mind the principle that the best formation is the one that most effectively accomplishes the tasks imposed by the mission. As a result, it is possible that mission requirements may not explicitly demand a high degree of accuracy. For an on-orbit servicing mission, the choice of the separation length is driven by the type of servicing to be performed on the chief satellite [16]. In the case of a pre-reentry inspection, a hundred meters may be a good compromise between the proximity for the acquisition of images and the margin to avoid the risk of possible collisions. A distance that remains approximately constant ensures consistency between images acquired by different satellites and faster visual coverage of the target. A similar approach could be taken in the case of possible docking to the satellite chief for maintenance or refueling operations. In this situation the distances involved would be much smaller since the impulsive burns are assumed to anticipate a docking maneuver. In any case, in this kind of scenario it may not be necessary for the distance between individual deputies to remain constant. The cost function could then be adjusted to more effectively meet the required tasks.

As an example, Figure 3.21 shows the plot of the deputy-chief distance obtained by imposing on it an importance 10 times greater than the one of the inter-deputy distance in the cost function. Following the reading of the next paragraphs, the reader will notice how the performance has definitely improved (oscillations in the range of ± 5 m) at the expense of the "regularity" of the tetrahedron, which has become less important. It is therefore crucial the clear definition of the mission objective that imposes the requirements to maintain the formation.

Algorithm 1 Best IC algorithm. d_{ic} is the distance between Deputy i and Chief. d_{ij} is the distance between Deputy i and Deputy j

```

1: procedure BEST IC( $\mathbf{x}$ )
2:   while ( $L_1 + L_2$ ) is minimized and Energy Matching Condition satisfied
   do
3:      $\triangleright$  The algorithm guesses what the best IC could be
4:     Initial Conditions (guessed)
5:      $\triangleright$  The EOM are used to simulate one-orbit trajectory for each
       deputy independently, using the guessed IC
6:     Deputy 1 EOM
7:     Deputy 2 EOM
8:     Deputy 3 EOM
9:     Deputy 4 EOM
10:     $\triangleright$   $L_1$  and  $L_2$  parameters are calculated
11:     $\triangleright$   $d_0$  is the ideal deputy-chief distance
12:     $\triangleright$   $l_0$  is the ideal distance between deputies
13:     $L_1 = \frac{1}{2}(d_{1c} - d_0)^2 + \frac{1}{2}(d_{2c} - d_0)^2 + \frac{1}{2}(d_{3c} - d_0)^2 + \frac{1}{2}(d_{4c} - d_0)^2$ 
14:     $L_2 = \frac{1}{2}(d_{12} - l_0)^2 + \frac{1}{2}(d_{13} - l_0)^2 + \frac{1}{2}(d_{14} - l_0)^2 + \frac{1}{2}(d_{23} - l_0)^2 +$ 
        $\frac{1}{2}(d_{24} - l_0)^2 + \frac{1}{2}(d_{34} - l_0)^2$ 
15:   end while
16:   Optimal IC found
17:   Best IC correspond to the new  $\mathbf{x}$  for each deputy
18: end procedure

```

3.5.2 Triangular formation

In order to test the effectiveness of the algorithm, we initially considered a planar formation consisting of three satellites arranged at the vertices of an equilateral triangle, at the center of which the chief satellite is positioned. As in the main formation under study, the altitude of the orbit of the chief is 350 km and the ideal distance between it and the deputies is 100 m. The ideal distance between the deputies is therefore 173.2 m. The algorithm searches for the initial conditions that guarantee the smallest deviation of the ideal distance from the chief and inter-deputies, finding the best compromise between the two. Figures 3.16 and 3.17 show the output of the algorithm for a simulation period equal to two orbits. Consequently, the maneuvers are applied twice, at the beginning of each orbit. This also explains the sharp point between the first and second orbits, particularly visible for deputy 3 in Figure 3.16 (green curve). Analyzing the plots, we can see the effect of applying the algorithm, as the distances from the chief undergo a deviation of ± 6 m ($\approx 6\%$), while the distances between deputies remain within ± 8 m ($\approx 5\%$). These rather limited values depend strongly on the planar geometry of the formation. In the following section we will notice how a three-dimensional geometry causes greater difficulty in the station-keeping of spacecraft.

Another important aspect to consider is the drift that spacecraft undergo for each orbit (Figure 3.18). Although applying a maneuver for each orbit, the tendency of the deputies is to drift away from the chief, so that even in this case the motion is not completely constrained. Twenty orbits of this formation is about 1.3 days, and if the inspection can be performed in that period of time, the deputies are still not too far drifted from the chief and still are able to do the job to a decent level using just a couple of grams of cold gas. In any case, for more precise formation maintenance, it is necessary to use a technique that overcomes these limitations, e.g. LQR (see next chapter).

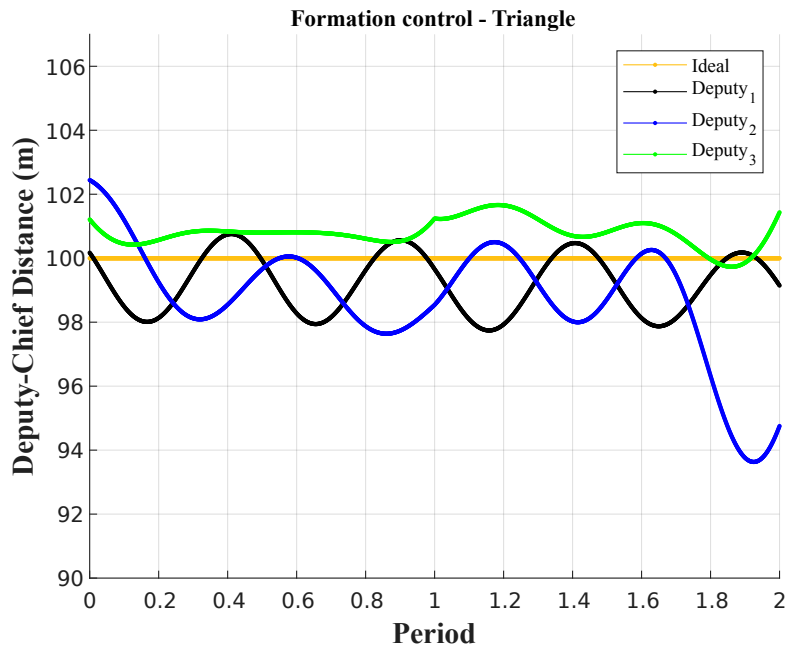


Figure 3.16: Triangular formation maintenance - Deputy-Chief distance.

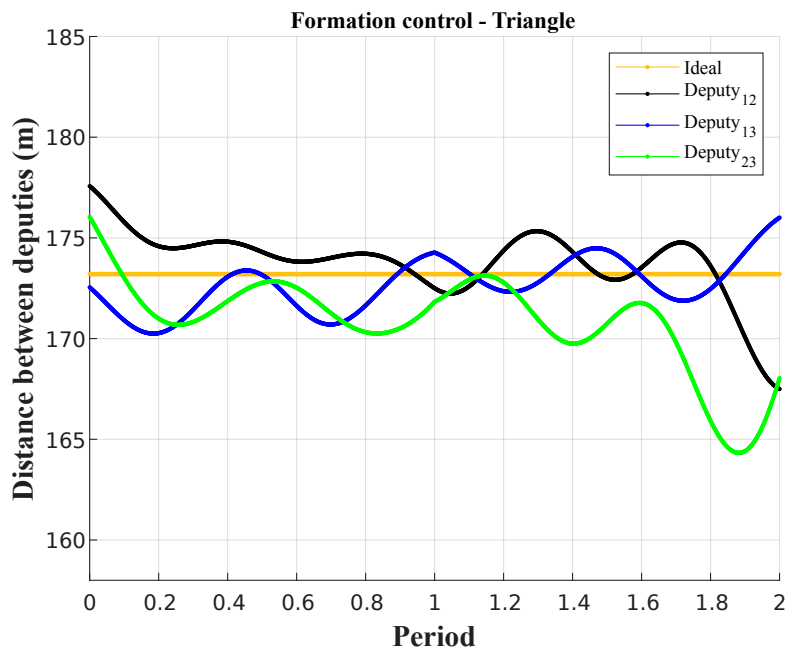


Figure 3.17: Triangular formation maintenance - Distance between deputies.

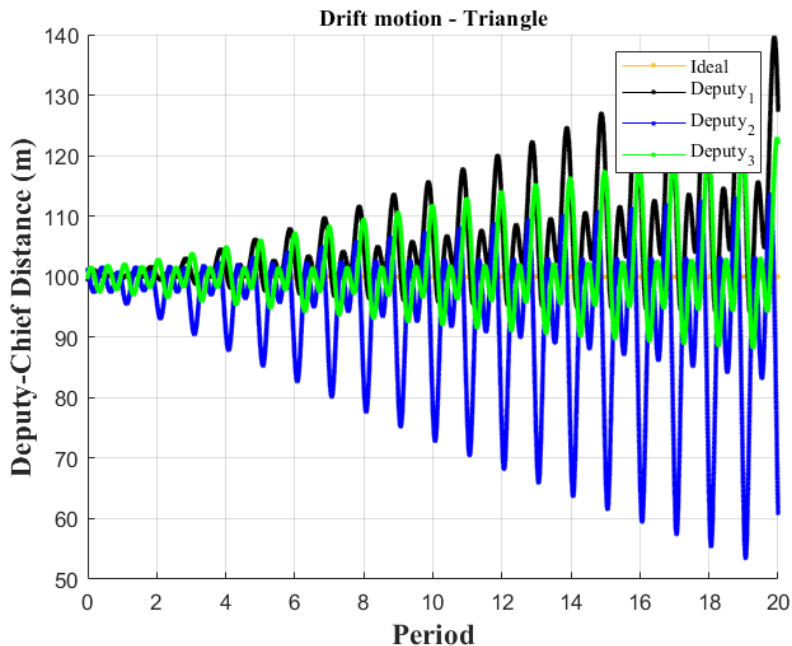


Figure 3.18: Secular motion of the triangular formation. One burn per orbit is applied.

3.5.3 Tetrahedral formation

Similarly to the previous case, the studied algorithm was also applied in the baseline scenario of the tetrahedral formation. Also in this case, the ideal distance is 100 m (corresponding to 163.3 m between deputies). The application of the propulsive burns occurs once per orbit. The results of these simulations can be found in Figures 3.19 and 3.20. As can be clearly observed, the maintenance of the formation is not as precise as in the triangular case. The oscillation of the distances from the chief is between about 60 and 130 m ($\approx \pm 30\%$) while the edges of the tetrahedron vary in length between 210 and 75 m ($\approx \pm 50\%$ in the worst case). If we compare these values with those in Figures 3.14 and 3.15 we notice a significant improvement in the maintenance of the formation, although the oscillations still remain considerable. Compared to the planar case, a three-dimensional formation indeed needs more burns and still has a large room for improvement. A

solution is provided by increasing the number of maneuvers per orbit. A possible scenario involves the application of 4 burns per orbit (one per quarter of an orbit), but at a much higher propulsive cost. It is a matter of trade-off between formation maintenance tolerance and fuel consumption. The values of ΔV required for formation maintenance are reported in the next chapter, together with other secondary analyses. In this regard, the choice of the most efficient propulsion system is crucial. A propulsion system such as cold gas has many advantages but also an inherent limitation on the value of the specific impulse I_{sp} . Exploiting hydrogen as cold gas, a reasonable value of I_{sp} is around 272 s, which can be largely exceeded if the choice of the propulsion system is based on another type of technology (e.g. electric propulsion), more suitable for the specific purposes. Once again, as in the case of the triangular formation, a more advanced control method such as LQR can be an effective solution and thus result in significantly reduced costs.

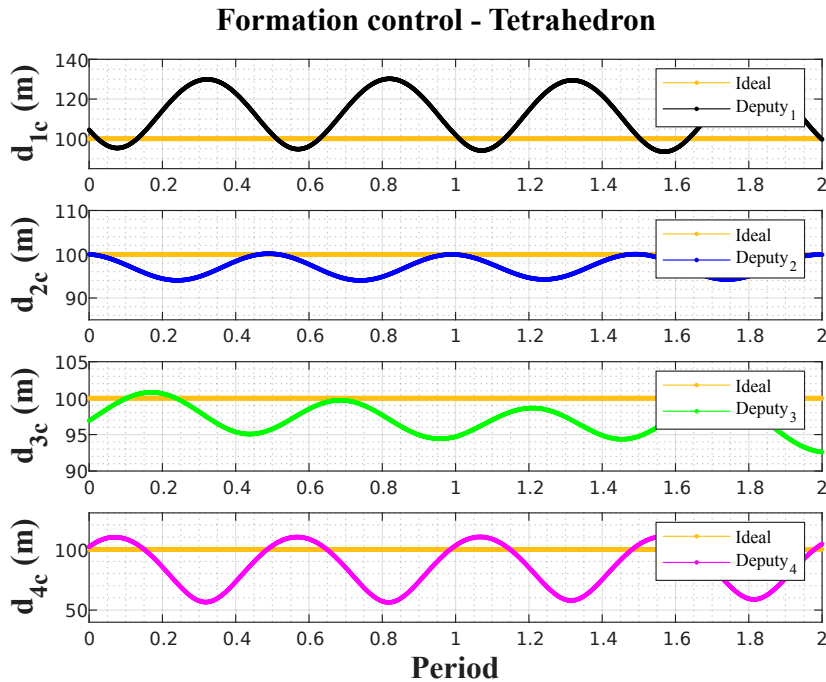


Figure 3.19: Tetrahedral formation maintenance - Deputy-Chief distance.

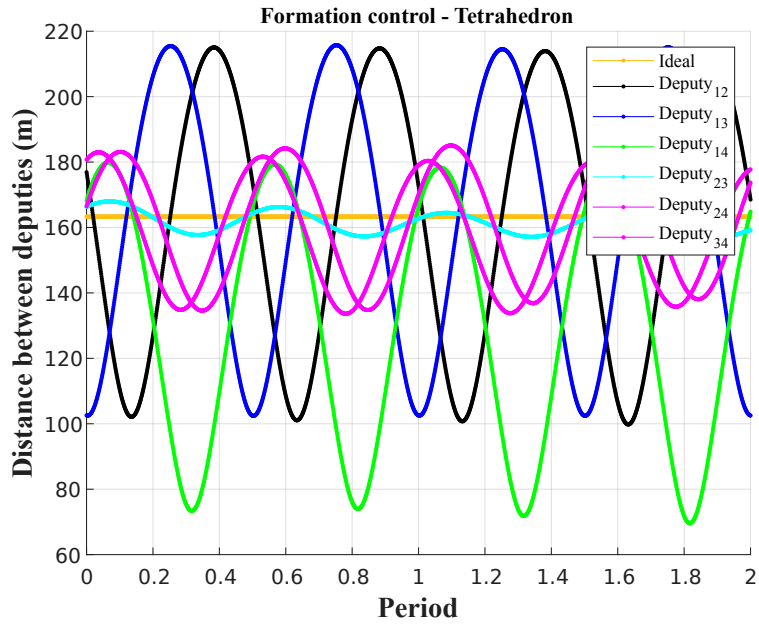


Figure 3.20: Tetrahedral formation maintenance - Distance between deputies.

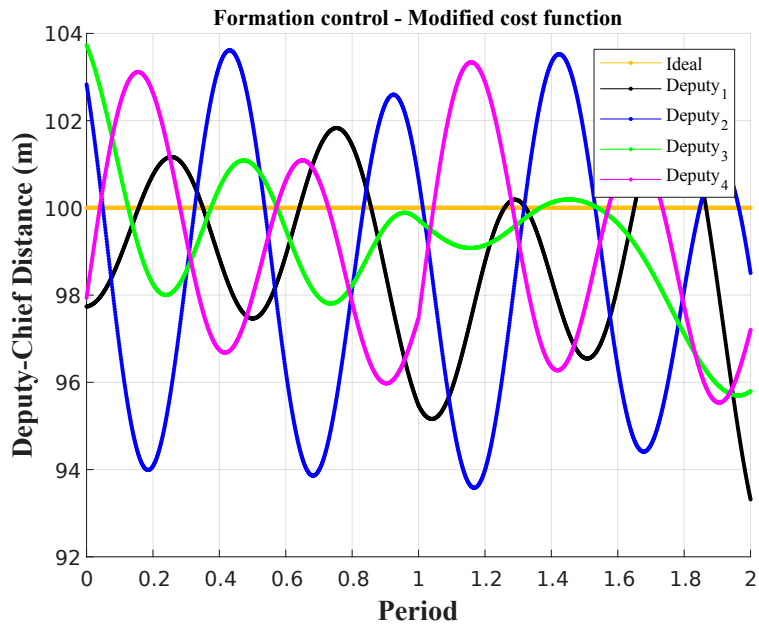


Figure 3.21: Effect of the adjustment of the cost function. Deputy-Chief distance has been given a 10-times more importance than the inter-deputy distance.

Chapter 4

Sensitivity Analysis

In the previous chapter, an algorithm was proposed that defines a possible strategy for the application of impulsive maneuvers, which are necessary for the maintenance of the formation. In this chapter we want to present the results of some secondary analyses that were conducted. Initially, we wanted to observe the effects of a change in the size of the formation, then we focused on the consequences of choosing a different altitude for the insertion orbit. The last part of the work was the application of the studied algorithm in an environment other than Low Earth Orbit. In anticipation of an asteroid-directed science mission, we analyzed the formation behavior using an asteroid of the main belt as the primary body, *Vesta*.

4.1 Change in the formation size

The first case we considered was a change in the formation size. In the baseline scenario, the ideal distance between the four deputies and the chief satellite is 100 m. Due to geometric issues the distance between two deputies is 163.3 m ($L = \frac{2\sqrt{6}}{3} \cdot R$, where L is the length of the edge of the tetrahedron and R is the radius of the sphere circumscribed to the tetrahedron).

The Table 4.1 reports the ΔV required to maintain formation for six different sizes, applying the strategy provided by the algorithm presented in the section 3.5. The altitude is kept constant at 350 km ($\rho = 1.8796 \cdot 10^{-11} \cdot 10^9$

kg/km³). However, it is important to spend a couple of words on how these values were obtained. As explained above, the objective of the algorithm is the search for the best initial conditions, able to minimize the objective function and keeping the Energy Matching Condition as a constraint. The solution provided by the algorithm is therefore a state vector with the components of position and velocity for each deputy (six for each, 24 values in total). Depending on the frequency of application of the maneuvers, this vector is updated more or less frequently. In the case study presented, we therefore obtain a single set of values for each orbit of the chief. Once the converged solution is obtained, the following equation is used to calculate the ΔV of the maneuver:

$$\Delta V = \sqrt{(v_x - v_{x0})^2 + (v_y - v_{y0})^2 + (v_z - v_{z0})^2} \quad (4.1)$$

where v_x , v_y , and v_z are the solutions, and v_{x0} , v_{y0} , and v_{z0} are the guessed deputies relative velocity components. These latter components correspond to the initial estimate with which the algorithm is first initialized or to the spacecraft's conditions at the end of the previous orbit, in the case of orbits after the first one. Accurate computation of the ΔV required by a mission therefore requires analysis of each orbit made by the formation. In fact, simulations conducted for our case study have shown that the values of ΔV for the first orbit are significantly larger than those required by subsequent orbits, which are held constant in the first approximation. Consequently, an effective way to calculate the ΔV for a mission is to consider the value of ΔV at the beginning of the first orbit to which one adds the ΔV of the second multiplied by the number of orbits of the mission. This technique is of course applied to each deputy individually, so the ΔV_{tot} of the formation is the sum of the contributions required by each deputy.

$$\Delta V_{tot} = \Delta V_1 + n^\circ \text{ orbits} \cdot \Delta V_2 \quad (4.2)$$

where ΔV_1 is the ΔV that the maneuver requires at the beginning of the first orbit, while ΔV_2 is the ΔV before the second one and its value is considered constant also for the following ones.

As can be seen from Table 4.1, increasing the size of the formation causes a significantly higher cost in terms of ΔV , with a progression that is not exactly linear. The increase in ΔV going from 50 m to 500 m is indeed more than ten times higher. This is not an entirely unexpected result. A larger formation implies that the satellites travel a greater distance per orbit and thus experience greater deviation. The consequence is that maintaining such a formation requires more propulsive effort. In any case, for a mission of 100 orbits (about 6 days of operations), the highest expected single deputy ΔV is 2.95 m/s. Starting from this result, exploiting the Tsiolkovsky rocket equation and considering hydrogen as a cold gas, it is easy to derive that the mass of H_2 to be embarked on the satellite is about 0.0033 kg (3.3 grams), a value that seems reasonable considering the wet mass of such satellites (3 kg).

Size (d_0) [m]	ΔV [m/s] Deputy 1	ΔV [m/s] Deputy 2	ΔV [m/s] Deputy 3	ΔV [m/s] Deputy 4	ΔV [m/s] TOT
50	0.20	0.09	0.13	0.17	0.59
100	0.46	0.14	0.24	0.41	1.25
200	0.80	0.37	0.49	0.69	2.35
300	1.24	0.85	0.56	1.58	4.24
400	1.63	0.95	0.81	1.68	5.09
500	2.13	1.49	0.90	2.95	7.47

Table 4.1: Sensitivity analysis for formation size at the same altitude (350 km) (with atmospheric drag) - ΔV for 100 orbits

4.2 Effects of formation’s altitude

The second analysis focused on the role of the altitude of the formation. The radius of the chief’s orbit, which can be approximated to that of the other four satellites, is closely related to the effects of the presence of the J_2 parameter and those of atmospheric drag. For this reason, two separate analyses were carried out, the first excluding the contribution of the atmosphere (thus taking into account only J_2), the second including the latter

as well. Atmospheric density values at high altitudes were obtained from a database made available by JPL. Again, the outputs of the simulations were the ΔV obtained for each deputy individually. Tables 4.2 and 4.3 summarize the results of the study. The aspect that stands out is the absence of a clear unambiguous trend as altitude increases or decreases. In the scenario where atmospheric resistance is not considered, it is interesting to note that the presence of J_2 alone does not provide a sufficient contribution to significantly change the values of ΔV . This can be explained because the increase in altitude must be seen in relation to the radius of the orbit. Raising from 250 km to 500 km, the orbit radius undergoes an increase of 3.8% and consequently, while still in LEO, the effect of J_2 does not change appreciably.

Altitude [km]	ΔV [m/s] Deputy 1	ΔV [m/s] Deputy 2	ΔV [m/s] Deputy 3	ΔV [m/s] Deputy 4	ΔV [m/s] TOT
250	0.42	0.20	0.25	0.37	1.23
300	0.43	0.31	0.18	0.60	1.53
350	0.49	0.40	0.33	0.42	1.64
400	0.66	0.19	0.25	0.42	1.52
450	0.38	0.39	0.32	0.39	1.48
500	0.37	0.17	0.24	0.32	1.10

Table 4.2: Sensitivity analysis for formation altitude with the same size (100 m) (without atmospheric drag) - ΔV for 100 orbits

Altitude [km]	ΔV [m/s] Deputy 1	ΔV [m/s] Deputy 2	ΔV [m/s] Deputy 3	ΔV [m/s] Deputy 4	ΔV [m/s] TOT
250	0.42	0.26	0.20	0.47	1.36
300	0.41	0.30	0.19	0.57	1.47
350	0.46	0.14	0.24	0.41	1.25
400	0.21	0.32	0.31	0.32	1.15
450	0.42	0.40	0.32	0.40	1.53
500	0.39	0.20	0.21	0.36	1.15

Table 4.3: Sensitivity analysis for formation altitude with the same size (100 m) (with atmospheric drag) - ΔV for 100 orbits

Regarding the second scenario (Table 4.3), we can conclude that there is a trend in which lower altitudes cause an increase in ΔV due to the higher resistance, but this does not immediately emerge. In addition, complicating the analysis is the presence of an outsider value for the altitude of 450 km. Among the possible causes, one can speculate that in this situation the value of ΔV calculated for the second orbit is not representative of the subsequent ones (see Eq. (4.2)). In any case, a further study could focus on the performance obtained by the formation in relation to altitude, since an increase in the propulsive cost is not necessarily related to an improvement in the tightness of the formation.

4.3 Application on Vesta

Vesta is a large asteroid of the Main Belt, the second most massive body in the asteroid belt, with an average diameter of about 525 kilometers and an estimated mass of about one-tenth that of the entire belt. It was discovered by the German astronomer Heinrich Wilhelm Matthias Olbers on March 29, 1807 and is named after Vesta, the virgin goddess of home and hearth from Roman mythology. Its size and unusually bright surface make Vesta the brightest and sometimes the only asteroid visible to the naked eye from Earth.

The main physical characteristics of Vesta are shown in Table 4.4, while its orbit parameters are reported in Table 4.5.

Parameter	Value
Major axes	286.3/278.6/223.2 km
Mean radius	262.7 km
Mass	2.59076×10^{20} kg
Volume	70.970×10^6 km ³
μ	17.28037 km ³ s ⁻²
J_2	0.0317799
k_{J_2}	56848.2327 km ⁵ s ⁻²

Table 4.4: Asteroid Vesta’s main characteristics. Source: [21].

Parameter	Value
Epoch	2020-Dec-17
Semi-major axis a	2.36203 AU
Eccentricity e	0.088425
Inclination i	7.14165°
Longitude of the ascending node	103.8083°
Argument of perihelion	150.9224°
Mean anomaly	258.5678°

Table 4.5: Asteroid Vesta’s orbital characteristics. Source: [22].

Vesta has assumed a particular importance because it was one of the targets of NASA’s *Dawn* mission [23]. The launch of the probe took place on September 27, 2007, and after four years of travel it entered orbit around Vesta on July 16, 2011, where it completed 14 months of observations. It subsequently entered orbit around Ceres on March 6, 2015. In 2017, an extension of the mission was announced, which ended on November 1, 2018, when the probe ran out of propellant. Currently, the probe, deactivated, is in a stable orbit around Ceres [24].

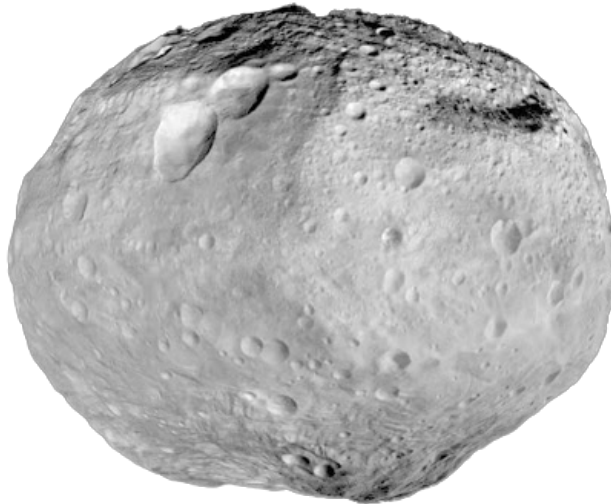


Figure 4.1: Representation of asteroid Vesta.

After analyzing the behavior of the tetrahedral formation in LEO, the focus shifted to a possible interplanetary mission. The purpose of this last part of the work was indeed the analysis of the dynamics of the formation in orbit around a celestial body such as Vesta, of which we have a lot of data thanks to the Dawn mission. The choice of such a celestial body was made in perspective of a possible on-orbit servicing mission, which sees a satellite chief in orbit around a celestial body like Vesta and a formation that can provide maintenance or refueling at the end of its operational life. For the sake of simplicity, the hypothesis of patched conic approximation was assumed and thus the effect of a third celestial body like the Sun was not considered. The major differences found when looking at the data for the Earth and those for Vesta concern the mass of the two bodies and the parameter J_2 . One of the characteristics of Vesta is in effect the great widening of its shape at the equator, characteristic that affects the parameter J_2 because the gravitational field generated by this body cannot be considered uniform. Table 4.6 shows the data related to ΔV for a period equal to 100 orbits, as a function of the altitude around Vesta. Looking at the data for the total ΔV , it is easy to see that as the altitude increases, the cost required to maintain the formation decreases drastically. This happens because at higher altitudes the satellites suffer less from the drift caused by J_2 . The lack of uniformity in the gravitational field generated by Vesta is less perceivable and the mass of the celestial body is assimilated more and more to a material point. We can therefore say that for higher altitudes the drift due to J_2 is less pronounced and this results in a lower propulsive cost.

Altitude [km]	ΔV [m/s] Deputy 1	ΔV [m/s] Deputy 2	ΔV [m/s] Deputy 3	ΔV [m/s] Deputy 4	ΔV [m/s] TOT
200	1.10	0.73	1.08	1.06	3.97
300	0.64	0.42	0.56	0.53	2.15
500	0.27	0.15	0.20	0.22	0.85
750	0.14	5.01e-2	8.30e-2	9.81e-2	0.37
1000	4.91e-2	1.35e-2	3.13e-2	3.63e-2	0.13
5000	8.6e-4	1.10e-3	8.21e-5	1.25e-3	3.25e-3

Table 4.6: Sensitivity analysis for Vesta (effect of J_2 parameter) - ΔV for 100 orbits

Chapter 5

Conclusions

The main topic of this dissertation was spacecraft formation flying. This technology, which was born at the end of the last century, has become particularly interesting for space agencies in the last two decades. Indeed, several studies have shown that in various situations many of the tasks typically performed by single space platforms can be accomplished with formations consisting of multiple smaller, more cost-effective satellites. Among the various types of missions in which such formations can be employed, on-orbit servicing missions have taken on a special importance in recent years, driven by the continuous growth of the commercial space sector. The possible solutions offered by this approach include the refueling of larger satellites at the end of their operational life, the repair of spacecraft in orbit or the inspection of cargo spacecraft in the re-entry phase to Earth. Of course, this does not exclude scientific missions, where two or more satellites can be deployed separately to achieve a common goal (e.g. occultation of the Sun for the observation of the solar corona in the Proba-3 mission).

In the framework of this study, the attention was focused on the investigation of the behavior of a tetrahedral formation (plus a chief satellite located in its center) operating in LEO orbit and subject to the perturbations typical of the space environment. Small-satellites have now become a well-established technology and seemed suitable to constitute such a formation. In the first phase of the work, simulations conducted showed that the natural dynamics

of spacecraft do not allow them to maintain their initial positions. The relative orbits described by the deputies around the chief undergo periodic variations in their radius, resulting in an oscillation in the distance between the deputies and the chief or between individual deputies. Along with this tendency comes a drifting motion that moves the deputies away from the chief. Nevertheless, this last characteristic is not completely unexpected. Such motion is in fact the result of the instability of the system of equations that describes the dynamics of relative motion. Thus, the need to have an effective strategy for spacecraft control has emerged.

The next step undertaken was the development of an algorithm that would define the criterion for the application of the impulsive burns. The method that has been proposed seeks to find the best initial conditions that minimize an appropriate cost function. This cost function considers the residual between the real distances obtained through simulations and the ideal distances. In the course of this study no adjustments to this objective function have been contemplated, but a possible improvement of the algorithm envisages the introduction of specific coefficients capable of handling the relative importance of the distances involved. In other words, depending on the type of mission, it could be useful to attribute more importance to the distance of a particular deputy from the chief, or to the distance from the chief with respect to the distance between the deputies themselves.

The proposed algorithm was applied to the case of a triangular planar formation and then to the baseline scenario with the tetrahedral formation. The achieved performance showed that the triangular formation responds much better to the maneuvers imposed by the algorithm if compared to the tetrahedral formation. As a matter of fact, a three-dimensional formation is much more prone to drifting away from its initial conditions. In any case, the mission requirements define the precision with which the formation should be maintained. A period of about 6 days seems suitable for tasks such as the inspection of a satellite or its refueling. For longer mission durations while maintaining acceptable performance and cost, more advanced methods of spacecraft control must be implemented. The last phase of this research

was a sensitivity analysis to observe the effect of atmospheric drag and the formation size. What emerged is a strong dependence on size since the deflection that the deputies undergo is closely related to the distance they have from the chief.

Of course, there is no lack of possible further developments for this research. Regarding the maneuvering optimization method, an already mentioned solution is to consider LQR. The electric propulsion could in fact guarantee a much higher I_{sp} than the one reached with a system based on cold gas. In this case one would not use impulsive burns but a continuous maneuver. The LQR problem from optimal control theory is used to track a given reference trajectory that exactly maintains the desired configuration. The need for linearized equations would be overcome with the implementation of the HCW equations, extensively treated throughout this work.

Another aspect to take into consideration is the implementation of the proposed cost function. As previously mentioned, the current function seems to be a good compromise to account for the overall tightness of the formation, but the requirements of a specific mission may focus on only some aspects of it. By tailoring the cost function to the mission requirements, for example by introducing weight coefficients for the distances involved, the maneuvers performed could be much more focused and ultimately targeted to the true mission objectives. As in any space mission, the best choice is often the one dictated by the best trade off. Therefore, a more in-depth study of this type cannot disregard a comprehensive view of the mission, an awareness that belongs only to the reader of this (hopefully interesting) dissertation.

This page is intentionally left blank

Appendix A

Complementaries on Keplerian problem and relative motion

A.1 Change of coordinates from \mathcal{I} to \mathcal{R}

$$\mathbf{r} = r\hat{\mathbf{r}} \tag{A.1}$$

$$\dot{\mathbf{r}} = \dot{r}\hat{\mathbf{r}} + r\dot{\theta}\hat{\boldsymbol{\theta}} \tag{A.2}$$

$$\ddot{\mathbf{r}} = (\ddot{r} - r\dot{\theta}^2)\hat{\mathbf{r}} + (2\dot{r}\dot{\theta} + r\ddot{\theta})\hat{\boldsymbol{\theta}} \tag{A.3}$$

A.2 Conservation of energy

We can start from Eq. (2.13) and we firstly note that

$$\ddot{r} = \frac{d}{dt} \left(\frac{dr}{dt} \right) = \frac{dr}{dt} \frac{d}{dr} \left(\frac{dr}{dt} \right) = \dot{r} \frac{d}{dr} (\dot{r}) = d \left(\frac{\dot{r}^2}{2} \right) \tag{A.4}$$

Substituting this result into Eq. (2.13) yields

$$d\left(\frac{\dot{r}^2}{2}\right) = \left(\frac{h^2}{r^3} - \frac{\mu}{r^2}\right) \quad (\text{A.5})$$

Integrating both sides of the previous equation we obtain

$$\mathcal{E} = \frac{\dot{r}^2}{2} + \frac{h^2}{2r^2} - \frac{\mu}{r} = \frac{\dot{r}^2}{2} + \frac{(r\dot{\theta})^2}{2} - \frac{\mu}{r} = \text{const.} \quad (\text{A.6})$$

\mathcal{E} is the constant of integration, i.e. the *total energy* per unit mass, which is composed by two terms: the first one is the *kinetic energy* $[\frac{1}{2}(\dot{r} + r\dot{\theta})^2]$, while the latter is the *potential energy* $[-\frac{\mu}{r}]$. Thus, this equation can be also written in the form

$$\mathcal{E} = \frac{v^2}{2} - \frac{\mu}{r} \quad (\text{A.7})$$

where v is the magnitude of the velocity vector.

A.3 Spacecraft relative motion

In order to develop the equations (2.32) we need to remind the reader the relative acceleration in frame \mathcal{L}

$$\ddot{\mathbf{r}}_d = \frac{d^2{}^{\mathcal{L}}\mathbf{r}_d}{dt^2} + 2{}^{\mathcal{J}}\boldsymbol{\omega}^{\mathcal{L}} \times \frac{d{}^{\mathcal{L}}\mathbf{r}_d}{dt} + \frac{d{}^{\mathcal{J}}\boldsymbol{\omega}^{\mathcal{L}}}{dt} \times \mathbf{r}_d + {}^{\mathcal{J}}\boldsymbol{\omega}^{\mathcal{L}} \times ({}^{\mathcal{J}}\boldsymbol{\omega}^{\mathcal{L}} \times \mathbf{r}_d) \quad (\text{A.8})$$

where ${}^{\mathcal{J}}\boldsymbol{\omega}^{\mathcal{L}}$ denotes the angular velocity vector of frame \mathcal{L} relative to frame \mathcal{J} . With no perturbations, we can write

$${}^{\mathcal{J}}\boldsymbol{\omega}^{\mathcal{L}} = [0, 0, \dot{\theta}_0]^T \quad (\text{A.9})$$

The position vector in the \mathcal{J} -frame can be written as

$$\mathbf{r}_0 = [r_0, 0, 0]^T \quad (\text{A.10})$$

and the position of the deputy in the LVLH frame is

$$[\mathbf{r}_d]_{\mathcal{L}} = [x, y, z]^T \quad (\text{A.11})$$

Substituting Eqs. (2.31), (A.9) and A.11 into Eq. (A.8) and writing the scalar equations for each component, we obtain the system (2.32).

This page is intentionally left blank

Appendix B

Matlab scripts

This section reports the main Matlab scripts employed for the simulations. The interested reader is encouraged to consult them if he wishes to learn more about the methods used for the analyses.

Listing B.1: Initial conditions for tetrahedron

```
1 format long g
2
3 % clear all
4
5 GM=398600.435436096;
6 kJ2=2.633e10;
7 r=6728.1363;
8 vx=0;
9 h=51786.4659815034;
10 OMEGA=0;
11 i=0.9;
12 theta=0.785398163397448;
13
14 tetra_rot
15
16 for j=1:4
17
18 x0=dep_all(1,j);
19 y0=dep_all(2,j);
20 z0=dep_all(3,j);
```

```

21 %
22 DU_J2(1)=GM/r^2 + (kJ2/r^4)*(1-3*sin(i)^2*sin(theta)^2);
23 DU_J2(2)=(kJ2/r^4)*sin(i)^2*sin(2*theta);
24 DU_J2(3)=(kJ2/r^4)*sin(2*i)^2*sin(theta);
25
26 a=atan2(DU_J2(2),DU_J2(1));
27 b=atan2(DU_J2(3),sqrt(DU_J2(1)^2 + DU_J2(2)^2));
28
29 wz_pp=sqrt(norm(DU_J2)/r);
30
31 C(1,1)=(3/2)*cos(a)*sin(a)*cos(b)-cos(a)^2*sin(a)^2*tan(theta);
32 C(1,2)=(1/2)*cos(a)^2*cos(b)+2*sin(a)^2*cos(b)-cos(a)*sin(a)*sin
    (b)^2*tan(theta);
33 C(1,3)=2*sin(a)*sin(b)+cos(a)*cos(b)*sin(b)*tan(theta);
34 C(2,1)=-2*cos(a)^2*cos(b)-(1/2)*sin(a)^2*cos(b)-cos(a)*sin(a)*
    sin(a)^2*tan(theta);
35 C(2,2)=-3/2*cos(a)*sin(a)*cos(b)-sin(a)^2*sin(b)^2*tan(theta);
36 C(2,3)=-2*cos(a)*sin(b)+sin(a)*cos(b)*sin(b)*tan(theta);
37 C(3,1)=-1/2*sin(a)*sin(b)+cos(a)*cos(b)*sin(b)*tan(theta);
38 C(3,2)=(1/2)*cos(a)*sin(b)+sin(a)*cos(b)*sin(b)*tan(theta);
39 C(3,3)=-cos(b)^2*tan(theta);
40
41 v0LJ2=wz_pp*C*[x0;y0;z0];
42
43 vx0LJ2=v0LJ2(1);
44 vy0LJ2=v0LJ2(2);
45 vz0LJ2=v0LJ2(3);
46
47 v0LJ2;
48
49 % The following part calculates v0_NJ2
50 rj=sqrt((r+x0)^2 + y0^2 + z0^2);
51 rZ=(r+x0)*sin(i)*sin(theta) + y0*sin(i)*cos(theta) + z0*cos(i);
52
53 U = -GM/r - (kJ2/r^3)*(1/3-sin(i)^2*sin(theta)^2);
54 Uj= -GM/rj - (kJ2/rj^3)*(1/3-rZ^2/rj^2);
55
56 V(1)=vx;
57 V(2)=h/r;

```

```

58
59 V_n=norm(V);
60
61 VrJ2=sqrt(V_n^2 + 2*(U-Uj));
62
63 wx=-kJ2*sin(2*i)*sin(theta)/(h*r^3);
64 wz=h/r^2;
65
66 VLJ2_(1)= vx + vx0LJ2 - y0*wz;
67 VLJ2_(2)= h/r + vy0LJ2 + x0*wz - z0*wx;
68 VLJ2_(3)= vz0LJ2 + y0*wx;
69
70 VLJ2=norm(VLJ2_);
71
72 VrL=VrJ2/VLJ2;
73
74 vx0NJ2 = VrL*vx0LJ2 + (VrL-1)*(vx-y0*wz);
75 vy0NJ2 = VrL*vy0LJ2 + (VrL-1)*(h/r + x0*wz - z0*wx);
76 vz0NJ2 = VrL*vz0LJ2 + (VrL-1)*y0*wx;
77
78 v0NJ2=[vx0NJ2;vy0NJ2;vz0NJ2];
79
80 v0NJ2;
81
82 (v0NJ2-v0LJ2)*1e6;
83
84 deputy_IC_LJ2=[x0;y0;z0;v0LJ2];
85 IC_NJ2=[x0;y0;z0;v0NJ2];
86
87 deputy_IC_NJ2_all_v2(1,j)=IC_NJ2(1);
88 deputy_IC_NJ2_all_v2(2,j)=IC_NJ2(2);
89 deputy_IC_NJ2_all_v2(3,j)=IC_NJ2(3);
90 deputy_IC_NJ2_all_v2(4,j)=IC_NJ2(4);
91 deputy_IC_NJ2_all_v2(5,j)=IC_NJ2(5);
92 deputy_IC_NJ2_all_v2(6,j)=IC_NJ2(6);
93
94 clear IC_NJ2
95
96 end

```

```
97
98 IC_TETRA=deputy_IC_NJ2_all_v2
```

Listing B.2: Tetrahedron rotation

```
1 format long g
2
3 d0 = 0.1;
4 ratio=1.0;
5
6 dep_x=ratio*
7 [0.1; -0.03333333339347834;...
8 -0.03333333339347834; -0.03333333339347834];
9 dep_y=ratio*...
10 [0;0;0.0816496579086169; -0.0816496579086169];
11 dep_z=ratio*...
12 [0;0.0942809039455616; -0.0471404519727808; -0.0471404519727808];
13
14 phi = 40; phi = phi*(pi/180);
15 psi = 60; psi = psi*(pi/180);
16
17 R3 = [cos(phi) -sin(phi) 0; sin(phi) cos(phi) 0; 0 0 1];
18 R1 = [1 0 0; 0 cos(psi) -sin(psi); 0 sin(psi) cos(psi)];
19
20 dep_1 = R1*R3*[dep_x(1); dep_y(1); dep_z(1)];
21 dep_2 = R1*R3*[dep_x(2); dep_y(2); dep_z(2)];
22 dep_3 = R1*R3*[dep_x(3); dep_y(3); dep_z(3)];
23 dep_4 = R1*R3*[dep_x(4); dep_y(4); dep_z(4)];
24
25 dep_all=[dep_1 dep_2 dep_3 dep_4];
```

Listing B.3: Independent trajectories

```
1 function Independent_trajectories
2
3 clear all; close all; clc; format long g;
4
5 global GM
6 GM = 398600.435436096;
7 IC_for_tetrahedron % Initial condition calculator
```

```

8
9 for i=1:4 % Number of deputies
10
11 Deputy_IC(:,i) = IC_TETRA(:,i); % Deputies initial conditions
12
13 % Chief initial conditions -----
14 Re=6378.1363; % Earth radius [Km]
15 Alt=350; % Satellite altitude [Km]
16
17 r_c0=Re+Alt; % Initial semi-major axis [km]
18 r_c0dot=0;
19
20 wz=sqrt(GM/(r_c0^3)); % Mean motion [rad/s]
21 Period=2*pi/wz; % Period [s]
22
23 h0 = r_c0^2*wz; % Initial angular momentum
24 OM0=0; % Initial RAAN [rad]
25 i0 = 0.9; % Initial inclination [rad]
26 theta0 = pi/4; % Initial argument of latitude [rad] (45
    deg)
27 e0=0; % Chief's orbit eccentricity
28 om0=0; % Initial argument of perigee
29
30 [r0_vec , v0_vec]=kep2car(r_c0 , e0 , i0 , OM0, om0 , theta0-om0, GM); %
    Chief IC state vector (ECI)
31
32 % Deputies initial conditions -----
33 DepIC_r_L=[Deputy_IC(1,i); Deputy_IC(2,i); Deputy_IC(3,i)]; %
    Deputy IC (r) in LVLH frame
34 DepIC_v_L=[Deputy_IC(4,i); Deputy_IC(5,i); Deputy_IC(6,i)]; %
    Deputy IC (v) in LVLH frame
35
36 h0_vec=cross(r0_vec , v0_vec);
37 h0_vec_u=h0_vec/norm(h0_vec);
38 r0_vec_u=r0_vec/norm(r0_vec);
39 TM=[r0_vec/norm(r0_vec) , cross(h0_vec_u , r0_vec_u) , h0_vec_u]; %
    Rotation Matrix LVLH to ECI
40

```

```

41 DepIC_r=TM*[r_c0+Deputy_IC(1,i);Deputy_IC(2,i); Deputy_IC(3,i)];
    %Deputy IC (r) in ECI frame
42
43 DepIC_v=TM*[Deputy_IC(4,i)-wz*Deputy_IC(2,i)+r_c0dot; Deputy_IC
    (5,i)+wz*(Deputy_IC(1,i)+r_c0);Deputy_IC(6,i)];
44
45 % Simulation parameters _____
46 num_orb = 5;           % Number of orbits for the simulation
47 tf=num_orb*Period;    % Final time
48 dt=Period/1000;      % Time step
49 tspan=0:dt:tf;       % Time vector
50 % _____
51
52 qd0=[DepIC_r(1);DepIC_r(2);DepIC_r(3);DepIC_v(1);DepIC_v(2);
    DepIC_v(3)];
53
54 options = odeset('RelTol',1e-10,'AbsTol',1e-12);
55 [t, Q(:, :, i)] = ode113(@integrator, tspan, qd0, options);
56
57 end
58
59 qc0=[r0_vec(1);r0_vec(2);r0_vec(3);v0_vec(1);v0_vec(2);v0_vec(3)
    ];
60 options = odeset('RelTol',1e-10,'AbsTol',1e-12);
61 [t, Q(:, :, 5)] = ode113(@integrator, tspan, qc0, options);
62
63 save Independent_traj t Q
64
65 return
66
67 function qdot = integrator(t,q)
68
69 global GM
70
71 r = sqrt(q(1)^2 + q(2)^2 + q(3)^2);
72
73 % Perturbation acceleration
74 m=3; % Spacecraft mass
75 T0=0; % Thrust magnitude (N)

```

```

76
77 vec=[q(4);q(5);q(6)]/norm([q(4);q(5);q(6)]); %Thrust unit vector
78
79 % Perturbation acceleration in term of km/s^2
80 a_x=(T0/m)*vec(1)/1000;
81 a_y=(T0/m)*vec(2)/1000;
82 a_z=(T0/m)*vec(3)/1000;
83
84 % Spacecraft equations of motion
85 qdot(1) = q(4);
86 qdot(2) = q(5);
87 qdot(3) = q(6);
88
89 qdot(4)=-GM*q(1)/r^3 + a_x;
90 qdot(5)=-GM*q(2)/r^3 + a_y;
91 qdot(6)=-GM*q(3)/r^3 + a_z;
92
93 qdot=qdot';
94 return

```

Listing B.4: HCW Equations

```

1 function HCW_Equations
2
3 clc, clear all, close all; format long g;
4 global GM kJ2 Cd rho A m we
5 GM = 398600.435436096; % [Km^3*s^-2]
6 kJ2 = 2.633e10;
7 Cd = 0.5;
8
9 IC_for_tetrahedron % Initial condition calculator (IC plot will
   show up)
10
11 for i=1:4 % Number of deputies
12
13 Deputy_IC(:,i)=IC_TETRA(:,i); % Deputies initial conditions
14
15 rho=1.88e-11*1e9; % Atmosphere density [kg/km^3]
16 m=3; % Spacecraft initial mass [Kg]
17 A=0.03*1e-6; % Spacecraft cross-sectional area [km^2]

```

```

18 we=7.2921e-5;           % Earth rotation rate [rad/s]
19
20 % Chief initial conditions -----
21 Re=6378.1363;          % Earth radius [Km]
22 Alt=350;                % Satellite altitude [Km]
23
24 r_c0=Re+Alt;           % Initial semi-major axis [km]
25
26 wz=sqrt(GM/(r_c0^3));  % Mean motion [rad/s]
27 n=wz;
28 Period=2*pi/wz;       % Period [s]
29
30 vx0 = 0;                % Initial radial velocity [Km/s]
31 h0 = r_c0^2*wz;        % Initial angular momentum
32 OM0=0;                 % Initial RAAN [rad]
33 i0 = 0.9;              % Initial inclination [rad]
34 theta0 = pi/4;        % Initial argument of latitude [rad] (45
    deg)
35
36 % Simulation parameters -----
37 num_orb = 20;          % Number of orbits for the simulation
38 tf=num_orb*Period;    % Final time
39 dt=Period/1000;       % Time step
40 t=0:dt:tf;            % Time vector
41
42 % Hill-Clohessy-Wiltshire Equations -----
43
44 % No drift condition (Comment if undesired)
45 % Deputy_IC(5,i) = -2*n*Deputy_IC(1,i);
46
47 x = @(t) (4*Deputy_IC(1,i)+2*Deputy_IC(5,i)/n) + Deputy_IC(4,i)
    /n*sin(n*t) - (3*Deputy_IC(1,i)+2*Deputy_IC(5,i)/n)*cos(n*t);
48 y = @(t) -(6*n*Deputy_IC(1,i)+3*Deputy_IC(5,i))*t + (Deputy_IC
    (2,i)-2*Deputy_IC(4,i)/n) + (6*Deputy_IC(1,i)+4*Deputy_IC(5,i)
    )/n*sin(n*t) + 2*Deputy_IC(4,i)/n*cos(n*t);
49 z = @(t) Deputy_IC(6,i)/n*sin(n*t)+Deputy_IC(3,i)*cos(n*t);
50 xdot = @(t) Deputy_IC(4,i)*cos(n*t) + (3*Deputy_IC(1,i)*n+2*
    Deputy_IC(5,i))*sin(n*t);

```

```

51 ydot = @(t) -(6*n*Deputy_IC(1,i)+3*Deputy_IC(5,i)) + (6*n*
    Deputy_IC(1,i)+4*Deputy_IC(5,i))*cos(n*t) - 2*Deputy_IC(4,i)*
    sin(n*t);
52 zdot = @(t) Deputy_IC(6,i)*cos(n*t)-Deputy_IC(3,i)*n*sin(n*t);
53
54 Q(:,1,i)=x(t);
55 Q(:,2,i)=y(t);
56 Q(:,3,i)=z(t);
57 Q(:,4,i)=xdot(t);
58 Q(:,5,i)=ydot(t);
59 Q(:,6,i)=zdot(t);
60
61 end
62
63 save HCW_all_deputies t Q
64
65 return

```

Listing B.5: Four Deputies EOM perturbed

```

1 function Four_Deputies_EOM_v1
2
3 clc , clear all , close all ; format long g ;
4 global GM kJ2 Cd rho A m we
5 GM = 398600.435436096 ; % [Km^3*s^-2]
6 kJ2 = 2.633e10 ;
7 Cd = 0.5 ;
8
9 IC_for_tetrahedron % Initial condition calculator
10
11 for i=1:4 % Number of deputies
12
13 Deputy_IC(:,i)=IC_TETRA(:,i) ; % Deputies initial conditions
14
15 %kJ2 = 0 ; % J2 effect
16 %Cd=0 ; % Spacecraft Drag coefficient
17 rho=1.88e-11*1e9 ; % Atmosphere density at alt=350km [kg/km
    ^3]
18 m=3 ; % Spacecraft initial mass [Kg]
19 A=0.03*1e-6 ; % Spacecraft cross-sectional area [km^2]

```

```

20 we=7.2921e-5;           % Earth rotation rate [rad/s]
21
22 % Chief initial conditions -----
23 Re=6378.1363;          % Earth radius [Km]
24 Alt=350;               % Satellite altitude [Km]
25
26 r_c0=Re+Alt;           % Initial semi-major axis [km]
27
28 wz=sqrt(GM/(r_c0^3));  % Mean motion [rad/s]
29 Period=2*pi/wz;       % Period [s]
30
31 vx0 = 0;               % Initial radial velocity [Km/s]
32 h0 = r_c0^2*wz;        % Initial angular momentum
33 OM0=0;                 % Initial RAAN [rad]
34 i0 = 0.9;              % Initial inclination [rad]
35 theta0 = pi/4;         % Initial argument of latitude [rad]
36
37 % Simulation parameters -----
38 num_orb = 5;           % Number of orbits for the simulation
39 tf=num_orb*Period;     % Final time
40 dt=Period/1000;        % Time step
41 tspan=0:dt:tf;        % Time vector
42 %-----
43 qc0=[r_c0;vx0;h0;OM0;i0;theta0]; %Chief IC – Hybrid state vector
44 q0=[qc0;Deputy_IC(:,i)]; % Initial conditions vector
45 options = odeset('RelTol',1e-10,'AbsTol',1e-12);
46 [t, Q(:, :, i)] = ode113(@integrator,tspan,q0,options);
47
48 end
49
50 save Traj_Deputy_all_v1 t Q
51 disp('Simulation results saved in Traj_Deputy_all_v1');
52
53 return
54
55
56 function qdot = integrator(t,q)
57
58 global GM kJ2 Cd rho A m we

```

```

59
60 % Terms in the EOM
61 r_=[(q(1)+q(7));q(8);q(9)];
62 r=norm(r_);
63 rZ=(q(1)+q(7))*sin(q(5))*sin(q(6)) + q(8)*sin(q(5))*cos(q(6)) +
    q(9)*cos(q(5));
64
65 % Drag-related terms
66 C=(1/2)*Cd*(A/m)*rho;
67 Va_=[q(2);q(3)/q(1)-we*q(1)*cos(q(5));we*q(1)*cos(q(6))*sin(q(5)
    )];
68 Va=norm(Va_);
69
70 wz=q(3)/q(1)^2;
71 wx=-kJ2*sin(2*q(5))*sin(q(6))/(q(3)*q(1)^3) - (C/q(3))*Va*we*q
    (1)^2*cos(q(6))*sin(q(5));
72
73 we_=we*[sin(q(6))*sin(q(5));cos(q(6))*sin(q(5));cos(q(5))];
74 Vj=[q(2)+q(10)-q(8)*wz;q(3)/q(1)+q(11)+q(7)*wz-q(9)*wx;q(12)+q
    (8)*wx];
75 Vaj_=[Vj(1)+we_(3)*r_(2)-we_(2)*r_(3);Vj(2)+we_(1)*r_(3)-we_(3)*
    r_(1);Vj(3)+we_(2)*r_(1)-we_(1)*r_(2)];
76 Vaj=norm(Vaj_);
77
78 az=-2*q(3)*q(2)/q(1)^3 - kJ2*sin(q(5))^2*sin(2*q(6))/q(1)^5;
79 ax=-kJ2*sin(2*q(5))*cos(q(6))/q(1)^5 + 3*kJ2*q(2)*sin(2*q(5))*
    sin(q(6))/(q(3)*q(1)^4) - 8*kJ2^2*sin(q(5))^3*cos(q(5))*sin(q
    (6))^2*cos(q(6))/(q(3)^2*q(1)^6);
80
81 zeta=2*kJ2*sin(q(5))*sin(q(6))/q(1)^4;
82 zetaj=2*kJ2*rZ/r^5;
83
84 eta2=GM/q(1)^3 + kJ2/q(1)^5 - 5*kJ2*sin(q(5))^2*sin(q(6))^2/q(1)
    ^5;
85 eta2j=GM/r^3 + kJ2/r^5 - 5*kJ2*rZ^2/r^7;
86
87 % Chief Equations of Motion
88 % q(1)= Radius
89 qdot(1)=q(2);

```

```

90
91 % q(2)= Vx
92 qdot(2)=-GM/q(1)^2 + q(3)^2/q(1)^3 - kJ2*(1-3*sin(q(5))^2*sin(q
    (6))^2)/q(1)^4 - C*Va*q(2);
93
94 % q(3)= h (Angular momentum)
95 qdot(3)=-kJ2*sin(q(5))^2*sin(2*q(6))/q(1)^3 - C*Va*(q(3)-we*q(1)
    ^2*cos(q(5)));
96
97 % q(4)= RAAN (big omega)
98 qdot(4)=-2*kJ2*cos(q(5))*sin(q(6))^2/(q(3)*q(1)^3) - C*Va*we*q
    (1)^2*sin(2*q(6))/(2*q(3));
99
100 % q(5)= i (inclination)
101 qdot(5)=-kJ2*sin(2*q(5))*sin(2*q(6))/(2*q(3)*q(1)^3) - C*Va*we*q
    (1)^2*sin(q(5))*cos(q(6))^2/(q(3));
102
103 % q(6)= theta (argument of latitude)
104 qdot(6)= q(3)/q(1)^2 + 2*kJ2*cos(q(5))^2*sin(q(6))^2/(q(3)*q(1)
    ^3) - C*Va*we*q(1)^2*sin(2*q(6))*cos(q(5))/(2*q(3));
105
106 % Deputy Equations of Motion _____
107 qdot(7)=q(10); %q(7)=xj
108 qdot(8)=q(11); %q(8)=yj
109 qdot(9)=q(12); %q(9)=zj
110
111 qdot(10)=2*q(11)*wz - q(7)*(eta2j-wz^2) + q(8)*az - q(9)*wx*wz -
    (zetaj-zeta)*sin(q(5))*sin(q(6)) - q(1)*(eta2j-eta2) - ...
112     C*Vaj*(q(10) - q(8)*wz) - (C*Vaj - C*Va)*q(2);
113 qdot(11)=-2*q(10)*wz + 2*q(12)*wx - q(7)*az - q(8)*(eta2j - wz^2
    -wx^2) + q(9)*ax - (zetaj-zeta)*sin(q(5))*cos(q(6)) - ...
114     C*Vaj*(q(10) + q(7)*wz - q(9)*wx) - (C*Vaj - C*Va)*(q
    (3)/q(1) - we*q(1)*cos(q(5)));
115 qdot(12)=-2*q(11)*wx - q(7)*wx*wz - q(8)*ax - q(9)*(eta2j-wx^2)
    - (zetaj-zeta)*cos(q(5))- ...
116     C*Vaj*(q(12) + q(8)*wx) - (C*Vaj - C*Va)*we*q(1)*cos(q
    (6))*sin(q(5));
117
118 qdot=qdot';

```

```

119
120 return

```

Listing B.6: ConfigKeep Tetrahedron

```

1 function [X,fval , exitflag , output , c , ceq]=
   FF_configKeep_TETRA_ORBIT_1
2
3 clear all; close all
4 format long g
5
6 global GM kJ2 Q1 Q2 Q3 Q4 d0 L0 Period qc0
7 global x1 y1 z1 x2 y2 z2 x3 y3 z3 x4 y4 z4
8 global x0 y0 z0 vx0 vy0 vz0
9 global Cd rho A m we
10 %-----
11 qc0=[6878.1363;0;52360.5588603561;0;0.9;0.785398163397448];
12
13 NL_deputy_wJ2_IC_all_v2
14
15 x0=deputy_IC_NJ2_all_v2(1 ,:);
16 y0=deputy_IC_NJ2_all_v2(2 ,:);
17 z0=deputy_IC_NJ2_all_v2(3 ,:);
18 vx0=deputy_IC_NJ2_all_v2(4 ,:);
19 vy0=deputy_IC_NJ2_all_v2(5 ,:);
20 vz0=deputy_IC_NJ2_all_v2(6 ,:);
21
22 %-----
23 GM = 398600.435436096;
24 kJ2 = 2.633e10;
25 %kJ2 = 0;
26 Cd=0.5;
27 %rho=1.17510e-10*1e9; %atmosphere density at alt=250 km kg/km^3
28 %rho=4.42557e-11*1e9; %atmosphere density at alt=300 km kg/km^3
29 rho=1.87964e-11*1e9; %atmosphere density at alt=350 km kg/km^3
30 %rho=8.56205e-12*1e9; %atmosphere density at alt=400 km kg/km^3
31 %rho=4.09528e-12*1e9; %atmosphere density at alt=450 km kg/km^3
32 %rho=2.03711e-12*1e9; %atmosphere density at alt=500 km kg/km^3
33 %rho=0;
34 m=3; %kg

```

```

35 A=0.03*1e-6; % km^2
36 we=7.2921e-5; %Earth rotation rate rad/sec
37 %-----
38 Re=6378.1363;
39 Alt=500;
40
41 r_c=Re+Alt;
42 wz=sqrt(GM/(r_c^3));
43
44 Period=2*pi/wz;
45 ratio=1.0;
46 d0 = ratio*0.1;
47 L0 = ratio*0.163299316553857;
48 %-----
49
50 X10=[x0(1);y0(1);z0(1);vx0(1);vy0(1);vz0(1)]; %startign guess
51 %X10=[x0(1);y0(1);z0(1);0;0;0]; %startign guess
52 X20=[x0(2);y0(2);z0(2);vx0(2);vy0(2);vz0(2)]; %startign guess
53 %X20=[x0(2);y0(2);z0(2);0;0;0]; %startign guess
54 X30=[x0(3);y0(3);z0(3);vx0(3);vy0(3);vz0(3)]; %startign guess
55 %X30=[x0(3);y0(3);z0(3);0;0;0]; %startign guess
56 X40=[x0(4);y0(4);z0(4);vx0(4);vy0(4);vz0(4)]; %startign guess
57 %X40=[x0(4);y0(4);z0(4);0;0;0]; %startign guess
58
59 X0=[X10;X20;X30;X40]; save X0.mat X0
60
61
62 lb=[]; % lower bound
63 ub=[]; %upper bound
64
65 %options = optimset('LargeScale','off')
66 options1 = optimset('Display','iter','MaxFunEvals',1e5,'TolFun',
67     ,1e-16,'TolX',1e-16,'MaxIter',333);
68 %options1 = optimset('Display','iter','MaxFunEvals',1e5,'MaxIter',
69     ,9999)
70 [X, fval, exitflag, output] = fmincon(@fun,X0,[],[],[],[],lb,ub,
    @const,options1)
71 [c, ceq] = const(X);

```

```

71 X1=X;
72 save X1.mat X1
73 return
74
75 function F = fun(X)
76
77 global Q1 Q2 Q3 Q4 Period qc0 d0 L0
78 global x1 y1 z1 x2 y2 z2 x3 y3 z3 x4 y4 z4
79 global x0 y0 z0 vx0 vy0 vz0
80 global Cd rho A m we
81
82 tf=Period;
83 tspan=0:tf/1000:tf;
84 %-----
85 q10=[qc0;X(1);X(2);X(3);X(4);X(5);X(6)];
86 options2 = odeset('RelTol',1e-10,'AbsTol',1e-12);
87 [T Q1] = ode45(@integrator1,tspan,q10,options2);
88
89 x1 = Q1(:,7);
90 y1 = Q1(:,8);
91 z1 = Q1(:,9);
92 % vx = Q(:,10);
93 % vy = Q(:,11);
94 % vz = Q(:,12);
95 %-----
96 %-----
97 n=2;
98 q20=[qc0;X(1+6*(n-1));X(2+6*(n-1));X(3+6*(n-1));X(4+6*(n-1));X
      (5+6*(n-1));X(6+6*(n-1))];
99 options2 = odeset('RelTol',1e-10,'AbsTol',1e-12);
100 [T Q2] = ode45(@integrator2,tspan,q20,options2);
101
102 x2 = Q2(:,7);
103 y2 = Q2(:,8);
104 z2 = Q2(:,9);
105 % vx = Q(:,10);
106 % vy = Q(:,11);
107 % vz = Q(:,12);
108 %-----

```

```

109 %-----
110 n=3;
111 q30=[qc0;X(1+6*(n-1));X(2+6*(n-1));X(3+6*(n-1));X(4+6*(n-1));X
      (5+6*(n-1));X(6+6*(n-1))];
112 options2 = odeset('RelTol',1e-10,'AbsTol',1e-12);
113 [T Q3] = ode45(@integrator3,tspan,q30,options2);
114
115 x3 = Q3(:,7);
116 y3 = Q3(:,8);
117 z3 = Q3(:,9);
118 % vx = Q(:,10);
119 % vy = Q(:,11);
120 % vz = Q(:,12);
121 %-----
122 %-----
123 n=4;
124 q40=[qc0;X(1+6*(n-1));X(2+6*(n-1));X(3+6*(n-1));X(4+6*(n-1));X
      (5+6*(n-1));X(6+6*(n-1))];
125 options2 = odeset('RelTol',1e-10,'AbsTol',1e-12);
126 [T Q4] = ode45(@integrator4,tspan,q40,options2);
127
128 x4 = Q4(:,7);
129 y4 = Q4(:,8);
130 z4 = Q4(:,9);
131 % vx = Q(:,10);
132 % vy = Q(:,11);
133 % vz = Q(:,12);
134 %-----
135
136 for i=1:length(T)-1
137 d1_diff_dt(i) = ((x1(i)^2 + y1(i)^2 + z1(i)^2)^0.5 - d0)^2*(T(i
      +1)-T(i));
138 d2_diff_dt(i) = ((x2(i)^2 + y2(i)^2 + z2(i)^2)^0.5 - d0)^2*(T(i
      +1)-T(i));
139 d3_diff_dt(i) = ((x3(i)^2 + y3(i)^2 + z3(i)^2)^0.5 - d0)^2*(T(i
      +1)-T(i));
140 d4_diff_dt(i) = ((x4(i)^2 + y4(i)^2 + z4(i)^2)^0.5 - d0)^2*(T(i
      +1)-T(i));
141

```

```

142 d12_diff_dt(i) = (((x1(i)-x2(i))^2 + (y1(i)-y2(i))^2 + (z1(i)-
      z2(i))^2)^0.5 - L0)^2*(T(i+1)-T(i));
143 d13_diff_dt(i) = (((x1(i)-x3(i))^2 + (y1(i)-y3(i))^2 + (z1(i)-
      z3(i))^2)^0.5 - L0)^2*(T(i+1)-T(i));
144 d14_diff_dt(i) = (((x1(i)-x4(i))^2 + (y1(i)-y4(i))^2 + (z1(i)-
      z4(i))^2)^0.5 - L0)^2*(T(i+1)-T(i));
145
146 d23_diff_dt(i) = (((x3(i)-x2(i))^2 + (y3(i)-y2(i))^2 + (z3(i)-
      z2(i))^2)^0.5 - L0)^2*(T(i+1)-T(i));
147 d24_diff_dt(i) = (((x4(i)-x2(i))^2 + (y4(i)-y2(i))^2 + (z4(i)-
      z2(i))^2)^0.5 - L0)^2*(T(i+1)-T(i));
148
149 d34_diff_dt(i) = (((x3(i)-x4(i))^2 + (y3(i)-y4(i))^2 + (z3(i)-
      z4(i))^2)^0.5 - L0)^2*(T(i+1)-T(i));
150 end
151
152 cost_func = (sum(d1_diff_dt) + sum(d2_diff_dt) + sum(d3_diff_dt)
      + sum(d4_diff_dt) + ...
153             sum(d12_diff_dt) + sum(d13_diff_dt) + sum(
      d14_diff_dt) + ...
154             sum(d23_diff_dt) + sum(d24_diff_dt) + sum(
      d34_diff_dt))/tf;
155
156 F = cost_func;
157
158 plot3(0,0,0, '*',x1,y1,z1, '.',x2,y2,z2, '.',x3,y3,z3, '.',x4,y4,z4,
      '.'); grid on;
159 xlabel('x (km)'); ylabel('y (km)'); zlabel('z (km)');
160
161 clear i dist1_diff_dt dist2_diff_dt dist3_diff_dt dist4_diff_dt
162 clear dist12_diff_dt dist13_diff_dt dist14_diff_dt
163 clear dist23_diff_dt dist24_diff_dt dist34_diff_dt
164
165 save ConfigKeep_TETRA_wJ2_wDrag_Period1_Alt350km_100m Q1 Q2 Q3
      Q4 T
166
167 return
168
169 function [c, ceq] = const(X)

```

```

170
171 global GM d0 L0 Period qc0
172 global x1 y1 z1 x2 y2 z2 x3 y3 z3 x4 y4 z4
173 global x0 y0 z0 vx0 vy0 vz0
174 global Cd rho A m we
175
176 r0=qc0(1);
177 r0_dot=qc0(2);
178 theta0_dot=sqrt(GM/(r0^3));
179
180 c=[];
181 %%%%%%%%%%%%%%%%%%%%%%%%%%%%%%%%%%%%%%%%%%%%%%%%%%%%%%%%%%%%%%%%%%%%%%%%%%
182 %nonlinear equality constraints
183
184 %EMC1-----
185 n=1;
186 K1_1 = 0.5 * (X(4+6*(n-1)) - theta0_dot*X(2+6*(n-1)) + r0_dot)
      ^2;
187 K2_1 = 0.5 * (X(5+6*(n-1)) + theta0_dot*(X(1+6*(n-1)) + r0))^2;
188 K3_1 = 0.5 * X(6+6*(n-1))^2;
189
190 K_1 = K1_1 + K2_1 + K3_1;
191 rd_1=sqrt((r0+X(1+6*(n-1)))^2 + X(2+6*(n-1))^2 + X(3+6*(n-1))^2)
      ;
192 U_1 = -GM/rd_1;
193 %-----
194 %EMC2-----
195 n=2;
196 K1_2 = 0.5 * (X(4+6*(n-1)) - theta0_dot*X(2+6*(n-1)) + r0_dot)
      ^2;
197 K2_2 = 0.5 * (X(5+6*(n-1)) + theta0_dot*(X(1+6*(n-1)) + r0))^2;
198 K3_2 = 0.5 * X(6+6*(n-1))^2;
199
200 K_2 = K1_2 + K2_2 + K3_2;
201 rd_2=sqrt((r0+X(1+6*(n-1)))^2 + X(2+6*(n-1))^2 + X(3+6*(n-1))^2)
      ;
202 U_2 = -GM/rd_2;
203 %-----
204 %EMC3-----

```

```

205 n=3;
206 K1_3 = 0.5 * (X(4+6*(n-1)) - theta0_dot*X(2+6*(n-1)) + r0_dot)
      ^2;
207 K2_3 = 0.5 * (X(5+6*(n-1)) + theta0_dot*(X(1+6*(n-1)) + r0))^2;
208 K3_3 = 0.5 * X(6+6*(n-1))^2;
209
210 K_3 = K1_3 + K2_3 + K3_3;
211 rd_3=sqrt((r0+X(1+6*(n-1)))^2 + X(2+6*(n-1))^2 + X(3+6*(n-1))^2)
      ;
212 U_3 = -GM/rd_3;
213 %-----
214 %EMC4-----
215 n=4;
216 K1_4 = 0.5 * (X(4+6*(n-1)) - theta0_dot*X(2+6*(n-1)) + r0_dot)
      ^2;
217 K2_4 = 0.5 * (X(5+6*(n-1)) + theta0_dot*(X(1+6*(n-1)) + r0))^2;
218 K3_4 = 0.5 * X(6+6*(n-1))^2;
219
220 K_4 = K1_4 + K2_4 + K3_4;
221 rd_4=sqrt((r0+X(1+6*(n-1)))^2 + X(2+6*(n-1))^2 + X(3+6*(n-1))^2)
      ;
222 U_4 = -GM/rd_4;
223 %-----
224
225 ceq = [K_1 + U_1 + GM/(2*r0); ...
226        K_2 + U_2 + GM/(2*r0); ...
227        K_3 + U_3 + GM/(2*r0); ...
228        K_4 + U_4 + GM/(2*r0)];
229
230 return
231
232
233 function qdot = integrator1(t,q)
234
235 global GM kJ2 Cd rho A m we
236
237 %% Terms in the EOM
238 r_=[(q(1)+q(7));q(8);q(9)];
239 r=sqrt((q(1)+q(7))^2 + q(8)^2 + q(9)^2);

```

```

240 rZ=(q(1)+q(7))*sin(q(5))*sin(q(6)) + q(8)*sin(q(5))*cos(q(6)) +
      q(9)*cos(q(5));
241
242 %% Drag-related terms
243 C=(1/2)*Cd*(A/m)*rho;
244 Va_=[q(2);q(3)/q(1)-we*q(1)*cos(q(5));we*q(1)*cos(q(6))*sin(q(5)
      )];
245 Va=sqrt(Va_(1)^2 + Va_(2)^2 +Va_(3)^2);
246
247 wz=q(3)/q(1)^2;
248 wx=-kJ2*sin(2*q(5))*sin(q(6))/(q(3)*q(1)^3) - (C/q(3))*Va*we*q
      (1)^2*cos(q(6))*sin(q(5));
249
250 we_=[sin(q(6))*sin(q(5));cos(q(6))*sin(q(5));cos(q(5))];
251 Vj=[q(2)+q(10)-q(8)*wz;q(3)/q(1)+q(11)+q(7)*wz-q(9)*wx;q(12)+q
      (8)*wx];
252 Vaj_=[Vj(1)+we_(3)*r_(2)-we_(2)*r_(3);Vj(2)+we_(1)*r_(3)-we_(3)*
      r_(1);Vj(3)+we_(2)*r_(1)-we_(1)*r_(2)];
253 Vaj=sqrt(Vaj_(1)^2 + Vaj_(2)^2 +Vaj_(3)^2);
254
255 az=-2*q(3)*q(2)/q(1)^3 - kJ2*sin(q(5))^2*sin(2*q(6))/q(1)^5;
256 ax=-kJ2*sin(2*q(5))*cos(q(6))/q(1)^5 + 3*kJ2*q(2)*sin(2*q(5))*
      sin(q(6))/(q(3)*q(1)^4) - 8*kJ2^2*sin(q(5))^3*cos(q(5))*sin(q
      (6))^2*cos(q(6))/(q(3)^2*q(1)^6);
257
258 zeta=2*kJ2*sin(q(5))*sin(q(6))/q(1)^4;
259 zetaj=2*kJ2*rZ/r^5;
260
261 eta2=GM/q(1)^3 + kJ2/q(1)^5 - 5*kJ2*sin(q(5))^2*sin(q(6))^2/q(1)
      ^5;
262 eta2j=GM/r^3 + kJ2/r^5 - 5*kJ2*rZ^2/r^7;
263 %%
264 % Chief EOM
265 qdot(1)=q(2);
266 qdot(2)=-GM/q(1)^2 + q(3)^2/q(1)^3 - kJ2*(1-3*sin(q(5))^2*sin(q
      (6))^2)/q(1)^4 - C*Va*q(2);
267 qdot(3)=-kJ2*sin(q(5))^2*sin(2*q(6))/q(1)^3 - C*Va*(q(3)-we*q(1)
      ^2*cos(q(5)));
268

```

```

269 qdot(4)=-2*kJ2*cos(q(5))*sin(q(6))^2/(q(3)*q(1)^3) - C*Va*we*q
      (1)^2*sin(2*q(6))/(2*q(3));
270 qdot(5)=-kJ2*sin(2*q(5))*sin(2*q(6))/(2*q(3)*q(1)^3) - C*Va*we*q
      (1)^2*sin(q(5))*cos(q(6))^2/(q(3));
271 qdot(6)= q(3)/q(1)^2 + 2*kJ2*cos(q(5))^2*sin(q(6))^2/(q(3)*q(1)
      ^3) - C*Va*we*q(1)^2*sin(2*q(6))*cos(q(5))/(2*q(3));
272
273 % Deputy relative EOM
274 qdot(7)=q(10);
275 qdot(8)=q(11);
276 qdot(9)=q(12);
277
278 qdot(10)=2*q(11)*wz - q(7)*(eta2j-wz^2) + q(8)*az - q(9)*wx*wz -
      (zetaj-zeta)*sin(q(5))*sin(q(6)) - q(1)*(eta2j-eta2) - ...
279       C*Vaj*(q(10) - q(8)*wz) - (C*Vaj - C*Va)*q(2);
280 qdot(11)=-2*q(10)*wz + 2*q(12)*wx - q(7)*az - q(8)*(eta2j - wz^2
      -wx^2) + q(9)*ax - (zetaj-zeta)*sin(q(5))*cos(q(6)) - ...
281       C*Vaj*(q(10) + q(7)*wz - q(9)*wx) - (C*Vaj - C*Va)*(q
      (3)/q(1) - we*q(1)*cos(q(5)));
282 qdot(12)=-2*q(11)*wx - q(7)*wx*wz - q(8)*ax - q(9)*(eta2j-wx^2)
      - (zetaj-zeta)*cos(q(5))- ...
283       C*Vaj*(q(12) + q(8)*wx) - (C*Vaj - C*Va)*we*q(1)*cos(q
      (6))*sin(q(5));
284
285
286 qdot=qdot';
287
288 return
289
290 function qdot = integrator2(t,q)
291
292 global GM kJ2 Cd rho A m we
293
294 %% Terms in the EOM
295 r_=[(q(1)+q(7));q(8);q(9)];
296 r=sqrt((q(1)+q(7))^2 + q(8)^2 + q(9)^2);
297 rZ=(q(1)+q(7))*sin(q(5))*sin(q(6)) + q(8)*sin(q(5))*cos(q(6)) +
      q(9)*cos(q(5));
298

```

```

299 %% Drag-related terms
300 C=(1/2)*Cd*(A/m)*rho;
301 Va_=[q(2);q(3)/q(1)-we*q(1)*cos(q(5));we*q(1)*cos(q(6))*sin(q(5)
    )];
302 Va=sqrt(Va_(1)^2 + Va_(2)^2 +Va_(3)^2);
303
304 wz=q(3)/q(1)^2;
305 wx=-kJ2*sin(2*q(5))*sin(q(6))/(q(3)*q(1)^3) - (C/q(3))*Va*we*q
    (1)^2*cos(q(6))*sin(q(5));
306
307 we_=we*[sin(q(6))*sin(q(5));cos(q(6))*sin(q(5));cos(q(5))];
308 Vj=[q(2)+q(10)-q(8)*wz;q(3)/q(1)+q(11)+q(7)*wz-q(9)*wx;q(12)+q
    (8)*wx];
309 Vaj_=[Vj(1)+we_(3)*r_(2)-we_(2)*r_(3);Vj(2)+we_(1)*r_(3)-we_(3)*
    r_(1);Vj(3)+we_(2)*r_(1)-we_(1)*r_(2)];
310 Vaj=sqrt(Vaj_(1)^2 + Vaj_(2)^2 +Vaj_(3)^2);
311
312 az=-2*q(3)*q(2)/q(1)^3 - kJ2*sin(q(5))^2*sin(2*q(6))/q(1)^5;
313 ax=-kJ2*sin(2*q(5))*cos(q(6))/q(1)^5 + 3*kJ2*q(2)*sin(2*q(5))*
    sin(q(6))/(q(3)*q(1)^4) - 8*kJ2^2*sin(q(5))^3*cos(q(5))*sin(q
    (6))^2*cos(q(6))/(q(3)^2*q(1)^6);
314
315 zeta=2*kJ2*sin(q(5))*sin(q(6))/q(1)^4;
316 zetaj=2*kJ2*rZ/r^5;
317
318 eta2=GM/q(1)^3 + kJ2/q(1)^5 - 5*kJ2*sin(q(5))^2*sin(q(6))^2/q(1)
    ^5;
319 eta2j=GM/r^3 + kJ2/r^5 - 5*kJ2*rZ^2/r^7;
320 %%
321 % Chief EOM
322 qdot(1)=q(2);
323 qdot(2)=-GM/q(1)^2 + q(3)^2/q(1)^3 - kJ2*(1-3*sin(q(5))^2*sin(q
    (6))^2)/q(1)^4 - C*Va*q(2);
324 qdot(3)=-kJ2*sin(q(5))^2*sin(2*q(6))/q(1)^3 - C*Va*(q(3)-we*q(1)
    ^2*cos(q(5)));
325
326 qdot(4)=-2*kJ2*cos(q(5))*sin(q(6))^2/(q(3)*q(1)^3) - C*Va*we*q
    (1)^2*sin(2*q(6))/(2*q(3));

```

```

327 qdot(5)=-kJ2*sin(2*q(5))*sin(2*q(6))/(2*q(3)*q(1)^3) - C*Va*we*q
      (1)^2*sin(q(5))*cos(q(6))^2/(q(3));
328 qdot(6)= q(3)/q(1)^2 + 2*kJ2*cos(q(5))^2*sin(q(6))^2/(q(3)*q(1)
      ^3) - C*Va*we*q(1)^2*sin(2*q(6))*cos(q(5))/(2*q(3));
329
330 % Deputy relative EOM
331 qdot(7)=q(10);
332 qdot(8)=q(11);
333 qdot(9)=q(12);
334
335 qdot(10)=2*q(11)*wz - q(7)*(eta2j-wz^2) + q(8)*az - q(9)*wx*wz -
      (zetaj-zeta)*sin(q(5))*sin(q(6)) - q(1)*(eta2j-eta2) - ...
336      C*Vaj*(q(10) - q(8)*wz) - (C*Vaj - C*Va)*q(2);
337 qdot(11)=-2*q(10)*wz + 2*q(12)*wx - q(7)*az - q(8)*(eta2j - wz^2
      -wx^2) + q(9)*ax - (zetaj-zeta)*sin(q(5))*cos(q(6)) - ...
338      C*Vaj*(q(10) + q(7)*wz - q(9)*wx) - (C*Vaj - C*Va)*(q
      (3)/q(1) - we*q(1)*cos(q(5)));
339 qdot(12)=-2*q(11)*wx - q(7)*wx*wz - q(8)*ax - q(9)*(eta2j-wx^2)
      - (zetaj-zeta)*cos(q(5))- ...
340      C*Vaj*(q(12) + q(8)*wx) - (C*Vaj - C*Va)*we*q(1)*cos(q
      (6))*sin(q(5));
341
342
343 qdot=qdot';
344
345 return
346
347 function qdot = integrator3(t,q)
348
349 global GM kJ2 Cd rho A m we
350
351 %% Terms in the EOM
352 r_=[(q(1)+q(7));q(8);q(9)];
353 r=sqrt((q(1)+q(7))^2 + q(8)^2 + q(9)^2);
354 rZ=(q(1)+q(7))*sin(q(5))*sin(q(6)) + q(8)*sin(q(5))*cos(q(6)) +
      q(9)*cos(q(5));
355
356 %% Drag-related terms
357 C=(1/2)*Cd*(A/m)*rho;

```

```

358 Va_=[q(2);q(3)/q(1)-we*q(1)*cos(q(5));we*q(1)*cos(q(6))*sin(q(5)
    )];
359 Va=sqrt(Va_(1)^2 + Va_(2)^2 +Va_(3)^2);
360
361 wz=q(3)/q(1)^2;
362 wx=-kJ2*sin(2*q(5))*sin(q(6))/(q(3)*q(1)^3) - (C/q(3))*Va*we*q
    (1)^2*cos(q(6))*sin(q(5));
363
364 we_=[sin(q(6))*sin(q(5));cos(q(6))*sin(q(5));cos(q(5))];
365 Vj=[q(2)+q(10)-q(8)*wz;q(3)/q(1)+q(11)+q(7)*wz-q(9)*wx;q(12)+q
    (8)*wx];
366 Vaj_=[Vj(1)+we_(3)*r_(2)-we_(2)*r_(3);Vj(2)+we_(1)*r_(3)-we_(3)*
    r_(1);Vj(3)+we_(2)*r_(1)-we_(1)*r_(2)];
367 Vaj=sqrt(Vaj_(1)^2 + Vaj_(2)^2 +Vaj_(3)^2);
368
369 az=-2*q(3)*q(2)/q(1)^3 - kJ2*sin(q(5))^2*sin(2*q(6))/q(1)^5;
370 ax=-kJ2*sin(2*q(5))*cos(q(6))/q(1)^5 + 3*kJ2*q(2)*sin(2*q(5))*
    sin(q(6))/(q(3)*q(1)^4) - 8*kJ2^2*sin(q(5))^3*cos(q(5))*sin(q
    (6))^2*cos(q(6))/(q(3)^2*q(1)^6);
371
372 zeta=2*kJ2*sin(q(5))*sin(q(6))/q(1)^4;
373 zetaj=2*kJ2*rZ/r^5;
374
375 eta2=GM/q(1)^3 + kJ2/q(1)^5 - 5*kJ2*sin(q(5))^2*sin(q(6))^2/q(1)
    ^5;
376 eta2j=GM/r^3 + kJ2/r^5 - 5*kJ2*rZ^2/r^7;
377 %%
378 % Chief EOM
379 qdot(1)=q(2);
380 qdot(2)=-GM/q(1)^2 + q(3)^2/q(1)^3 - kJ2*(1-3*sin(q(5))^2*sin(q
    (6))^2)/q(1)^4 - C*Va*q(2);
381 qdot(3)=-kJ2*sin(q(5))^2*sin(2*q(6))/q(1)^3 - C*Va*(q(3)-we*q(1)
    ^2*cos(q(5)));
382
383 qdot(4)=-2*kJ2*cos(q(5))*sin(q(6))^2/(q(3)*q(1)^3) - C*Va*we*q
    (1)^2*sin(2*q(6))/(2*q(3));
384 qdot(5)=-kJ2*sin(2*q(5))*sin(2*q(6))/(2*q(3)*q(1)^3) - C*Va*we*q
    (1)^2*sin(q(5))*cos(q(6))^2/(q(3));

```

```

385 qdot(6)= q(3)/q(1)^2 + 2*kJ2*cos(q(5))^2*sin(q(6))^2/(q(3)*q(1)
      ^3) - C*Va*we*q(1)^2*sin(2*q(6))*cos(q(5))/(2*q(3));
386
387 % Deputy relative EOM
388 qdot(7)=q(10);
389 qdot(8)=q(11);
390 qdot(9)=q(12);
391
392 qdot(10)=2*q(11)*wz - q(7)*(eta2j-wz^2) + q(8)*az - q(9)*wx*wz -
      (zetaj-zeta)*sin(q(5))*sin(q(6)) - q(1)*(eta2j-eta2) - ...
393      C*Vaj*(q(10) - q(8)*wz) - (C*Vaj - C*Va)*q(2);
394 qdot(11)=-2*q(10)*wz + 2*q(12)*wx - q(7)*az - q(8)*(eta2j - wz^2
      -wx^2) + q(9)*ax - (zetaj-zeta)*sin(q(5))*cos(q(6)) - ...
395      C*Vaj*(q(10) + q(7)*wz - q(9)*wx) - (C*Vaj - C*Va)*(q
      (3)/q(1) - we*q(1)*cos(q(5)));
396 qdot(12)=-2*q(11)*wx - q(7)*wx*wz - q(8)*ax - q(9)*(eta2j-wx^2)
      - (zetaj-zeta)*cos(q(5))- ...
397      C*Vaj*(q(12) + q(8)*wx) - (C*Vaj - C*Va)*we*q(1)*cos(q
      (6))*sin(q(5));
398
399
400 qdot=qdot';
401
402 return
403
404 function qdot = integrator4(t,q)
405
406 global GM kJ2 Cd rho A m we
407
408 %% Terms in the EOM
409 r_=[(q(1)+q(7));q(8);q(9)];
410 r=sqrt((q(1)+q(7))^2 + q(8)^2 + q(9)^2);
411 rZ=(q(1)+q(7))*sin(q(5))*sin(q(6)) + q(8)*sin(q(5))*cos(q(6)) +
      q(9)*cos(q(5));
412
413 %% Drag-related terms
414 C=(1/2)*Cd*(A/m)*rho;
415 Va_=[q(2);q(3)/q(1)-we*q(1)*cos(q(5));we*q(1)*cos(q(6))*sin(q(5)
      )];

```

```

416 Va=sqrt(Va_(1)^2 + Va_(2)^2 +Va_(3)^2);
417
418 wz=q(3)/q(1)^2;
419 wx=-kJ2*sin(2*q(5))*sin(q(6))/(q(3)*q(1)^3) - (C/q(3))*Va*we*q
      (1)^2*cos(q(6))*sin(q(5));
420
421 we_=we*[sin(q(6))*sin(q(5));cos(q(6))*sin(q(5));cos(q(5))];
422 Vj=[q(2)+q(10)-q(8)*wz;q(3)/q(1)+q(11)+q(7)*wz-q(9)*wx;q(12)+q
      (8)*wx];
423 Vaj_=[Vj(1)+we_(3)*r_(2)-we_(2)*r_(3);Vj(2)+we_(1)*r_(3)-we_(3)*
      r_(1);Vj(3)+we_(2)*r_(1)-we_(1)*r_(2)];
424 Vaj=sqrt(Vaj_(1)^2 + Vaj_(2)^2 +Vaj_(3)^2);
425
426 az=-2*q(3)*q(2)/q(1)^3 - kJ2*sin(q(5))^2*sin(2*q(6))/q(1)^5;
427 ax=-kJ2*sin(2*q(5))*cos(q(6))/q(1)^5 + 3*kJ2*q(2)*sin(2*q(5))*
      sin(q(6))/(q(3)*q(1)^4) - 8*kJ2^2*sin(q(5))^3*cos(q(5))*sin(q
      (6))^2*cos(q(6))/(q(3)^2*q(1)^6);
428
429 zeta=2*kJ2*sin(q(5))*sin(q(6))/q(1)^4;
430 zetaj=2*kJ2*rZ/r^5;
431
432 eta2=GM/q(1)^3 + kJ2/q(1)^5 - 5*kJ2*sin(q(5))^2*sin(q(6))^2/q(1)
      ^5;
433 eta2j=GM/r^3 + kJ2/r^5 - 5*kJ2*rZ^2/r^7;
434 %%
435 % Chief EOM
436 qdot(1)=q(2);
437 qdot(2)=-GM/q(1)^2 + q(3)^2/q(1)^3 - kJ2*(1-3*sin(q(5))^2*sin(q
      (6))^2)/q(1)^4 - C*Va*q(2);
438 qdot(3)=-kJ2*sin(q(5))^2*sin(2*q(6))/q(1)^3 - C*Va*(q(3)-we*q(1)
      ^2*cos(q(5)));
439
440 qdot(4)=-2*kJ2*cos(q(5))*sin(q(6))^2/(q(3)*q(1)^3) - C*Va*we*q
      (1)^2*sin(2*q(6))/(2*q(3));
441 qdot(5)=-kJ2*sin(2*q(5))*sin(2*q(6))/(2*q(3)*q(1)^3) - C*Va*we*q
      (1)^2*sin(q(5))*cos(q(6))^2/(q(3));
442 qdot(6)= q(3)/q(1)^2 + 2*kJ2*cos(q(5))^2*sin(q(6))^2/(q(3)*q(1)
      ^3) - C*Va*we*q(1)^2*sin(2*q(6))*cos(q(5))/(2*q(3));
443

```

```

444 % Deputy relative EOM
445 qdot(7)=q(10);
446 qdot(8)=q(11);
447 qdot(9)=q(12);
448
449 qdot(10)=2*q(11)*wz - q(7)*(eta2j-wz^2) + q(8)*az - q(9)*wx*wz -
      (zetaj-zeta)*sin(q(5))*sin(q(6)) - q(1)*(eta2j-eta2) - ...
450      C*Vaj*(q(10) - q(8)*wz) - (C*Vaj - C*Va)*q(2);
451 qdot(11)=-2*q(10)*wz + 2*q(12)*wx - q(7)*az - q(8)*(eta2j - wz^2
      -wx^2) + q(9)*ax - (zetaj-zeta)*sin(q(5))*cos(q(6)) - ...
452      C*Vaj*(q(10) + q(7)*wz - q(9)*wx) - (C*Vaj - C*Va)*(q
      (3)/q(1) - we*q(1)*cos(q(5)));
453 qdot(12)=-2*q(11)*wx - q(7)*wx*wz - q(8)*ax - q(9)*(eta2j-wx^2)
      - (zetaj-zeta)*cos(q(5))- ...
454      C*Vaj*(q(12) + q(8)*wx) - (C*Vaj - C*Va)*we*q(1)*cos(q
      (6))*sin(q(5));
455
456
457 qdot=qdot';
458
459 return

```

This page is intentionally left blank

Bibliography

- [1] Milani, A. *Orbite Periodiche, Perturbazioni, Risonanze: Elementi di Storia Interna ed Esterna della Meccanica Celeste*. Vol. 5. Mathematical Institute - University of Pisa, Mar. 1978, pp. 3–4 (cit. on p. 2).
- [2] Karimi, R. R. «Designing an interplanetary autonomous spacecraft navigation system using visible planets». PhD thesis. Texas A&M University, May 2012 (cit. on p. 5).
- [3] Alfriend, K. T.; Vadali, S. R.; Gurfil, P.; How, J. P., and Breger, L. S. *Spacecraft Formation Flying - Dynamics, Control and Navigation*. Butterworth-Heinemann, Elsevier Astrodynamics Series, 2010 (cit. on pp. 7, 9, 19–21, 28, 30).
- [4] Sholomitsky, G. B.; Prilutsky, O. F., and Rodin, V. G. «Infra-red Space Interferometer». In: *28th International Astronautical Federation Congress*. 1977 (cit. on p. 7).
- [5] Wang, P. and Hadaegh, F. Y. «Coordination and Control of Multiple Microspacecraft Moving in Formation». In: *Journal of the Astronautical Sciences* 44.3 (July 1996), pp. 315–355 (cit. on p. 8).
- [6] Ren, W. and Beard, R. W. «Virtual Structure Based Spacecraft Formation Control with Formation Feedback». In: *AIAA Guidance, Navigation, and Control Conference and Exhibit*. Monterey, California, Aug. 2002 (cit. on p. 9).
- [7] ESA official website. *Cluster II operations*. https://www.esa.int/Enabling_Support/Operations/Cluster_II_operations. [Accessed: March 31st, 2021] (cit. on p. 11).

- [8] ESA official website. *Extended life for ESA's science missions*. https://www.esa.int/About_Us/ESAC/Extended_life_for_ESA_s_science_missions. [Accessed: March 31st, 2021]. 2018 (cit. on p. 11).
- [9] JPL official website. *GRACE mission*. <https://www.jpl.nasa.gov/missions/gravity-recovery-and-climate-experiment-grace/>. [Accessed: March 31st, 2021] (cit. on p. 11).
- [10] ESA official website. *About Proba-3*. https://www.esa.int/Enabling_Support/Space_Engineering_Technology/Proba_Missions/About_Proba-3. [Accessed: March 31st, 2021]. 2021 (cit. on p. 13).
- [11] ESA official website. *Darwin overview*. <http://www.esa.int/science/darwin>. [Accessed: March 31st, 2021] (cit. on p. 13).
- [12] Delpech, M.; Malbet, F.; Karlsson, T.; Larsson, R.; Léger, A., and Jorgensen, J. «Flight Demonstration of Formation Flying Capabilities for Future Missions (NEAT Pathfinder)». In: *Acta Astronautica* 105.1 (May 2014), pp. 82–94 (cit. on p. 15).
- [13] Karimi, R. R.; Peterson, J. T. A.; Rahmani, A.; Chung, S.-J.; Junkins, J. L., and Hadaeagh, F. Y. «Swarm of Satellites Initial Formation Maintenance using Impulsive and Low Thrust Maneuvers». In: (2020) (cit. on pp. 15, 34).
- [14] Bandyopadhyay, S.; Foust, R.; Subramanian, G. P.; Chung, S.-J., and Hadaeagh, F. Y. «Review of Formation Flying and Constellation Missions Using Nanosatellites». In: *Journal of Spacecraft and Rockets* 53.3 (Mar. 2016), pp. 567–578 (cit. on p. 15).
- [15] Clohessy, W. H. and Wiltshire, R. S. «Terminal Guidance System for Satellite Rendezvous». In: *Journal of the Aerospace Sciences* 27.9 (1960), pp. 653–658 (cit. on p. 30).
- [16] Li, W.-J. et al. «On-orbit service (OOS) of spacecraft: A review of engineering developments». In: *Progress in Aerospace Sciences* 108 (July 2019), pp. 32–120 (cit. on pp. 34, 56).
- [17] Xu, G. and Wang, D. «Nonlinear Dynamic Equations of Satellite Relative Motion Around an Oblate Earth». In: *Journal of Guidance, Control, and Dynamics* 31.5 (2008), pp. 1521–1524 (cit. on p. 37).

- [18] Morgan, D.; Chung, S.-J.; Blackmore, L.; Acikmese, B.; Bayard, D., and Hadaegh, F. Y. «Swarm-Keeping Strategies for Spacecraft Under J_2 and Atmospheric Drag Perturbations». In: *Journal of Guidance, Control, and Dynamics* 35.5 (2012), pp. 1492–1506 (cit. on p. 37).
- [19] Lemmer, K. «Propulsion for CubeSats». In: *Acta Astronautica* 134 (May 2017), pp. 231–243 (cit. on p. 55).
- [20] Cardin, J.; Coste, K.; Williamson, D., and Gloyer, P. «A cold gas micro-propulsion system for cubesats». In: *17th Annual AIAA/USU Conference on Small Satellites*. Logan, Utah, 2003 (cit. on p. 55).
- [21] Russell, C. T. et al. «Dawn at Vesta: Testing the Protoplanetary Paradigm». In: *Science* 336 (2012), pp. 684–686 (cit. on p. 67).
- [22] JPL official website. *JPL Small-Body Database: 4-Vesta*. <https://ssd.jpl.nasa.gov/sbdb.cgi?sstr=4>. [Accessed: March 31st, 2021] (cit. on p. 68).
- [23] NASA official website. *Dawn Mission*. https://www.nasa.gov/mission_pages/dawn/main/index.html. [Accessed: March 31st, 2021] (cit. on p. 68).
- [24] NASA official website. *NASA's Dawn Mission to Asteroid Belt Comes to End*. <https://www.nasa.gov/press-release/nasa-s-dawn-mission-to-asteroid-belt-comes-to-end>. [Accessed: March 31st, 2021] (cit. on p. 68).
- [25] Scharf, D. P.; Hadaegh, F. Y., and Ploen, S. R. «A Survey of Spacecraft Formation Flying Guidance and Control. Part I: Guidance». In: *Proceedings of the 2003 American Control Conference*. IEEE. Denver, Colorado, June 2003.
- [26] Scharf, D. P.; Hadaegh, F. Y., and Ploen, S. R. «A Survey of Spacecraft Formation Flying Guidance and Control. Part II: Control». In: *Proceedings of the 2004 American Control Conference*. Vol. 4. IEEE. Boston, Massachusetts, June 2004, pp. 2976–2985.